Development of reduced-order models for predicting the plastic deformation of metals employing material knowledge systems.

A Dissertation
Presented to
The Academic Faculty

by

David Montes de Oca Zapiain

In Partial Fulfillment
of the Requirements for the Degree
Doctor of Philosophy in Mechanical Engineering in the
George W. Woodruff School of Mechanical Engineering

Georgia Institute of Technology
May 2019

Development of reduced-order models for predicting the plastic deformation of metals employing material knowledge systems.

Approved by:

Dr. Surya R. Kalidindi, Advisor
School of Mechanical Engineering
Georgia Institute of Technology

Dr. Richard W. Neu
School of Mechanical Engineering
Georgia Institute of Technology

Dr. David L. McDowell
School of Material Science & Engineering
Georgia Institute of Technology

Dr. Hojun Lim
SANDIA National Laboratories

Dr. Hamid Garmestani
School of Material Science & Engineering
Georgia Institute of Technology

Date Approved: March 25, 2019

To my family,

whose sacrifice and unwavering support

enabled me to complete this endeavor.

ACKNOWLEDGEMENTS

First of all, I would like to thank my advisor Dr. Surya R. Kalidindi for his guidance and mentorship throughout my PhD studies. I have taken his teachings to heart since they have defined not only the rigorous researcher I am, but the academic I aspire to be.

I would also like to thank Dr. Hamid Garmestani, Dr. Hojun Lim, Dr. David L. McDowell and Dr. Richard W. Neu for participating in my defense committee and for providing new and fresh insights on this research.

I would also like to thank the Office of Naval Research (ONR) for funding this research under the award number N00014-15-1-2478 (Dr. William M. Mullins, program manager).

I would like to thank Dr. Dipen Patel, Dr. Noah Paulson, Dr. Ali Khosravani and Almambet Iskavov for their useful discussions around old and new concepts. I would also like to thank Apaar Shanker for guiding me into the world of deep learning, as well as all rest of the members of our research group for their comradery and support.

Finally, I would like to thank my parents David Montes de Oca Rosas, Maria del Carmen Zapiain Bazdresch and my brothers Arturo Montes de Oca Zapiain and Ana Paula Montes de Oca Zapiain for their unwavering support.

TABLE OF CONTENTS

LIST OF TABLES

LIST OF FIGURES

NOMENCLATURE

MKS	Material Knowledge System
RVE	Representative Volume Element
3-D	Three Dimensional
CPFEM	Crystal Plasticity Finite Element Models
FFT	Fast Fourier Transform
DFT	Discrete Fourier Transform
GFS	Generalized Fourier Series
OLS	Ordinary Least Squares
GSH	Generalized Spherical Harmonics
ODF	Orientation Distribution Function
FEM	Finite Element Method
FCC	Face Center Cubic

SUMMARY

Metal alloys being explored for structural applications exhibit a complex polycrystalline internal structure that intrinsically spans multiple length-scales. Therefore, rational design efforts for such alloys require a multiscale modeling framework capable of adequately incorporating the appropriate physics that control/drive the plastic deformation at the different length scales when modeling the overall plastic response of the alloy. The establishment of the desired multiscale modeling frameworks requires the development of low-computational cost, non-iterative, frameworks capable of accurately localizing the anisotropic plastic response of polycrystalline microstructures.

This dissertation addresses the outlined needs by defining suitable extensions to the scale-bridging, data-driven Material Knowledge System Framework. The extensions detailed in the subsequent chapters enabled the first successful implementation of this framework for predicting the plastic response of polycrystalline microstructures caused by any arbitrary periodic boundary condition imposed at the macroscale. The case studies presented in this work demonstrate that the localization models developed using the MKS framework are of low-computational cost and non-iterative. Nevertheless, their predictions are not as accurate as desired. As a result, leveraging the insights obtained from the implementation of this framework to polycrystalline plasticity, this dissertation provides a robust protocol to incorporate deep learning approaches in order to provide better predictions of the local plastic response in polycrystalline RVEs. The final case study performed in this dissertation establishes that the most robust approaches to develop accurate localization reduced-order models capable of accurately predicting the local anisotropic plastic response of polycrystalline microstructures are deep learning approaches such as Convolutional Neural Networks.

CHAPTER 1:

Introduction

Metal alloys explored for structural applications typically exhibit complex polycrystalline internal structures at the mesoscale (i.e., at the scale of individual crystals also called grains). Therefore, rational design and development efforts for such alloys require a multiscale modeling framework that accounts accurately for the different physics at the different length scales in modeling the overall plastic response of the alloy [1-7]. As an illustrative example, Figure 1 schematically shows the specifics of the coupling between the details of material constitutive response occurring at the macroscale and the mesoscale in a sheet forming operation. At the macroscale (i.e., the scale of the sheet geometry), the material constitutive response is formulated using quantities such as the effective stress tensor $\langle \boldsymbol{\sigma} \rangle$ and the effective stretching tensor $\langle \boldsymbol{D} \rangle$. These macroscale effective quantities are defined as volume-averaged quantities over a representative volume element (RVE) identified at the mesoscale. In Figure 1, the mesoscale RVE is depicted to comprise a multitude of grains with different crystal lattice orientations. The relevant microscale quantities are $\boldsymbol{\sigma}(\boldsymbol{x})$ and $\boldsymbol{D}(\boldsymbol{x})$, where $\boldsymbol{x}$ denotes a spatial location in the RVE. Formulation of precise mathematical relationships between these different macroscale and mesoscale quantities is the main goal of a multiscale materials modeling framework. It is convenient to consider these relationships in two distinct directions: (i) homogenization - going from mesoscale to the macroscale, and (ii) localization – going from the macroscale to the mesoscale.

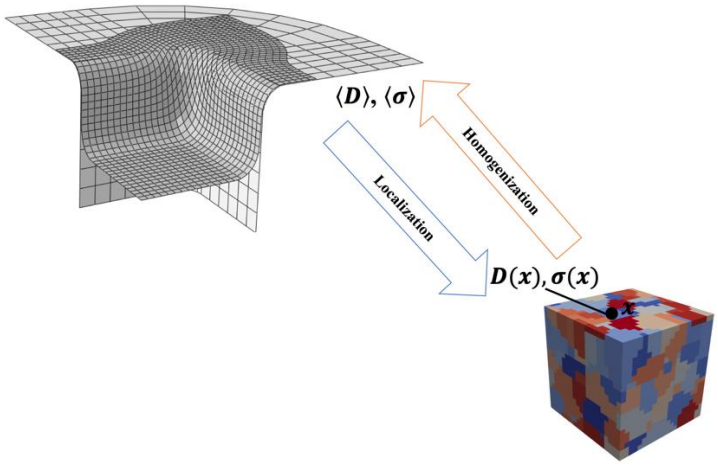

Figure 1: Schematic of a Multiscale Method that Links Mesoscale Defined Quantities to their Effective Macroscale Quantities Via Homogenization and Localization Models.

Development of high fidelity models for the localization of the plastic response in heterogeneous materials has encountered significant challenges because one needs to find solutions that satisfy both the governing equilibrium field equations as well as the highly nonlinear material constitutive laws throughout the volumetric domain of the RVE. For polycrystalline microstructures, the relevant constitutive theories are generally referred as crystal plasticity theories[8-12]. These theories incorporate successfully the many intricate details of the plastic deformation occurring at the level of individual grains (e.g., crystallographic slip on defined slips systems), and are known to result in numerically stiff set of coupled nonlinear equations. Consequently, one often has to resort to numerical approaches for addressing multiscale plasticity problems in metal alloy components. The most popular approach for simulating the plastic deformation in polycrystalline RVEs has been to use the crystal plasticity finite element models (CPFEM) [13-18]. The CPFEM have enjoyed tremendous success in explaining the many microstructure-sensitive plastic responses of polycrystalline metals. These have included various anisotropic responses in metal-forming operations (e.g., [19, 20]), variations in formability of

metal sheets (e.g., [21, 22]), and damage initiation in dual phase steels (e.g., [23]). An exhaustive summary of the successes and challenges in CPFEM has been expounded in a recent review article [24]. In spite of the many successes of CPFEM, their high computational cost prevents them from being successfully incorporated into a fully-coupled macroscale-mesoscale simulation of the type depicted in Figure 1. This is because one needs to perform a multilevel finite element simulation incorporating a CPFEM simulation at each integration point in the macroscale finite element simulation to accomplish the stated goal [25-28].Ongoing efforts in this direction typically aim to employ major computational resources and clever parallelization of the numerical calculations to overcome the inherent challenges [25, 29, 30].

As an alternative to CPFEM, a fast Fourier transform (FFT)-based method has been developed by Lebensohn [31], building on earlier work of Suquet et al. [32]. This approach leverages the Green's function method [33], which computes the local nonlinear response field in a heterogeneous medium using an iterative strategy. Each iteration in this approach involves the evaluation of a convolution integral that can be efficiently carried out by exploiting the properties of discrete Fourier transforms (DFTs) using an FFT algorithm. This approach significantly lowers the computational cost involved in solving for the mesoscale response fields (e.g., plastic stretching tensors) [34-37]. However, the computational cost of the FFT method is still too large to facilitate a fully-coupled multiscale simulation of metal plasticity using only modest computational resources. This is mainly because the approach relies on solving the governing equations at the microscale iteratively for each integration point at the macroscale. Moreover, if one needs to use a relatively large RVE size, the iterations can become computationally expensive [38]. Therefore, there still exists a critical need for a low-computational cost, non-iterative,

framework capable of accurately localizing the anisotropic plastic response of polycrystalline microstructures.

In recent years, our research group has developed a computational framework called Materials Knowledge Systems (MKS) that leverages the statistical continuum theories developed by Kröner [39, 40] (the Green's function method mentioned earlier is also derived from the same theories) to obtain a calibrated series expansion that can directly compute (without iterations) the localized response field of interest in heterogeneous microstructures [7, 41]. The MKS framework also exploits DFT representations (and FFT algorithms) both for efficient calibration of the localization models as well as for the predictions of the localized response for new material microstructures. This is accomplished by re-organizing the convolution integrals involved in the series expansion such that the kernel functions are completely independent of the material microstructure and can therefore be calibrated in a one-time computational effort. The calibration is usually performed using the results generated by a numerical approach such as the finite element method on an ensemble of selected microstructures. Although the computational cost in this one-time calibration is high, all further use of the calibrated localization models (usually calibrated for a selected material class of interest) incurs minimal computational cost [7, 41-45]. The viability, remarkable accuracy, and significant computational savings of the MKS localization kernels have been demonstrated on a broad range of multiscale materials phenomena [43-48].

The MKS localization models developed previously for the elastic and the rigid-perfectly plastic responses of heterogeneous media form the foundations for the present dissertation. It was previously demonstrated that MKS localization models provided excellent predictions of the local elastic and thermo-elastic responses in multiphase composites with moderate contrasts (contrast here reflects the ratio of the elastic stiffnesses of the constituent phases in the composite material)

[44, 49]. It was also discovered that the systematic introduction of the higher-order terms in the series expansion showed tremendous potential for improving the accuracy of the localization models for the higher contrast composites [50]. Additionally, the validity of the MKS localization approaches for rigid-perfectly plastic response of a two phase composite has been initially demonstrated in a simple case study [43]. More recently, it was demonstrated that the MKS framework can be extended to elastic response of polycrystalline microstructures [45, 48] (here the local state at each point in the mesoscale RVE is defined through the specification of a crystal lattice orientation expressed in the form of an ordered set of three Bunge-Euler angles [51]). This was accomplished by employing Fourier representations of both the kernel function and the microstructure function over the orientation space using generalized spherical harmonics (GSH) [7, 45, 48, 51]. Most importantly, in all the aforementioned implementations, the MKS localization models were found to provide highly accurate predictions of the mesoscale fields with 2-3 orders of magnitude savings in the computational cost. Furthermore, these computational savings were observed to be relatively independent of the RVE size[41, 44].

The recent advances in the MKS framework described above set the stage for this dissertation, in which suitable extensions to the MKS framework are successfully defined to enable the first successful implementation of this framework for predicting the plastic response of polycrystalline microstructures. As a result, the protocols outlined in this dissertation enable the successful establishment of low-computational cost, non-iterative, localization models for localizing the anisotropic plastic response of polycrystalline microstructures. Thus, paving the way forward for the development of fully-coupled computationally inexpensive multiscale plasticity simulations. This dissertation also provides a robust framework to incorporate deep learning approaches to provide better predictions of the local plastic response in polycrystalline RVEs.

Therefore, opening new research avenues by providing a clear path forward for successfully implementing deep learning techniques to develop accurate and feature-engineering-free localization model for complex, heterogenous and non-linear phenomena in complex material structures.

It is important to acknowledge that the localization models developed in this dissertation focus solely on localizing the plastic response at an instant in time. In order to apply the developed models to finite strain levels, additional advances are needed. These include: the incorporation of elastic deformations to allow for a proper treatment of the elastic-plastic deformations in polycrystalline metals, and the update of the microstructure after a specified time step with the imposed plastic stretching tensor. Finally, it is important to clarify that the localization models developed in this work interest focus on localizing the response of polycrystalline RVEs whose plastic behavior is modeled by a size-independent crystal plasticity theory. In other words, the mechanism that affect/drive the plastic behavior of RVE's containing a small numbers of grains is not considered. All of these problems need further development and are beyond the scope of the present dissertation.

CHAPTER 2:

Review of Fundamental Concepts

The purpose of this chapter is to provide a review of fundamental concepts required to follow (and understand) the expressions and derivations developed in this dissertation. It is important to acknowledge that this chapter summarizes the most important properties and details of the mathematical concepts of interest to this dissertation. Consequently, the reader should bear in mind that the treatment of the concepts is far from being comprehensive. For a thorough and comprehensive treatment of the concepts introduced in this chapter please confer to the following references[7, 41, 51-53].

2.1 Generalized Fourier Series

A function space defined over $0 < t < T$ can be spanned by a set of orthonormal basis functions $\mathrm{A}_k(t)$ $(k = 0, \pm 1, \pm 2, \ldots)$that have the following properties:

$$\langle \mathrm{A}_k(t), \mathrm{A}_m(t) \rangle = \int_T \mathrm{A}_k(t)\, \mathrm{A}^*{}_m(t) dt = \delta[k-m] = \begin{cases} 1 & k = m \\ 0 & k \neq m \end{cases} \tag{2.1}$$

where $*$ denotes the complex conjugate. Generalized Fourier Series (GFS) enable the representation of a given function $f(t)$ defined in this space as an infinite series of the following form:

$$f(t) = \sum_{n=-\infty}^{\infty} C_k \mathrm{A}_k(t) \tag{2.2}$$

where $\mathrm{A}_k(t)$ denotes the complete set of orthonormal basis functions and C_k are the coefficients of the GFS. The coefficients C_k are obtained by performing an inner product of the function $f(t)$ with the basis functions $\mathrm{A}_k(t)$ as shown in Eq. (2.3):

$$C_k = \int_T f(t)\,\mathrm{A}^*{}_k(t)dt \tag{2.3}$$

In other words, the kth coefficient (i.e., C_k) is the projection of $f(t)$ onto the kth basis function $\mathrm{A}_k(t)$. As one can imagine, the basis functions $\mathrm{A}_k(t)$ can be many different options. However, selecting e^{ikt} as a basis function is quite useful if the function of interest $f(t)$ is periodic. A function $f(t)$ is periodic when the following relationship is satisfied:

$$f(t) = f(t+p) \tag{2.4}$$

where p is a positive number that represents a period after which the function repeats itself. As a result, $f(t)$ is assumed to be represented as an infinite series sum of harmonic functions (i.e., cosine and sine functions) as Eq. (2.5) shows:

$$f(t) = \sum_{n=-\infty}^{\infty} F_k e^{\frac{2\pi ikt}{p}} \tag{2.5}$$

where $i = \sqrt{-1}$. Notice that F_k simply denote amplitudes of different frequencies indexed by k, given the fact that $e^{\frac{2\pi ikt}{p}} = \cos(\frac{2\pi kt}{p}) + i\sin(\frac{2\pi ikt}{p})$. In other words, this Fourier series enables one to transform a function $f(t)$ defined in the space t to the frequency space.

2.1.1 The Fourier Transform

The Fourier transform enables the transformation of a function $f(t)$ to the frequency space by leveraging the orthonormality of the basis functions as follows:

$$F_k = \frac{1}{2\pi}\int_0^{2\pi} f(t)\, e^{-ikt} dt \tag{2.6}$$

where the periodicity period is assumed to be 2π. Nevertheless, note that the period of periodicity can be suitably modified to accommodate for any periodic period p.

2.1.2 Discrete Fourier Transform

As it can be observed GFS are an extremely powerful tool to represent a mathematical function $f(t)$. Nevertheless, the series expansion requires an infinite number of terms. A special variation of the Fourier series concept, called the Discrete Fourier Transform (DFT) enables for one to circumvent this impasse by establishing the complimentary representation in the frequency space of a finite number of discrete evaluations of the function $f(t)$. In other words, assume that the function $f(t)$ has been defined on a discrete grid of points x_n, where n takes the value from 0 to $N-1$, such that f_n denotes the value of $f(t)$ evaluated at x_n. The DFT representation then provides a one-to-one mapping between the representation of f_n in the frequency space (i.e., F_k) with the aid of the following expression:

$$F_k = \Im(f_n) = \sum_{n=0}^{N} f_n\, e^{\frac{2\pi ikn}{N}} \tag{2.7}$$

The relationship that transforms from frequency space back to the real space is the following:

$$f_n = \Im^{-1}(F_k) = \frac{1}{N}\sum_{k=0}^{N-1} F_k \, e^{\frac{2\pi i k n}{N}} \tag{2.8}$$

where $\Im()$ denotes the DFT mapping and $\Im^{-1}()$ the inverse DFT mapping. The relationships denoted by Eqs. (2.7-2.8) are capable of being extended for functions with multiple independent variables in a trivial manner. It is important to mention that in order for the function to be faithfully represented with a DFT it is necessary for the sampling frequency (i.e. the spacing of the grid used to discretize $f(t)$) to be able of capturing the highest frequency component of the data. As a result, the Nyquist frequency, which is defined as half of the sample frequency, should be greater than or equal to the highest frequency component of the function in order to ensure an accurate representation. Finally, it should be acknowledged that the DFT representation only becomes practical when computed using a special algorithm called Fast Fourier Transform (FFT) that leverages the inherent symmetries present in the transformation to compute it efficiently.

The DFT representation has many properties that can be leveraged to ease analysis in a wide array of fields. The convolution and correlation of two functions, $f(t)$ and $g(t)$, obtained using DFT representations are heavily leveraged throughout this dissertation and is easily obtained using the following expressions (for proof cf. [52]):

$$\mathrm{Conv}(f,g) = \sum_{s=0}^{N-1} f_s g_{r-s} = \Im^{-1}(F_k G_k) \tag{2.9}$$

$$\mathrm{Corr}(f,g) = \sum_{s=0}^{N-1} f_s g_{r+s} = \Im^{-1}(F_k {G^*}_k) \tag{2.10}$$

2.1.3 Trigonometric Interpolation

An extremely powerful property of DFT representations is the ability to obtain values of a continuous function $f(t)$ at new points in the domain of interest, apart from the sampling points where the function values were already known and that were leveraged to procure the DFT representation. One specific approach central to the formalisms developed in this dissertation is trigonometric interpolation. The interpolation scheme takes advantage of the DFT representations to perform an interpolation with global support. The trigonometric interpolation for a function $f(t)$ is obtained with the following relationship:

$$f(t) = \frac{1}{N} \sum_{k=-\frac{N}{2}+1}^{\frac{N}{2}} F_k \, e^{\frac{2\pi i k t}{p}} \tag{2.11}$$

where N denotes the total number of grid points on which the function $f(t)$ was originally sampled, p denotes the periodicity of the function and F_k are the DFT coefficients of the function at the grid points. It is important to notice that the output of this interpolation is a continuous function, which attests to the power of this interpolation since it enables for one to procure the value of the function at any desired point. Moreover, this interpolation is extremely well suited for interpolation of periodic functions discretized on a regular grid.

2.2 Digital Representation of the Microstructure

A mathematical representation of the internal structure of the material is needed in order to be capable of quantifying the effect that different spatial arrangements/distributions of microstructural features (i.e., grains) have on the overall response (i.e., plastic deformation) of the material. The microstructure function is a function that enables the mathematical representation of

the internal structure of a material [7, 41]. The set of physical characteristics of the internal structure is called local state and can have many different descriptors such as phase, chemical composition, crystal lattice orientation, crystal structure, etc. The derivations and expressions developed in this dissertation denote the physical descriptor of interest with the variable n. Thus, the microstructure function, $m(\boldsymbol{x}, n)$, prescribes the probability density associated with finding a determined local state n (within an invariant measure dn) at an infinitesimal neighborhood of the material point $\boldsymbol{x}$ and is formally defined by the following relationship:

$$m(\boldsymbol{x}, n)dn = \frac{dV}{V} \tag{2.12}$$

The microstructure function is most suitably represented using generalized Fourier series (GFS) since it has the flexibility to incorporate any arbitrary level of detail desired to be included into the description of the microstructure's feature geometries and local states. It is important to recognize that experimental characterization of the internal structure of a material of interest inherently provides discrete measurements because it rasterizes the local state with a characteristic minimum resolved length-scale defined by the resolution of the specific machine used to acquire the information[41]. As one can imagine, different local state descriptors require different GFS to represent the microstructure function.

2.2.1 Digital Representation of Multiphase Composites

Multiphase composites are comprised by two or more thermodynamically distinct phases (labeled $\alpha, \beta, \ldots$). As such, one can describe the local state space with a set that lists each of the phases (i.e., enumerated by a discrete variable h). The most adequate GFS representation of the microstructure function for this type of materials is the following:

$$m(\boldsymbol{x}, n)\Delta n \approx \sum_{n=1}^{N}\sum_{\boldsymbol{s}=1}^{\boldsymbol{S}} m_{\boldsymbol{s}}^{h}\chi_h(n)\chi_{\boldsymbol{s}}(\boldsymbol{x}) \tag{2.13}$$

where $m_{\boldsymbol{s}}^{h}$ are the coefficients of the GFS used, Δn is the size of the local state bin, and $\chi_i()$ denotes an indicator basis function. An indicator basis function returns a value of one if the argument of the function is within the bin indexed by i. Otherwise it returns a value of zero. This GFS representation amounts to discretizing the spatial domain by tessellating it into voxels (spatial cells) of uniform volume enumerated by $\boldsymbol{s} \in \boldsymbol{S}$ and to consider each thermodynamic phase as a binned local state $h \in H$. It is important to mention that N and $\boldsymbol{S}$ indicate the maximum number of phases and spatial locations being considered in the description of the microstructure. Notice also that $\boldsymbol{s}$ can be treated as a vector index for multidimensional domains. For example, in the case of 3D microstructures $\boldsymbol{s}$ can be considered as a three-index vector (i.e. $\boldsymbol{s} = (s_1, s_2, s_3)$).

2.2.2 Digital Representation of Polycrystalline Microstructures

The local state for a general polycrystalline material might encompass various different descriptors (i.e. crystal symmetry, orientation, dislocation density, chemical composition, etc.). For the specific case of single-phase polycrystalline materials, the local state can be adequately determined by the orientation of the crystal lattice. The orientation of the crystal lattice is suitably represented with three different angles $({\varphi_1}^c, \Phi^c, {\varphi_2}^c)$ commonly referred as Bunge-Euler angles[51] and typically compacted into a single continuous variable g. The probability density of an arbitrary orientation g, also known as the orientation distribution function $f(g)$, is used to determine the local state of polycrystalline materials. Therefore, $f_s(g)dg$ indicates the spatially resolved orientation distribution function (ODF) for a spatial bin s. In other words, $f_{\boldsymbol{s}}(g)dg$ indicates the probability that the material located in spatial bin $\boldsymbol{s}$ is characterized by the crystal lattice

orientations that exist within dg around g. With this definition one can clearly see the correspondence between $f_s(g)dg$ and m_s^h.

Generalized Spherical Harmonics (GSH) are a Fourier basis that enable a computationally efficient handling for functions defined in the orientation space (i.e. $f(g)dg$)[45]. The GSH Fourier basis, $T_l^{mn}(g)$, are defined as follows:

$$T_l^{mn}(g) = T_l^{mn}({\varphi_1}^c, \Phi^c, {\varphi_2}^c) = e^{im{\varphi_1}^c} P_l^{mn}(\Phi^c) e^{im{\varphi_2}^c} \tag{2.14}$$

where $P_l^{mn}(\Phi^c)$ are certain generalization of Legendre functions [51] and $({\varphi_1}^c, \Phi^c, {\varphi_2}^c)$ are the previously introduced Bunge-Euler angles. The functions described by the GSH basis (Eq. 2.14) form an orthonormal basis [41, 45, 51]:

$$\oint T_l^{mn} T_{l'}^{m'n'*} dg = \frac{1}{2l+1} \delta_{ll'} \delta_{mm'} \delta_{nn'} \tag{2.15}$$

where dg is the invariant measure of the orientation space and $*$ denotes the complex conjugate. The GSH basis functions can be further customized to depict any specific crystal and sample symmetry of interest by simply taking a linear combination of the previously introduced GSH functions[7, 51]. As a specific example let $\dot{T}_l^{\mu n}$ denote the symmetrized GSH functions for cubic-triclinic symmetry. The $\dot{T}_l^{\mu n}$ functions are obtained with the following expression:

$$\dot{T}_l^{\mu n} = \sum_{m=-l}^{l} \dot{A}_l^{m\mu} T_l^{mn} \tag{2.16}$$

where $\dot{A}_l^{m\mu}$ denote the coefficients of the symmetrized GSH functions that exhibit the desired symmetry (cubic-triclinic). Taking advantage of the orthogonality of the GSH functions one can

compactly represent the functions defined in the orientation space and efficiently compute any mathematical operation of interest on them. As an example:

$$f_{\boldsymbol{s}}(g) = \sum_{\mu,n,l} F_{l\boldsymbol{s}}^{\mu n}\, \dot{T}_l^{\mu n}(g),$$
$$F_{l\boldsymbol{s}}^{\mu n} = (2l+1)\int_{FZ} f_{\boldsymbol{s}}(g)\dot{T}_l^{\mu n*}(g)dg \tag{2.17}$$

where $F_{l\boldsymbol{s}}^{\mu n}$ are the respective GSH (Fourier) coefficients of $f_{\boldsymbol{s}}(g)$. The corresponding GSH coefficients of $f_{\boldsymbol{s}}(g)$ for the specific case where a single lattice orientation g_0 is present in a spatial bin $\boldsymbol{s}$ are obtained by:

$$F_{l\boldsymbol{s}}^{\mu n} = (2l+1)\dot{T}_l^{\mu n*}(g_0) \tag{2.18}$$

2.3 Spatial Statistics

Spatial statistics in the form of n-point spatial correlations are capable of characterizing lower- and higher-order spatial relationships between features of the internal structure of a material. Additionally, they inherently capture a majority of the ad-hoc metrics employed in the literature. As a result, n-point spatial correlations enable a robust mathematical comparison of the internal structures of different materials. Two-point spatial correlations describe the probability of finding two local states (indexed by h and h', respectively) in two different spatial locations separated by a vector indexed by $\boldsymbol{r}$. The mathematical representation of the microstructure introduced previously in this section allows one to express the 2-point statistics of a periodic microstructure as follows:

$$f_{\boldsymbol{r}}^{hh'} = \frac{1}{|\boldsymbol{S}|}\sum_{\boldsymbol{s}=1}^{\boldsymbol{S}} m_{\boldsymbol{s}}^{h} m_{\boldsymbol{s}+\boldsymbol{r}}^{h'} \tag{2.19}$$

where $|\boldsymbol{S}|$ denotes the total number of voxels (spatial bins) present in the spatial domain. This dissertation leverages two-point statistics since previous work has demonstrated that they are sufficient to perform a robust comparison between different internal structures [46, 54, 55].

2.4 Multiple Linear Regression

The central tool used in this dissertation to calibrate the values of the microstructure-independent localization kernels (explained in detail in Chapter 3) is Multiple or Multivariate Linear Regression. This specific model of regression describes a linear relationship between a single response variable y (e.g., the value of a tensor component at a specific point on the microstructure of interest) and more than two predictor variables (e.g., the coefficients associated with a GFS). It is important to recognize that even though the relationship between the defined predictor variables and the output is linear, the predictor variables can be non-linear terms (for example the cosine and sine terms of a Fourier series that uses e^{ikt} as a basis function).

As an example, consider the following model that describes a single variable response y as a linear combination of q independent predictor variables $x_1, \ldots, x_q$ as Eq. (2.20) shows:

$$y_i = \beta_0 + \beta_1 x_1 + \ldots + \beta_q x_{qi} + e_i \tag{2.20}$$

where i indexes the ith observation (assume that n observations are recorded for the $q+1$ variables of interest, where $n > q$), β_q denote the regression coefficients that establish the linear relationship between the single variable response and the q independent variables, and e_i denote

the associated error term. One can express the linear relationship described in Eq. (2.20) in matrix notation as follows:

$$\boldsymbol{y} = \boldsymbol{X\beta} + \boldsymbol{e} \tag{2.21}$$

Linear regression determines the value of the predictor variables by minimizing the sum of the squared error terms using Ordinary Least Square Regression (OLS). One can think of OLS regression as fitting a hyper-plane in a $q + 1$ dimensional space that minimizes the sum of the squared errors. The general expression obtained using OLS to find the values of the $\boldsymbol{\beta}$ coefficients is the following:

$$\boldsymbol{\beta} = (\boldsymbol{X^T X})^{-1}(\boldsymbol{X^T y}) \tag{2.22}$$

For a more detailed and thorough explanation of the derivation of this model please cf. [53].

2.5 Representative Volume Element

A representative volume element (RVE) [41, 56] identifies a finite region that has been sampled randomly from an infinite medium. The identified region is "statistically representative" of the whole medium, while also capturing the microstructural salient features with a sufficient accuracy [41, 57-61]. This concept is central to any multiscale effort since it is the region over which the loading conditions are applied, it is also the region where the localization reduced-order models predict the response field and finally because the different length scales are integrated by exchanging information between RVEs at different length scales with the aid homogenization and localization models (as Figure 1 shows)[41, 56].

CHAPTER 3:

Generalized Material Knowledge Systems Framework for Localization

This chapter provides an overview of the generalized MKS framework for localization as well as the details for extending this framework into plastic deformations.

3.1 Theoretical Foundations of the MKS Framework for Localization

The theoretical foundation behind the localization models developed with the MKS framework is the localization tensor. This tensor is defined on the generalized composite theories that determine the effective response of heterogeneous materials [39, 40, 62-65] and is employed to link the fields at a lower length scale to a boundary condition imposed at a higher length scale. An example of such localization tensor is the fourth-rank elastic localization tensor ($\boldsymbol{a}(\boldsymbol{x})$), which relates the local elastic strain at any location of interest ($\boldsymbol{\varepsilon}(\boldsymbol{x})$) to the macroscopically imposed strain ($\langle\boldsymbol{\varepsilon}(\boldsymbol{x})\rangle$) in the following fashion [41]:

$$\boldsymbol{\varepsilon}(\boldsymbol{x}) = \boldsymbol{a}(\boldsymbol{x})\langle\boldsymbol{\varepsilon}(\boldsymbol{x})\rangle \tag{3.1}$$

and $\boldsymbol{a}(\boldsymbol{x})$ is defined as follows:

$$\boldsymbol{a}(\boldsymbol{x}) = (\boldsymbol{I} - \langle\boldsymbol{\Gamma}^r(\boldsymbol{x},\boldsymbol{x}')\mathbf{C}'(\boldsymbol{x}')\rangle + \langle\boldsymbol{\Gamma}^r(\boldsymbol{x},\boldsymbol{x}')\mathbf{C}'(\boldsymbol{x}')\boldsymbol{\Gamma}^r(\boldsymbol{x}',\boldsymbol{x}'')\mathbf{C}'(\boldsymbol{x}'')\rangle - \cdots) \tag{3.2}$$

where $\boldsymbol{I}$ denotes the fourth-rank identity tensor, $\mathbf{C}'(\boldsymbol{x})$ denotes the perturbation in the local stiffness with respect to a selected reference medium, $\boldsymbol{x}$ is the spatial location of interest in the microstructure RVE, $\boldsymbol{\Gamma}^r$ is a symmetrized derivative of the Green's function corresponding to the elastic properties of the selected reference medium, and the $\langle\cdots\rangle$ brackets denote ensemble average over the RVE being studied (i.e., these brackets essentially represent volume averages over the RVE). Eq. (3.2) shows that the localization tensor can be obtained by evaluating the terms of an

infinite series. In this series, one systematically adds the contribution from other spatial locations in the material microstructure to the localization tensor at the spatial location of interest. For example, the second term captures the contribution from spatial location $\boldsymbol{x}'$ on $\boldsymbol{a}(\boldsymbol{x})$, modulated through the kernel $\boldsymbol{\Gamma}^{\boldsymbol{r}}$ that decays sharply with $|\boldsymbol{x}' - \boldsymbol{x}|$**.** In a very similar manner, the next term captures the combined incremental contribution from spatial locations $\boldsymbol{x}'$ and $\boldsymbol{x}''$ on $\boldsymbol{a}(\boldsymbol{x})$ tensor, once again suitably modulated through Green's function based kernels. It is important to recognize that these terms capture systematically and hierarchically the spatial correlations in the material microstructure.

Although the physics-based models presented in Eq. (3.1) and Eq. (3.2) are rigorously derived, their practical implementation in real-world applications has been hampered by the inability to establish the $\boldsymbol{\Gamma}^{r}$ kernels for a broad range of materials phenomena of interest with sufficient accuracy due to the following issues [7, 41, 63, 66-70]:

1. The computation of the ensemble averages ($\langle \cdots \rangle$ terms) actually require the evaluation of complex convolution integrals whose terms exhibit singularities, commonly referred as the Principal Value Problem.
2. The accuracy of the solutions obtained depends heavily on the selection of the reference media employed to define the Green's Function solution.
3. The expression of the localization tensor from Eq. 3.2 is not suitable for carrying forward to different microstructures calculations that were performed on a previous microstructure. Meaning that most of the terms in the expression would need to be reevaluated to obtain results for a different microstructure.

The MKS localization framework addressed these issues by leveraging GFS to obtain suitable mathematical representations of the functions comprised in Eq. (3.2) and to decouple the

localization relationship into physics-capturing microstructure-independent kernels (also called localization kernels that are related to $\boldsymbol{\Gamma^r}$) and terms that capture the microstructure topology [7, 41, 43, 45, 48, 49]. As a result, Eq. (3.2) can be casted into the following form by suitably representing $\boldsymbol{a}(\boldsymbol{x})$ with GFS, invoking ergodic hypothesis and substituting $\boldsymbol{r} = \boldsymbol{x} - \boldsymbol{x}'$ and $\boldsymbol{r} = \boldsymbol{x}' - \boldsymbol{x}''$:

$$\boldsymbol{a}(\boldsymbol{x}) = \left(I - \int_R \int_N \boldsymbol{\alpha}(\boldsymbol{r}, n) m(\boldsymbol{x} + \boldsymbol{r}, n) dn d\boldsymbol{r} + \int_R \int_R \int_N \int_N \widetilde{\boldsymbol{\alpha}}(\boldsymbol{r}, \boldsymbol{r}', n, n') m(\boldsymbol{x} + \boldsymbol{r}, n) m(\boldsymbol{x} + \boldsymbol{r} + \boldsymbol{r}', h') dn dn' d\boldsymbol{r} d\boldsymbol{r}' - \cdots\right) \tag{3.3}$$

where $\boldsymbol{\alpha}(\boldsymbol{r}, n)$ denotes the microstructure-independent localization kernel (related to $\boldsymbol{\Gamma^r}$) and $m(\boldsymbol{x}, n)$ denotes the previously defined microstructure function (cf. Chapter 2). Notice also that Eq. (3.3) casts the localization relationship as an infinite series sum of convolutions between the microstructure-independent localization kernels and the spatial correlations of the material microstructure (captured by the microstructure function $m(\boldsymbol{x}, n)$). As a result, these convolutions can be most efficiently computed leveraging DFT representations (cf. Eq. (2.7-2.9)). It is needless to mention the remarkable complications that an analytical evaluation of the localization kernels denoted in Eq. (3.3) will have. For that reason, the MKS localization framework discretizes the functions present in the localization relationship depicted in Eq. (3.3) using suitable GFS to enable a direct calibration of the kernels to numerical simulations (e.g. FEM) performed on ensembles of digitally created microstructures. Thus, the volumetric domain of the microstructure is binned into a uniform grid of voxels (spatial cells) enumerated by $\boldsymbol{s} \in \boldsymbol{S}$ (as stated earlier in Chapter 2 this index can be treated as a vector index for multidimensional domains). Subsequently, the potential material states, also called local states, allowed to occupy each spatial voxel are indexed by $h \in$

H. As a result, the array $m_{\boldsymbol{s}}^{h}$ reflects the volume fraction of spatial bin $\boldsymbol{s}$ occupied by local state n (cf. [58, 60, 71]) as an array of discrete values. A similar discretization is performed over the spatial domain and the local state space of the influence kernel function ($\boldsymbol{\alpha}(\boldsymbol{r}, n)$) to obtain an array of discrete values denoted by $\boldsymbol{\alpha}_{\boldsymbol{t}}^{h}$. Notice that the strategy employed to discretize these continuous functions corresponds to a GFS representation of the functions using indicator basis functions as the following equations show:

$$m(\boldsymbol{x}, n)\Delta n \approx \sum_{n=1}^{N}\sum_{\boldsymbol{s}=1}^{\boldsymbol{S}} m_{\boldsymbol{s}}^{h}\chi_{h}(n)\chi_{\boldsymbol{s}}(\boldsymbol{x}) \tag{3.4a}$$

$$\boldsymbol{\alpha}(\boldsymbol{r}, n)\Delta n \approx \sum_{n=1}^{N}\sum_{\boldsymbol{s}=1}^{\boldsymbol{S}} \mathbf{A}_{\boldsymbol{s}}^{h}\chi_{h}(n)\chi_{\boldsymbol{s}}(\boldsymbol{x}) \tag{3.4b}$$

As a result, the GFS representation enables the MKS framework to discretize the localization relationship depicted in Eq. (3.3) and recast it into the following form:

$$\boldsymbol{p}_{\boldsymbol{s}} = \left(\sum_{h}^{H}\sum_{\boldsymbol{t}}^{\boldsymbol{S}} \boldsymbol{\alpha}_{\boldsymbol{t}}^{h} m_{\boldsymbol{s}+\boldsymbol{t}}^{h} + \sum_{h}^{H}\sum_{h'}^{H}\sum_{\boldsymbol{t}}^{\boldsymbol{S}}\sum_{\boldsymbol{t}'}^{\boldsymbol{S}} \boldsymbol{\alpha}_{\boldsymbol{t}\boldsymbol{t}'}^{hh'} m_{\boldsymbol{s}+\boldsymbol{t}}^{h} m_{\boldsymbol{s}+\boldsymbol{t}+\boldsymbol{t}'}^{h'} + \cdots\right)\langle \boldsymbol{p}\rangle \tag{3.5}$$

where $\boldsymbol{p}$ denotes the response field of interest (e.g., strain, strain rate), $\boldsymbol{\alpha}$ are the microstructure-independent localization kernels (related to $\boldsymbol{\Gamma}^{r}$) and $m_{\boldsymbol{s}}^{h}$ is the microstructure function. In this notation, $\boldsymbol{t}$ indexes the discretized vectors needed to identify the relative location of all the voxels in the RVE with respect to the voxel of interest (denoted by $\boldsymbol{s}$). For a uniformly tessellated periodic RVE, the set of values taken by $\boldsymbol{t}$ are identical to the values taken by $\boldsymbol{s}$ (i.e., $\boldsymbol{t} \in \boldsymbol{S}$). It is important to recognize that the localization relationship is now defined as an infinite series sum of arrays of discrete values and as such a numerical evaluation of the relationship is possible. The first order

localization kernels ($\boldsymbol{\alpha}_{\boldsymbol{t}}^{h}$) capture the influence of local state h on a voxel separated by a vector $\boldsymbol{t}$ from spatial voxel $\boldsymbol{s}$. Similarly, the second order localization kernels ($\boldsymbol{\alpha}_{\boldsymbol{tt'}}^{hh'}$) capture the combined incremental contribution of local states h and h' on voxels separated by vectors $\boldsymbol{t}$ and $\boldsymbol{t}'$, respectively, from spatial voxel $\boldsymbol{s}$. As a result, the calibrated series expansion expressed in Eq. (3.5) systematically and hierarchically captures the contribution of the local states at other spatial locations in the material microstructure to the local value of the response at the spatial voxel $\boldsymbol{s}$.

The MKS framework calibrates the values of the localization kernels ($\boldsymbol{\alpha}$) from numerical results obtained from validated physics-based models (i.e. FEM) over a broad range of microstructures. The main advantage of the decoupled localization relationship portrayed in Eq. (3.5) is that once the localization kernels have been calibrated they can be subsequently employed to predict the results of new microstructures with very little computational cost, as well as with negligible loss in accuracy[7, 41-45]. The detailed derivation of Eqs. (3.1-3.5), and the mathematical formulation of MKS can be found in prior publications (cf. [41, 43, 49, 72]). Figure 2 schematically depicts the steps taken by the MKS framework to obtain the microstructure-independent localization kernels.

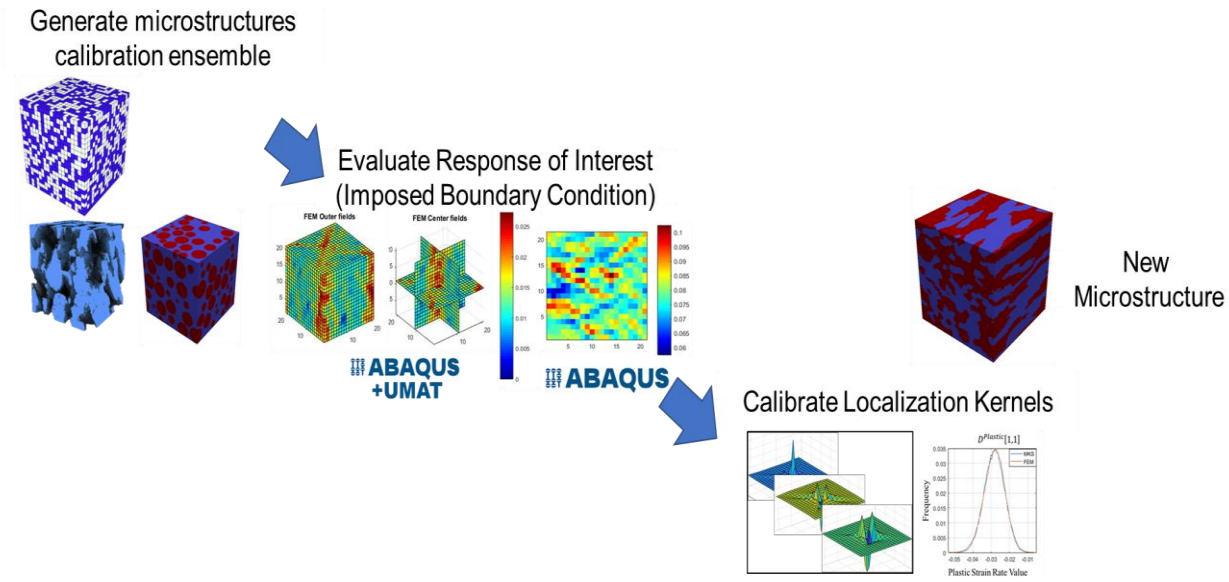

Figure 2: Flowchart of the Process by which the MKS Localization Kernels are Calibrated to Numerical Results of Previously Validated Physics-based Models.

The viability and remarkable accuracy of the microstructure-independent localization kernels obtained following the protocol outlined in Figure 2 has been demonstrated on a broad range of multiscale materials phenomena [43-46, 48, 49]. It is important to mention that the localization relationship employed for the mentioned worked used only the first order localization kernel since the microstructure of interest depicted low to moderate contrast between the properties exhibited by the local states. In other words, the heterogeneity of the response field was limited and as such the physics captured with the first order kernels were sufficient to procure an accurate prediction of the field.

3.2 MKS Localization Framework Implementation to Plastic Deformation

The success and accuracy of the MKS framework coupled with the fact that the statistical continuum theories on which this framework is based have been successfully applied to non-linear phenomena [73, 74] ascertain that this framework is capable of localizing the plastic response. As

a matter of fact, previous work demonstrated that providing the contrast between the composite phases is low, (such that the first order kernels are sufficient to procure an accurate response) the MKS framework is capable to accurately localize the response of a specific loading condition of a rigid-plastic deformation in a composite material made of two isotropic phases [43].

For the localization of the plastic response, the response field is selected as the strain rate tensor (i.e., $\boldsymbol{p} = \boldsymbol{D}$). Therefore, the relationship that localizes the plastic response, using an indicator basis function to discretize the relationship, is the following:

$$\boldsymbol{D_s} = \left(\sum_{h}^{H} \sum_{\boldsymbol{t}}^{\boldsymbol{S}} \boldsymbol{\alpha}_{\boldsymbol{t}}^{h}(\langle \boldsymbol{D} \rangle) m_{\boldsymbol{s+t}}^{h} + \sum_{h}^{H} \sum_{h'}^{H} \sum_{\boldsymbol{t}}^{\boldsymbol{S}} \sum_{\boldsymbol{t'}}^{\boldsymbol{S}} \boldsymbol{\alpha}_{\boldsymbol{tt'}}^{hh'}(\langle \boldsymbol{D} \rangle) m_{\boldsymbol{s+t}}^{h} m_{\boldsymbol{s+t+t'}}^{h'} + \cdots \right) \tag{3.6}$$

where $\boldsymbol{D_s}$ denotes the spatially resolved strain rate tensor (i.e., stretching tensor) in the microstructure, and the dependence of the Green's function based kernel $\boldsymbol{\alpha}$ on the macroscopically imposed strain rate tensor ($\langle \boldsymbol{D} \rangle$) is explicitly noted. The current MKS approach, depicted graphically in Figure 2, requires for one to establish a different localization kernel for each $\langle \boldsymbol{D} \rangle$ that can be applied at the macroscale (on the RVE of the microstructure). The number of distinct macroscopic strain rate tensors that could be imposed on a microstructure is infinite. Consequently, a direct implementation of the current MKS framework is not feasible. Therefore, it is essential to seek a formalism that enables an efficient computation/calibration of $\boldsymbol{\alpha}$ as a function of $\langle \boldsymbol{D} \rangle$. It must be acknowledged that prior MKS work on the elastic deformations in composites and polycrystalline materials circumvented this challenge by taking advantage of the superposition principle. However, superposition principle is not applicable to the plastic deformations.

This dissertation develops and demonstrates a novel approach that enables the kernels to localize any arbitrary periodic boundary condition imposed at the macroscale in an efficient

fashion. This dissertation developed this formalism in two-phase composite systems and subsequently implements it to single-phase, cubic, FCC materials. Thus, successfully developing a computationally efficient/inexpensive, yet robust, computational framework capable of predicting the anisotropic plastic response of polycrystalline microstructures.

CHAPTER 4:

Localization Models for Predicting the Local Plastic Response Caused by An Arbitrary Periodic Boundary Condition Imposed at the Macroscale Using the Material Knowledge Systems Framework

The plastic response of a material is inherently non-linear and path-dependent. As a result, plasticity constitutive laws relate the state of stress to increments in strain, or to the strain rate [75]. Eq. (3.6) clearly denotes that the localization kernels are dependent on the macroscopically imposed strain rate $\langle \boldsymbol{D} \rangle$. Therefore, in order to establish a formalism for an efficient computation of $\boldsymbol{\alpha}$ as a function of $\langle \boldsymbol{D} \rangle$ it is first needed to define a suitable parameterization of the function space spanned by the imposed stretching tensor. This section describes a strategy that enables a suitable parametrization of the function space spanned by the macroscopically imposed stretching tensor in order to establish a finite, and sufficiently accurate, spectral database of localization kernels capable of capturing this entire space. As a result, the MKS framework will be capable to efficiently localize any arbitrary strain rate tensor imposed at the macroscale (i.e. an infinite set of loading conditions) with a finite spectral database of localization kernels ($\boldsymbol{\alpha}$). The strategy defined in this Chapter is inspired by certain prior applications in related problems [76-79] and is expounded on [80].

4.1 Extension of the Generalized MKS Localization Framework for Localizing Any Arbitrary Periodic Boundary Condition Imposed at the Macroscale

The clever parametrization of the stretching tensor will be performed in in two-phase composite systems subjected to rigid-plastic deformation. It has been assumed that the constituent phases of these systems exhibit rate-independent isotropic plasticity described by the commonly employed J_2 flow theory [81]. It should be noted that even though the selection of this simple

material constitutive theory constrains the local plastic response to be isotropic, the overall behavior of the composite is allowed to be anisotropic. The J_2 flow theory for the plastic deformation under the listed assumptions (rate-independent, isotropic and rigid-plastic) starts with the Levy-Misses relation for each constituent phase [75]:

$$\boldsymbol{D} = \lambda \boldsymbol{\sigma'} \tag{4.1}$$

where λ is related to the magnitude of the imposed plastic strain rate and $\boldsymbol{\sigma'}$ is the strain rate-independent deviatoric component of the symmetric Cauchy stress tensor. In other words, in this formulation, λ scales linearly with $|\boldsymbol{D}|$, while $\boldsymbol{\sigma'}$ is unaffected by $|\boldsymbol{D}|$ for a selected direction of $\boldsymbol{D}$. An important consequence of this feature in the rigid-plastic constitutive behavior (based on J_2 flow theory) is that the partitioning of the imposed strain rate on a two-phase composite is such that the local strain rate tensor scales linearly with the magnitude of the macroscale imposed strain rate tensor for any selected direction of this tensor. One can reach this conclusion simply by recognizing the fact that this simple solution satisfies both compatibility (all local strain components are scaled by the same factor) and equilibrium (as stresses are unaffected) throughout the microstructure. As a result, the localization relationship for the plastic response can now be casted into the following form:

$$\boldsymbol{D_s} = \left(\sum_{h}^{H} \sum_{\boldsymbol{t}}^{\boldsymbol{S}} \boldsymbol{\alpha}_{\boldsymbol{t}}^{h}(\boldsymbol{d}) m_{\boldsymbol{s+t}}^{h} + \sum_{h}^{H} \sum_{h'}^{H} \sum_{\boldsymbol{t}}^{\boldsymbol{S}} \sum_{\boldsymbol{t'}}^{\boldsymbol{S}} \boldsymbol{\alpha}_{\boldsymbol{tt'}}^{hh'}(\boldsymbol{d}) m_{\boldsymbol{s+t}}^{h} m_{\boldsymbol{s+t+t'}}^{h'} + \cdots \right) |\langle \boldsymbol{D} \rangle| \tag{4.2}$$

where $\boldsymbol{d} = \frac{\langle \boldsymbol{D} \rangle}{|\langle \boldsymbol{D} \rangle|}$. Notice how the kernels $\boldsymbol{\alpha}$ depend only on the direction (unit magnitude) of the imposed symmetric traceless strain rate tensor, $\boldsymbol{d}$. It can be seen that this specific formulation reduces significantly the domain space on which the MKS kernels need to be defined.

The strain-rate direction tensor ($\boldsymbol{d}$) is a symmetric second rank tensor, which guarantees real Eigen values and therefore the existence of a Principal Frame [75, 82]. Let d_{ij}^{SF} and d_{ij}^{PF} denote the components of this tensor in the sample frame and the principal frame, respectively. Note that the off-diagonal terms of d_{ij}^{PF} are zeros. As a result, the complete space of $\boldsymbol{d}$ can be efficiently parametrized using four angles represented as $(\varphi_1, \Phi, \varphi_2, \theta)$ [76-79]. The first three angles $(\varphi_1, \Phi, \varphi_2)$, hereafter referred as Euler angles, describe the orientation of the principal frame with respect to the sample reference frame. The fourth angle (θ) identifies the principal values while taking advantage of the unit magnitude and zero trace of $\boldsymbol{d}$ [76]. Using this parametrization, one can show that:

$$\left[d_{ij}^{PF}\right] = \sqrt{\frac{2}{3}}\begin{bmatrix} \cos(\theta - \frac{\pi}{3}) & 0 & 0 \\ 0 & \cos(\theta + \frac{\pi}{3}) & 0 \\ 0 & 0 & -\cos\theta \end{bmatrix} \tag{4.3}$$

and

$$d_{ij}^{SF} = Q_{ik}Q_{jl}d_{kl}^{PF} \tag{4.4}$$

where Q_{ij} defines the transformation matrix from the principal frame to the sample reference frame and Einstein's notation is employed for implied summation on repeated indices. The transformation matrix is defined through the dot products of the basis vectors in the sample and principal frames and is expressed as products of sines and cosines of the Euler angles $(\varphi_1, \Phi, \varphi_2)$.

A significant benefit of this parameterization is that the domain of $\boldsymbol{d}$ is now represented by a four-dimensional space over which all physically-based functions of interest exhibit periodicity.

Indeed, this is a central element of our strategy for developing a rigorous, compact, and sufficiently accurate spectral database for capturing $\boldsymbol{\alpha}_{\boldsymbol{t}}^{h}(\boldsymbol{d})$.

Taking advantage of the novel parametrization and assuming that the phases of the composite exhibit a low to moderate contrast between their local plastic properties (i.e. the ratio between their yield strengths), the MKS localization relationship can be truncated to the first order terms and casted into to the following expression:

$$\boldsymbol{D}_{\boldsymbol{s}} = \left(\sum_{h}^{H} \sum_{\boldsymbol{t}}^{\boldsymbol{S}} \boldsymbol{\alpha}_{\boldsymbol{t}}^{h}(\varphi_1, \Phi, \varphi_2, \theta) m_{\boldsymbol{s}+\boldsymbol{t}}^{h} \right) |\langle \boldsymbol{D} \rangle| \tag{4.5}$$

It is important to recognize that Eq. 4.5 is a tensorial equation valid in any reference frame. Nevertheless, it is to be used in the sample reference frame, since this is the frame on which the response is desired to be localized.

4.2 Calibration of a Finite Set of Localization Kernels in the Principal Frame of the Imposed Periodic Boundary Condition

The calibration of the localization linkage in the sample frame requires discretizing, and sampling of the localization kernel, $\boldsymbol{\alpha}_{\boldsymbol{t}}^{h}$, in a four-dimensional space (see Eq. (4.5)). However, the required effort can be significantly reduced if the kernel is established in the principal frame of the tensor $\boldsymbol{d}$, since it would then be dependent on a single parameter, θ (see Eqs. (4.3) and (4.4)). In addition to reducing the effort involved, the kernel established in the single parameter space would result in a compact database. Such a compact representation of the localization kernel would reduce significantly the computational memory in the applications of the MKS approach.

An extended notation is leveraged to describe clearly the important details involved in establishing a finite and compact database of MKS localization kernels. The extended notation

denotes the quantities of interest as multi-dimensional arrays. As an example, the components of the second-rank tensor $\boldsymbol{\alpha}_{\boldsymbol{t}}^{h}$ in the sample reference frame on a spatial grid aligned with the sample reference frame for the local state indexed by h would be represented as an array $\alpha[i,j]^{SF}[\boldsymbol{t}]^{SF}[h](\varphi_1, \Phi, \varphi_2, \theta)$. Square brackets and round brackets are used respectively for indices and the continuous variables needed to describe this tensor; the superscript identifies explicitly the associated reference frame. It is also important to mention that the components of this tensor are expected to be dependent on continuous variables $(\varphi_1, \Phi, \varphi_2, \theta)$.

This work first calibrated the values of the array $\alpha[i,j]^{PF}[\boldsymbol{t}]^{PF}[h](\theta)$ using previously demonstrated protocols in the MKS framework [43, 44, 49]. Subsequently, a computational strategy was defined that enable the efficient calculation of the $\alpha[i,j]^{SF}[\boldsymbol{t}]^{SF}[h](\varphi_1, \Phi, \varphi_2, \theta)$ array required for the actual implementation of the MKS framework in multiscale simulations. This array is needed because the material microstructure and the imposed stretching tensor are usually defined in the sample reference frame. It is important to recognize that the developed computational strategy involves only a suitable coordinate transformation of the influence kernel without any rotation of the given microstructure. The steps involved in the transformation of the influence kernel from the principal frame of the stretching tensor to the sample reference frame are schematically depicted in Figure 3.

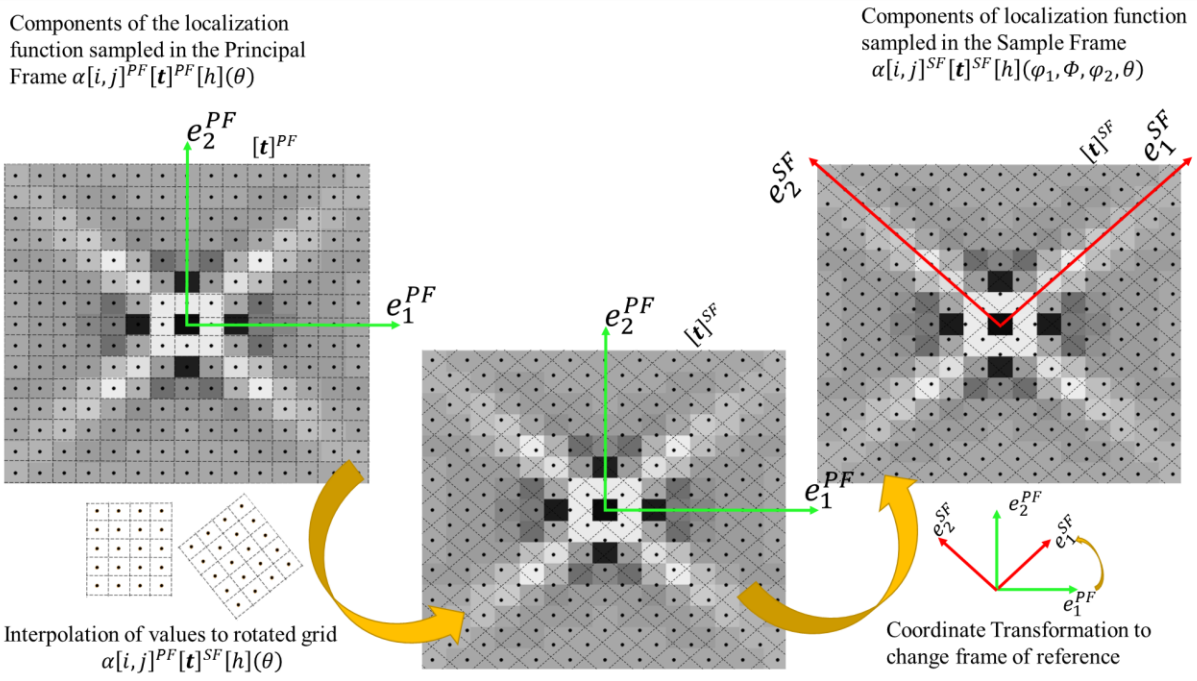

Figure 3: Schematic of the Transformation of Discrete Values of the Localization Function Sampled in the Principal Frame to the Sample Reference Frame.

Figure 3 shows 2D slices of the different spatial grids on which the continuous localization function ($\boldsymbol{\alpha}_{\boldsymbol{t}}^{h}(\varphi_1,\Phi,\varphi_2,\theta)$) can be discretized (sampled) depending on the desired frame of reference. As it can be seen one needs to change both the spatial grid on which the function is sampled as well as the orientation of the reference axes in order to recover the values of the function on a different reference frame. This is depicted as a two-step process in Figure 3. The first step obtains the value of the kernel function at the spatial grid associated with the new frame of reference using a suitable interpolation scheme. The second step transforms the orientation of the reference frame using a standard coordinate transformation law for second-rank tensors. More specifically, the first step requires the use of two different spatial grids denoted in Figure 3 as $[\boldsymbol{t}]^{PF}$ and $[\boldsymbol{t}]^{SF}$. The spatial locations on these two grids are in fact directly related by the set of Euler angles ($\varphi_1, \Phi,\ \varphi_2$) that describe the relationship between the two reference frames (note that

there is only a rotation between these two frames without any translation). Trigonometric interpolation is leveraged for re-sampling the function on the new spatial grid. As a result, the values of the function on the new spatial grid are calculated with the following trigonometric interpolation scheme:

$$\alpha[i,j]^{PF}[x,y,z]^{SF}[h](\theta) = \frac{1}{N_x}\frac{1}{N_y}\frac{1}{N_z}\frac{1}{N_\theta}\sum_{r=\frac{-N_x}{2}+1}^{\frac{N_x}{2}}\sum_{s=\frac{-N_y}{2}+1}^{\frac{N_y}{2}}\sum_{t=\frac{-N_z}{2}+1}^{\frac{N_z}{2}}\sum_{q=\frac{-N_\theta}{2}+1}^{\frac{N_\theta}{2}}\beta[i,j]^{PF}[r\ s\ t]^{PF}[h]\,[q]\,e^{\frac{2\pi irx}{L_x}}e^{\frac{2\pi isy}{L_y}}e^{\frac{2\pi itz}{L_z}}e^{\frac{2\pi iq\theta}{L_\theta}} \quad (4.6)$$

The coordinate transformation involved in the second step is described as follows (summation implied on repeated indices):

$$\alpha[k,l]^{SF}[\boldsymbol{t}]^{SF}[h](\varphi_1,\Phi,\varphi_2,\theta) = Q[k,i](\varphi_1,\Phi,\varphi_2)Q[l,j](\varphi_1,\Phi,\varphi_2)\alpha[i,j]^{PF}[\boldsymbol{t}]^{SF}[h](\theta) \quad (4.7)$$

A DFT representation of the $\alpha[i,j]^{PF}[\boldsymbol{t}]^{PF}[h](\theta)$ array is needed in order to be able to leverage the trigonometric scheme denoted in Eq. (4.6). The DFT representation was obtained by sampling the $\alpha[i,j]^{PF}[\boldsymbol{t}]^{PF}[h](\theta)$ array on a regular grid in the periodic domain of θ. The definition of θ in Eq. (4.3) identifies a periodic domain of [0, 120) degrees, with a mirror symmetry at 60 degrees [76-78]. This means that mirror symmetry can be leveraged to populate the complete periodic domain required to procure the DFTs representations. As a result, it is only necessary to generate the data in the θ = [0, 60) domain. In this work, it was decided to sample the array every one degree in the range identified above. Following the protocols described in previous work, the values of the $\alpha[i,j]^{PF}[\boldsymbol{t}]^{PF}[h](\theta)$ array were calibrated to the numerical results of two finite element simulations of "delta" microstructures [43, 44, 49] subjected to the periodic boundary conditions corresponding to each selected value of θ. A delta microstructure is defined as a microstructure in which an element of one phase is surrounded fully by the elements of the other phase [43, 49].

The calibration of the values of the array of interest are procured by linear regression (i.e., minimizing the sum of squared error) on Eq. (4.5) in the DFT space. Periodic boundary conditions are imposed through the displacement degrees of freedom on the boundary nodes. These boundary conditions are specifically well suited for the DFT operators used in the linear regression, and are expressed as follows:

$$u_3^{3+} - u_3^{3-} = \langle \varepsilon_{33} \rangle L, \qquad u_2^{2+} - u_2^{2-} = \langle \varepsilon_{22} \rangle L, \qquad u_1^{1+} - u_1^{1-} = \langle \varepsilon_{11} \rangle L$$

$$u_1^{3+} = u_1^{3-},\ u_1^{2+} = u_2^{2-},\ u_3^{1+} = u_3^{1-},\ u_3^{2+} = u_3^{2-}, \qquad u_2^{1+} = u_2^{1-}, \tag{4.8}$$

$$u_2^{3+} = u_2^{3-}, \qquad u_1^{C} = u_2^{C} = u_3^{C} = 0$$

where u_i denotes the i^{th} component of the displacement vector, $\langle \varepsilon_{ii} \rangle$ (no summation implied on the repeated indices) are the diagonal components of the macroscopic strain tensor, L represents the length of the cuboidal microstructure volume, and the superscript $n+$ or $n-$ identifies the set of nodes on the surface whose normal points in the positive n direction or the negative n direction, respectively. The superscript C in Eq. (4.6) denotes the corner node located at the (0, 0, 0) coordinate.

All the finite element simulations performed in this study were executed using finite element commercial software ABAQUS [83]. Each simulation was performed on a 21x21x21 finite element mesh of a three-dimensional cuboid, using continuum elements (C3D8) [83]. In prior work [49], it was observed that this size was sufficient to capture the details of the localization kernel for medium-contrast composites. A high elastic modulus of 1000 GPa was assigned to both phases. This was done to minimize the elastic strains and their influence on the plastic localization kernel extracted in this work. A contrast ratio of 1.5 between the yield strengths of the constituent phases was employed in this study, with the yield strength for the soft phase assigned as 200 MPa.

Each simulation (on each cuboidal microstructure volume) was deformed to a total strain of 0.1. It is important to mention that the imposition of perfectly-plastic constitutive relations caused the appearance of non-physical strain rate fields in the form of bands. Interestingly, these bands were most noticeable in the simulations corresponding to θ=30^o, which corresponds to overall (effective) plane strain conditions on the microstructure volume. After numerous trials (with different mesh densities, boundary conditions) it was ascertained that these were indeed caused by the perfectly plastic constitutive description. This hurdle was circumvented by adding a small amount of hardening in the constitutive responses of the constituent phases. A 15% increase in hardening over 8% plastic strain was imposed to avoid the non-physical strain rate fields (i.e., bands), while not significantly changing the contrast ratio of the yield strengths of the phases.

In total, 120 simulations (two delta microstructures subjected to periodic boundary conditions corresponding to every one degree value for θ = [0, 60)) were performed to produce the dataset needed to calibrate $\alpha[i,j]^{PF}[\boldsymbol{t}]^{PF}[h][\theta]$. The finite element computed plastic strain rate field (one averaged value for each spatial cell) for each delta microstructure was used to perform the regression analyses and extract the values of the plastic localization tensor of interest (this regression takes place in DFT space). Notice that these calculations are performed for discrete values of θ (every one degree). Therefore, performing this calibration step successfully results in establishment of $\alpha\ [i,j]^{PF}[\boldsymbol{t}]^{PF}[h][\theta]$. The square brackets on θ indicate that this array is essentially a uniform sampling of $\alpha[i,j]^{PF}[\boldsymbol{t}]^{PF}[h](\theta)$. The values of the $\alpha[i,j]^{SF}[\boldsymbol{t}]^{SF}[h](\varphi_1,\Phi,\varphi_2,\theta)$ array are then procured by casting the localization linkages in the DFT-space and using the computational strategy schematically depicted in Figure 3.

4.3 Validation of the Spectral Database of Kernels Calibrated in the Principal Frame

The critical validation of the computational strategies developed to leverage a discrete, finite set of localization kernels in principal frame to localize any arbitrary strain-rate tensor applied to the RVE at the macro-scale was performed systematically.

4.3.1 Validation of the Microstructure Independence of the Spectral Database of Calibrated Localization Kernels

The first validation consists in demonstrating that the calibrated localization kernels are independent of the microstructure itself. Following prior MKS implementations [43, 45, 48, 49], random microstructures where each spatial cell is randomly assigned one of the two local states (see Figure 4). These microstructures are not only very different from the ones used in the calibration of the kernels (i.e., delta microstructures), but also provide highly complex heterogeneous local fields and therefore serve as challenging validation case studies for our purpose.

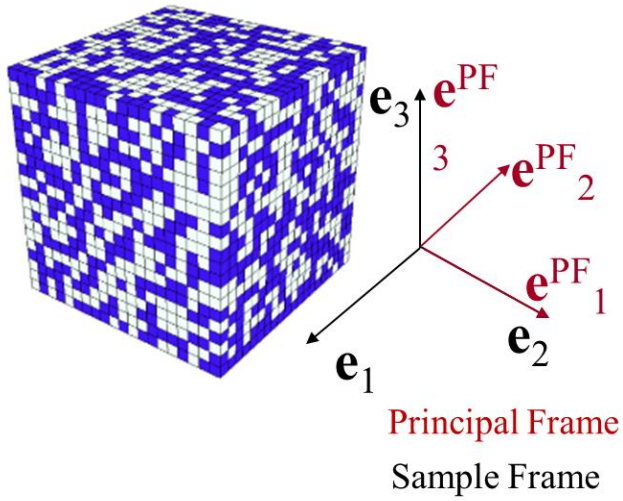

Figure 4: Example of a Random Microstructure Used as a Validation Microstructure.

The following macro scale strain rate was imposed to the generated random microstructure:

$$\langle D[i,j]\rangle^{SF} = \begin{bmatrix} -.56 & 0 & 0 \\ 0 & -.24 & 0 \\ 0 & 0 & .8 \end{bmatrix} \tag{4.9}$$

Although the applied $\langle \boldsymbol{D} \rangle$ is already in a principal frame, it is important to recognize that the sample frame corresponds to only one of the six possible principal frames that could be defined by choosing to align different sample axes with the three different principal axes. Indeed, the six possible principal frames produce the six different values of theta in range [0, 360). In this validation study the selected value of theta for the $\langle \boldsymbol{D} \rangle$ prescribed in Eq. (4.9) corresponds to $\theta = 46.5^{\circ}$. The corresponding Q_{ij} (defined in Eq. (4.4)) is presented below:

$$Q[i,j] = \begin{bmatrix} 0 & 0 & -1 \\ 0 & 1 & 0 \\ 1 & 0 & 0 \end{bmatrix} \tag{4.10}$$

Note also that this value of θ was not sampled in the calibration. Therefore, this case study represents a true validation.

A finite element simulation imposing the $\langle \boldsymbol{D} \rangle$ defined on Eq. (4.9) on the selected microstructure (Figure 4) was performed to obtain numerically the localized values of the plastic strain rate tensor in each spatial bin. The local values of the plastic strain rate tensor were also computed separately using the database developed in the previous section and following the approach described schematically in Figure 3. These results are compared in Figure 5.

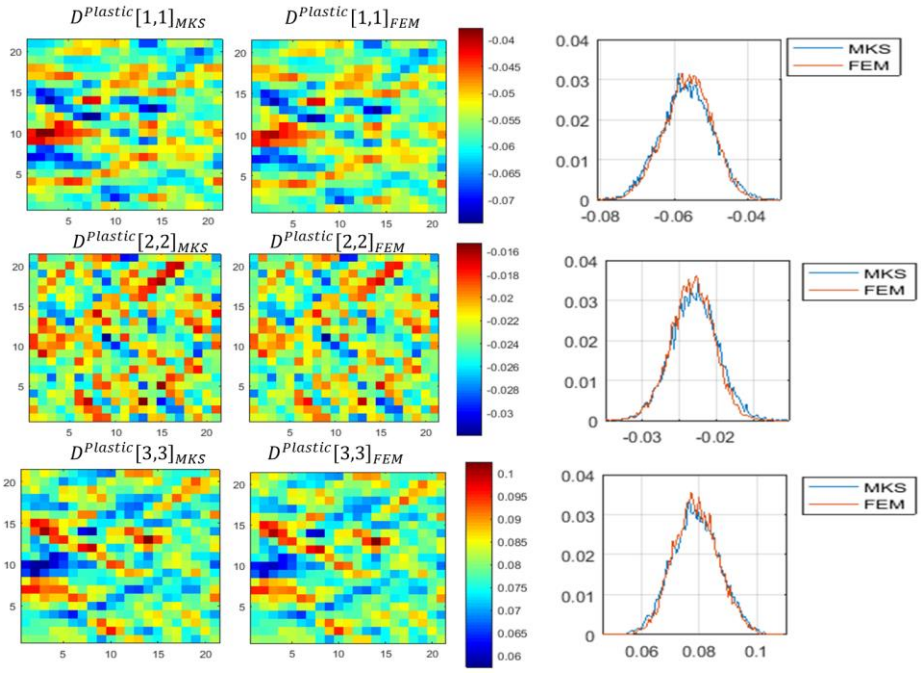

Figure 5: Comparison between the Results Obtained with the Spectral Database of Localization Kernels and those Obtained from the FE Simulation For the microstructure shown in Figure 4 subjected to the Stretching Tensor Described by Eq. (4.9).

The first two columns of Figure 5 compare the fields of the orthogonal components of the plastic strain rate tensor obtained by using the calibrated localization kernels (i.e., the MKS method) as well as the response fields obtained using the FE simulation on a mid-section of the microstructure volume. It can be clearly seen that there is excellent agreement between the results obtained by the extended MKS protocols developed in this work and the FE results. Similar results were also obtained for the off-diagonal components of the strain rate fields (not shown in Figure 5). The percentage error in the MKS predictions can be quantified for each spatial cell in the microstructure volume using the following error definition:

$$Err[i,j][\boldsymbol{s}]\% = \frac{\left|D^{Plastic}[i,j][\boldsymbol{s}]_{FEM} - D^{Plastic}[i,j][\boldsymbol{s}]_{MKS}\right|}{|\langle \boldsymbol{D} \rangle|} \times 100 \qquad (4.11)$$

where $D^{Plastic}[i,j][\boldsymbol{s}]_{FEM}$ denotes the value of the $[i,j]$ component of the plastic strain rate tensor obtained from the FEM simulation for bin $\boldsymbol{s}$, and $D^{Plastic}[i,j][\boldsymbol{s}]_{MKS}$ corresponds to the value predicted by the MKS approach. The mean value of this error for each of the six components of the plastic strain rate tensor is shown in Table 1.

Table 1: Mean Error (%) between the FEM and the MKS predicted values.

Strain Rate Tensor Component	Error (%)
D11	.83
D22	.69
D33	.60
D12	.58
D13	.73
D23	.58

Table 1 shows that the mean error in the MKS predictions is less than 1% for all the six components of the tensor. The accuracy obtained here is consistent with those obtained in prior applications of the MKS approach (cf. [43, 45, 48, 49]). The last column of Figure 5 compares the frequency histograms for the orthogonal components of the plastic strain rate tensor predicted for the selected microstructure with both methods. It can be seen that there is an excellent agreement between the histograms of the local plastic strain rate components obtained by both methods. The MKS predictions for the validation microstructure were produced with significant computational savings. The FE simulation for the new microstructure took 17 minutes on a single 2.4 GHz AMD processor node in the Georgia Tech super computer cluster, while the MKS predictions were obtained in only 2.4 seconds on the same resource. This validation example clearly demonstrates that the calibrated MKS localization kernels are independent of the

microstructure and attests to the accuracy and computational efficiency of trigonometric interpolation scheme previously outlined.

4.3.2 Validation of the Length-scale Independence of the Spectral Database of Calibrated Localization Kernels

The second validation shows the extensibility of the calibrated spectral database of localization kernels for RVEs of different sizes and demonstrates that the computational savings obtained with the MKS framework are independent of the RVE size. For this validation, a new random microstructure was created on a 43X43X43 spatial grid and a finite element simulation was performed with the macroscopic strain rate tensor in Eq. (4.9).

Following the strategies performed in previous MKS implementations [44, 45, 48, 80, 84], the size of the localization kernels contained in the calibrated spectral database (recall that the MKS kernels obtained in section are defined on a 21X21X21 spatial grid) are extended using a resampling strategy called spectral interpolation, which corresponds to simply padding the calibrated kernels with zeros. As a result, by leveraging spectral interpolation the MKS calibrated spectral database is able to obtain a prediction of the local values for the new extended RVE size. The MKS predictions are compared to the FE obtained values in Figure 6.

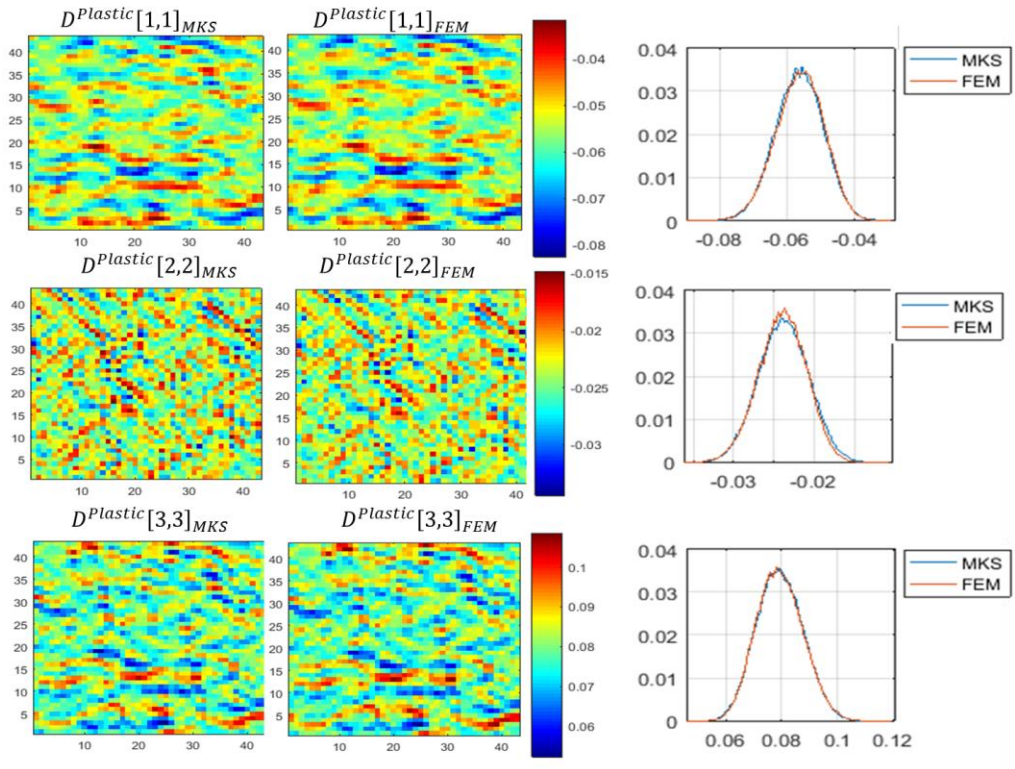

Figure 6: Comparison Between the Results Obtained using the Calibrated Spectral Database of Localization Kernels and the Results of the FE Simulation for a Microstructure Discretized on a 43x43x43 Grid.

From Figure 6 it can be clearly seen that the calibrated localization kernels contained in the previously established spectral database provide remarkably accurate predictions for the larger RVEs without the need to recalibrate them. The mean errors (obtained using Eq. (4.11)) for this validation study are summarized in Table 2 and are less than 1.2%. The slight increase in error from the earlier validation case study (see Table 1) is attributed to the spectral interpolation employed in resampling the calibrated kernels on a finer spatial grid. However, this small increase is quite acceptable in most practical applications. It should be noted that the computational savings obtained by employing the MKS framework on the larger RVE are even more significant. The FEM analysis required 15 hours (54,000 seconds) on a single 2.4 GHz AMD processor node in the Georgia Tech super computer cluster, while the MKS predictions were obtained in 2.4 seconds on

the same resource. This case study demonstrates the versatility of the MKS kernels for a broad range of microstructures and RVE sizes. It is also important to highlight that the computational efficiency of the MKS framework is much more noticeable when the RVE size is increased.

Table 2: Mean Error (%) between the FEM and the MKS predicted values for a 43x43x43 random microstructure subjected to boundary conditions expressed in Eq. (13).

Strain Rate Tensor Component	Error (%)
D11	1.1
D22	.42
D33	1.1
D12	.66
D13	.94
D23	.64

4.3.3 Validation of the Frame Independence of the Spectral Database of Calibrated Localization Kernels

The last validation consisted in demonstrating the applicability of the calibrated spectral database for localizing the response of an arbitrary strain rate tensor imposed at the macroscale. As a critical validation, the local values will be predicted for a case in which the computational strategy that obtains the localization kernels for any arbitrary sample frame (cf. Figure 3) is most likely to fail. This case corresponds to a 45 degree rotation of the spatial grid in all three angles because the new grid points are most distinctly away from the original grid points before rotation. As a result, this case study will localize the response for a strain rate macroscopically imposed on a sample frame corresponding to $\varphi_1 = 45^\circ, \Phi = 45^\circ, \varphi_2 = 45^\circ$. The predictions for the local values using the calibrated spectral database are readily obtained with the developed computational

strategy. Ironically, obtaining the corresponding FE results is not a simple matter because it was observed that when periodic boundary conditions corresponding to a macroscale stretching tensor with off-diagonal components were applied to a finite amount of plastic strain (~0.1), the overall shape of the periodic domain changed significantly making it difficult to compare directly (voxel by voxel) the FE results with the MKS predictions. Note that the MKS kernels presented here only localize the strain rate tensor. One needs to adequately evolve the microstructure to be able to apply these kernels to simulate plastic deformation over an imposed finite strain on the microstructure; this is yet an unsolved problem (cf. [85]). As a result, it was not possible to conduct a direct voxel to voxel comparison between MKS predictions and FE predictions in this final validation case study. Instead, the performed validation focused on comparing the frequency histograms of the microscale stretching tensor components between the FE and the MKS predictions.

The first step consisted in a macroscale strain rate tensor expressed in the sample and principal frames as follows:

$$\langle D[i,j]\rangle^{SF} = \begin{bmatrix} -0.028 & -.022 & -.006 \\ -.022 & .043 & -.056 \\ -.006 & -.056 & -.015 \end{bmatrix} \qquad \langle D[i,j]\rangle^{PF} = \begin{bmatrix} 0.079 & 0 & 0 \\ 0 & -0.21 & 0 \\ 0 & 0 & 0.06 \end{bmatrix} \quad (4.12)$$

The Euler angles that define the transformation matrix between these two frames are $\varphi_1 = 45^{\circ}, \Phi = 45^{\circ}, \varphi_2 = 45^{\circ}$. As stated earlier, the prediction of the local values caused by the tensor defined in Eq. (4.12) using the MKS method are obtained in a straightforward manner by simply following the computational strategy defined in 4.2 and schematically shown in Figure 3. In this case study the macroscopic strain rate tensor is imposed on a random microstructure (assumed to be close to a perfectly disordered microstructure) gridded along the sample frame (indexed with

the $m[\boldsymbol{s}]^{SF}[h]$ array). This random microstructure was generated by randomly placing different phases on a 43x43x43 voxel grid to attain a volume fraction of 59%.

However, the FE simulation was performed on an equivalent microstructure gridded along the principal frame (i.e., $m[\boldsymbol{s}]^{PF}[h]$) in order to correctly impose the periodic boundary conditions associated with the defined macroscopic stretching tensor. It is important to recognize that given the discretized nature of the RVEs employed in this study, it was impossible to create an exactly equivalent microstructure in the gridded along principal frame, given the microstructure in the sample frame. However, it was relatively easy to produce a statistically equivalent microstructure by simply defining a new random microstructure gridded along the principal frame with the same volume fraction. The equivalence between the two defined structures can be ascertained from their 2-point statistics maps [58, 71] shown in Figure 7.

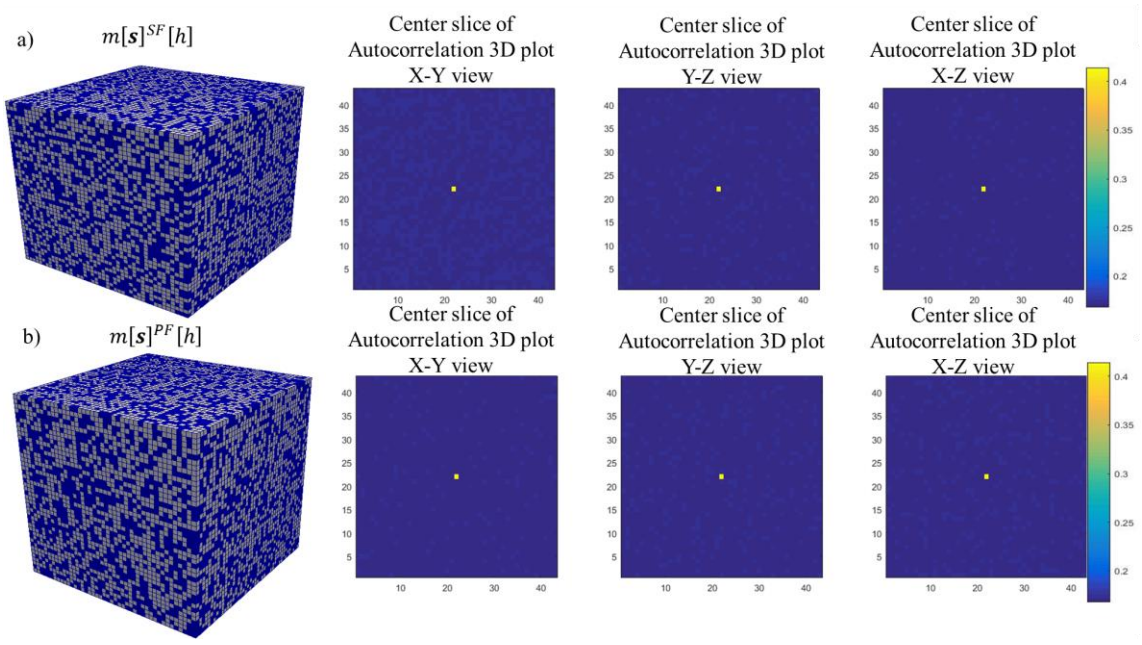

Figure 7: a) Random 43x43x43 Microstructure Defined in the Sample Frame along with Three Center Sections of the 3-D Autocorrelation Plot. b) Another 43x43x43 Statistically Equivalent Microstructure Defined in the Principal Frame with the Same Volume Fraction as the One Shown in (a) along with Three Center Sections of the 3-D Autocorrelation Plot.

The 2-point statistics maps shown in Figure 7 shows that the two defined RVEs are fairly close to being perfectly disordered. As a result, it can be concluded that the two defined RVEs are statistically equivalent microstructures. Furthermore, since the perfectly disordered structures do not exhibit any directionality, the rotation from the sample frame to the principal frame does not change the statistics of the microstructure. Once the FE analysis completed on the microstructure gridded along the principal frame, the local plastic stretching tensor components in each voxel were converted to the sample frame to facilitate comparison with the MKS predictions. The MKS and FE predictions for this case study are compared as frequency histograms in Figure 8.

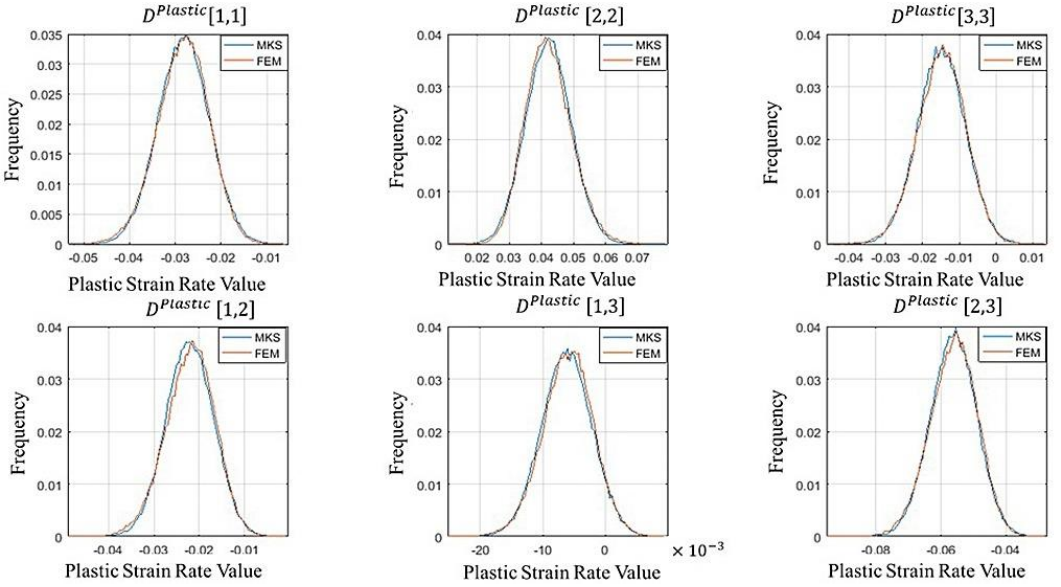

Figure 8: Comparison of the Frequency Distributions of the Local Values of the Stretching Tensor Components in the Sample Frame Obtained with the MKS Approach and the Corresponding FE Simulation.

As it can be clearly seen from Figure 8 the frequency distributions obtained with both methods show excellent agreement. Thus, demonstrating the applicability of the calibrated spectral database of localization kernels to localize the response of an arbitrary strain rate tensor imposed at the macroscale. It is also important to highlight the computational savings associated with

implementing the MKS framework. The FEM analysis required 15 hours (54,000 seconds) on a one 2.4 GHz AMD processor node in the Georgia Tech super computer cluster, while the MKS predictions were obtained in 2.4 seconds on the same resource.

4.4 Summary and Conclusions

The case studies performed in this chapter demonstrate that the MKS localization framework has been successfully extended and is now capable of accurately predicting, and in a computationally efficient manner, the local plastic response caused by imposing any arbitrary plastic strain rate tensor at the macroscale for an RVE of a material made of two isotropic phases. Therefore, eliminating one the main impediments in advancing the adoption of the MKS approach as a practical scale-bridging framework in fully-coupled multiscale modeling efforts.

CHAPTER 5:

Localization Models for the Plastic Response of Polycrystalline Materials Using the Material Knowledge Systems Framework

This chapter integrates all the previously developed enhancements that have enabled the MKS localization framework undertake the localization problem for complex material structures and non-linear phenomena and defines suitable extensions in order to enable this framework to predict the local plastic response in polycrystalline microstructures caused by any arbitrary periodic boundary condition imposed at the macroscale. As a result, this chapter reports the first successful application of the MKS framework for modeling the localization of the plastic response in polycrystalline microstructures. This chapter provides the details of the implementation for single-phase, fcc, cubic polycrystalline materials. It is important to acknowledge that the choice of the crystalline structure and of sample and crystal symmetry is arbitrary. However, it is more important to establish that the protocols described in this chapter are agnostic to these parameters and as such can be repeated for any other crystal structures and symmetries of interest.

5.1 Derivation of the MKS Localization Framework for the Plastic Response of Polycrystalline Materials

The general localization relationship denoted in Eq. (3.5) is suitable for materials whose internal structure can be adequately represented by two or more thermodynamically distinct phases (enumerated by a discrete variable h). However, this expression is not ideal/adequate for the polycrystalline structures of interest in this chapter since their internal structure is significantly more complex. Section 2.2.2 shows that the adequate microstructure function (i.e., the mathematical function used to represent the internal structure of the material) for single-phase polycrystalline structures is adequately characterized by the spatially resolved ODF ($f_s(g)dg$). Incorporating the

new microstructure function ($f_s(g)dg$) into Eq. (3.5) requires for one to replace the summations over $h \in H$ with suitable integrals over $g \in FZ$, where FZ denotes the fundamental zone in the orientation space [7] representing the complete set of all physically distinct lattice orientations (i.e., after accounting for all relevant crystal symmetries). For the same reason, the localization kernels also need to be expressed as functions of the lattice orientation, g. These changes produce the relevant MKS formulation for the localization relationship applicable to single-phase polycrystalline structures as follows:

$$\boldsymbol{p_s} = \left(\sum_{\boldsymbol{t}}^{\boldsymbol{S}} \int_{FZ} \boldsymbol{\alpha_t}(g) f_{\boldsymbol{s+t}}(g) dg + \sum_{\boldsymbol{t}}^{\boldsymbol{S}} \sum_{\boldsymbol{t'}}^{\boldsymbol{S'}} \int_{FZ} \int_{FZ} \boldsymbol{\alpha_{tt'}}(g, g')\, f_{\boldsymbol{s+t}}(g) f_{\boldsymbol{s+t+t'}}(g, g') dg' dg + \ \ldots \right) \langle \boldsymbol{p} \rangle \tag{5.1}$$

where the dependence on the orientation of the crystal lattice is clearly noted on both the microstructure function and the localization kernels. It should be noted that Eq. (5.1) (limited to first-order kernels) has been successfully applied to obtain a high fidelity localization model for elastic deformations in polycrystalline microstructures [45].

For the application to plastic deformations on polycrystalline RVEs one needs to apply this equation on a variable that characterizes the rate of deformation that the polycrystalline RVE is experiencing. The plastic component of the velocity gradient ($\boldsymbol{L}^p$) is the logical choice since it is related to the shearing rate experienced by the slip systems on the polycrystalline RVE (assuming that the plastic deformation in the polycrystal is caused solely by the motion of dislocations along the slip systems) by the following relationship [13-18]:

$$\boldsymbol{L}^p = \sum_{\beta} \dot{\gamma}^{(\beta)} \boldsymbol{m}_t^{\beta} \otimes \boldsymbol{n}_t^{\beta} \tag{5.2}$$

where $\dot{\gamma}^{(\beta)}$ is the shearing rate, $\boldsymbol{m}_t^{\beta}$ is the slip direction at the current time t and $\boldsymbol{n}_t^{\beta}$ is slip plane normal also at the current time t. It is important to notice that each of these quantities correspond to

a slip system β. The plastic component of the velocity gradient can be decomposed into a symmetric part that captures the rate of stretch on the polycrystal (typically denoted by $\boldsymbol{D}^p$) and an anti-symmetric that part captures the total rate of spin on the polycrystal.

Therefore, decomposing $\boldsymbol{L}^p$ into its symmetric and antisymmetric components and leveraging the previous implementation of the MKS localization framework to polycrystalline structures [45], as well as the previous implementation to plastic deformations in multiphase composites [43, 80], enables one to define the following localization relationship of the plastic response for single-phase polycrystalline materials:

$$\boldsymbol{L}_{\boldsymbol{s}}^{p} = \left(\sum_{\boldsymbol{t}}^{\boldsymbol{S}} \int_{FZ} \boldsymbol{\alpha}_{\boldsymbol{t}}(g, \boldsymbol{d}^p) f_{\boldsymbol{s+t}}(g) dg + \sum_{\boldsymbol{t}}^{\boldsymbol{S}} \sum_{\boldsymbol{t'}}^{\boldsymbol{S'}} \int_{FZ} \int_{FZ} \boldsymbol{\alpha}_{\boldsymbol{tt'}}(g, g', \boldsymbol{d}^p) f_{\boldsymbol{s+t}}(g) f_{\boldsymbol{s+t+t'}}(g') dg' dg \right) |\langle \boldsymbol{D}^p \rangle| + |\langle \boldsymbol{W} \rangle| \tag{5.3}$$

where $\boldsymbol{L}^p{}_{\boldsymbol{s}}$ denotes the value of the plastic component of the velocity gradient at voxel $\boldsymbol{s}$, $\frac{\langle \boldsymbol{D}^p \rangle}{|\langle \boldsymbol{D}^p \rangle|}$ denotes the direction (unit magnitude) of the macroscopically imposed symmetric and traceless plastic stretching tensor and $\langle \boldsymbol{W} \rangle$ denotes the macroscopically imposed spin tensor. Notice that the imposed spin rate needs not to be localized because every point in the RVE experiences the same spin rate as the one that is being macroscopically imposed. Also notice that the localization relationship defined in Eq. (5.3) shows that the calibrated localization kernels are not only dependent on the crystal lattice orientations (g) but also on the direction (unit magnitude) of the macroscopically imposed symmetric and traceless plastic stretching tensor denoted by $\boldsymbol{d}^p = \frac{\langle \boldsymbol{D}^p \rangle}{|\langle \boldsymbol{D}^p \rangle|}$.

Looking at the kernel $\boldsymbol{\alpha}_{\boldsymbol{t}}(g, \boldsymbol{d}^p)$ in the first term in Eq. (5.3), it becomes clear that this kernel is defined over a total of seven independent variables (three variables defining the crystal

lattice orientation g and four variables defining the traceless unit tensor $\boldsymbol{d}^p$). These seven variables are in addition to the variable $\boldsymbol{t}$, which is a three-dimensional vector indexing the set of discretized vectors used to represent the difference between any two spatial points in the RVE. In prior work on multiphase composites [80], the first order kernel was similarly defined over four variables (since the local state did not need a prescription of g), and it was shown that one can effectively reduce the number of independent variables to one by choosing to establish the kernel in the principal frame of $\boldsymbol{d}^p$. In this work, we employ the same strategy to reduce the number of independent variables in the kernel $\boldsymbol{\alpha_t}(g, \boldsymbol{d}^p)$ from seven to four. In other words, we will choose to express the second-rank tensor $\boldsymbol{\alpha_t}$ in the principal frame of $\boldsymbol{d}^p$, where the traceless unit tensor $\boldsymbol{d}^p$ can be expressed using a single variable θ [76]. As a result, it is also needed to re-define the crystal lattice orientation g as the set of Bunge-Euler angles that rotate the principal frame of $\boldsymbol{d}^p$ to the crystal frame. These definitions are clarified in Figure 9, where the three different reference frames of interest are depicted. These include a sample reference frame, a crystal reference frame, and a principal reference frame for $\boldsymbol{d}^p$. The transformation matrix from the sample reference frame to the principal frame of $\boldsymbol{d}^p$ is denoted by $[Q]$, and is obtained by solving for the eigen vectors of $\boldsymbol{d}^p$. Note that all components of $\boldsymbol{d}^p$ can be expressed as functions of a single independent variable θ. The transformation from the principal frame of $\boldsymbol{d}^p$ to the crystal reference frame is denoted by the set of Bunge-Euler angles, $g = ({\varphi_1}^c, \Phi^c, {\varphi_2}^c)$. Taking advantage of the simple structure of $\boldsymbol{d}^p$ in its principal frame, one can express the components of the kernel in the same principal frame as $\boldsymbol{\alpha_t}[i,j]^{PF}(g,\theta)$. In this notation, the indices in the square brackets enumerate the tensorial components, and the superscript on the square brackets indicate the frame in which they are expressed. The variables g and θ are shown in curved brackets to indicate that they are treated as continuous variables in the functional dependence expressed.

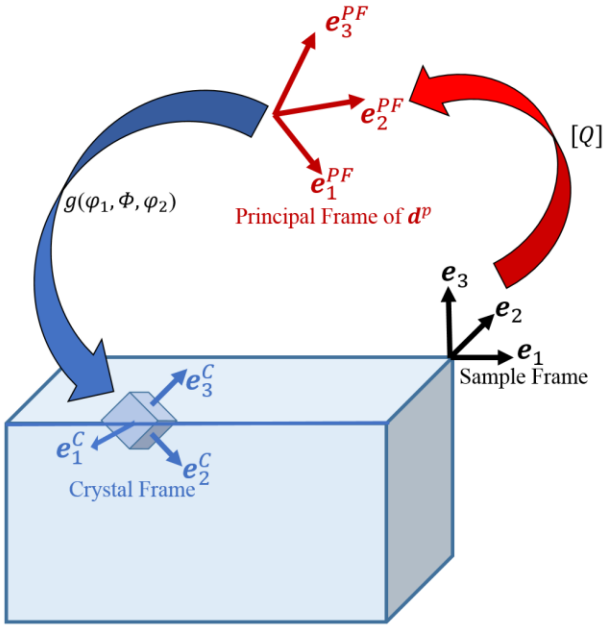

Figure 9: Clarification of the different reference frames and the coordinate transformation matrices used in this work.

The orientation dependence of the $\boldsymbol{\alpha_t}[i,j]^{PF}(g,\theta)$ can be captured with a compact set of coefficients by using generalized spherical harmonics (GSH) [51] as a Fourier basis (cf. [7, 41, 45, 51]) as

$$\boldsymbol{\alpha_t}[i,j]^{PF}(g,\theta) = \sum_{\mu,n,l} \boldsymbol{A_{lt}^{\mu n}}[i,j]^{PF}(\theta)\, \dot{T}_l^{\mu n}(g) = \sum_{L} \boldsymbol{A_t^L}[i,j]^{PF}(\theta)\, \dot{T}^L(g) \tag{5.4}$$

where $\boldsymbol{A_t^L}[i,j]^{PF}(\theta)$ denote the GSH coefficients and L Lenumerates over all relevant and distinct combinations of (μ,n,l) in the symmetrized GSH basis functions $\dot{T}_l^{\mu n}(g)$ (these implicitly account for the crystal symmetry) [51]. The θ-dependence of kernel coefficients in Eq. (4) will be captured using DFT (discrete Fourier transform) representation, the same way we will also address the $\boldsymbol{t}$-dependence. The advantages of using DFTs for such representations has been demonstrated in prior

work on related problems [77, 78, 80]. Specifically, they allow for computationally efficient and accurate interpolations of the values of highly complex functions sampled on a uniform grid on any new point in the complete domain space. Adoption of this strategy entails representing the kernel coefficients in Eq. (4) as an array $\boldsymbol{A}^L[i,j]^{PF}[\boldsymbol{t}]^{PF}[\theta]$, where $[\boldsymbol{t}]^{PF}$ represents a uniform spatial grid aligned with the principal frame of $\boldsymbol{d}^p$ in the vector space and $[\theta]$ denotes a uniform grid in the θ-space, and performing DFTs on $[\boldsymbol{t}]^{PF}$ and $[\theta]$ using the FFT (fast Fourier transform) algorithms [52, 86]. Let $\boldsymbol{\mathcal{A}}_{\boldsymbol{t}}^L[i,j]^{PF}[\boldsymbol{k}]^{PF}[q]$ denote the DFTs obtained by this process. Note that in three dimensional space, $\boldsymbol{t}$ and $\boldsymbol{k}$ would comprise three integer indices, i.e., $\boldsymbol{t} = (t_1, t_2, t_3)$ and $\boldsymbol{t} = (k_1, k_2, k_3)$.

In the actual application of the MKS approach on a new microstructure with a new periodic boundary condition, one needs to transform the established $\boldsymbol{\mathcal{A}}_{\boldsymbol{t}}^L[i,j]^{PF}[\boldsymbol{k}]^{PF}[q]$ (in a one-time computational effort described in subsequent section; cf. [45, 80]) to the $\boldsymbol{A}^L[i,j]^{SF}[\boldsymbol{t}]^{SF}(\theta)$ needed for the specific application. In other words, we would need to recover the kernel coefficients on a spatial grid aligned with an arbitrarily specified sample reference frame and an arbitrarily specified value of θ for a general application of the MKS framework. Moreover, this recovery has to be accomplished in a computationally efficient manner. This can be accomplished in two steps. In the first step, one would use a well-established trigonometric interpolation strategy (commonly used in DFT representations; cf. [87]) to recover $\boldsymbol{A}^L[i,j]^{PF}[\boldsymbol{t}]^{SF}(\theta)$. In the second step, these kernel coefficients are transformed into the sample frame using the standard coordinate transformation laws for second-rank tensors (using the [Q] matrix identified in Figure 2; cf. [7, 41]). The transformed kernel coefficients are denoted as $\boldsymbol{A}^L[i,j]^{PF}[\boldsymbol{t}]^{SF}(\theta)$, and represent the GSH coefficients of the MKS kernel needed for the selected application.

It is important to acknowledge that the MKS localization framework presented above deals only with the localization of the imposed plastic velocity gradient at any instant in time. In order to apply the framework to finite strain levels, additional advances would be needed. These include (i) incorporation of elastic deformations to allow for a proper treatment of the elastic-plastic deformations in polycrystalline metals, and (ii) update of the microstructure after a specified time step with the imposed plastic velocity gradient. Both of these problems need further development and are beyond the scope of the present dissertation. As stated in the introduction of this chapter, in this dissertation the focus will exclusively be on the localization of the imposed plastic velocity gradient in fcc (face-centered cubic) polycrystalline microstructures that exhibit cubic-triclinic symmetry. It is important to acknowledge and that the choice of the crystalline structure and of the sample and crystal symmetry was arbitrary. However, it is more important to establish that the calibration protocol described in the subsequent section is agnostic to these parameters. Therefore, the described calibration protocol can be implemented for any other crystal structures and symmetries of interest.

5.2 Calibration of MKS Localization Kernels for the Plastic Response of Polycrystalline Materials

In this first application of the MKS localization framework to fcc polycrystalline microstructures, the attention is focused on the first-order kernel in the first term of the expansion in Eq. (5.3). With the introduction of the GSH as a Fourier basis for the functions defined on the orientation space and the other notation described in the previous section, Eq. (5.3) limited to the first term in the series expansion can be expressed in the principal frame of $\boldsymbol{d}^p$ as:

$$\boldsymbol{L}^{p}[\boldsymbol{s}]^{PF} = \left(\sum_{L} \boldsymbol{A}^{L}[i,j]^{PF}[\boldsymbol{t}]^{PF}(\theta)\, M^{L}[\boldsymbol{s}+\boldsymbol{t}]^{PF} \right) |\langle \boldsymbol{D}^{p} \rangle| + |\langle \boldsymbol{W} \rangle| \tag{5.5}$$

with $M^{L}[\boldsymbol{s}]^{PF}$ denoting the GSH coefficients of the spatially resolved orientation distribution function defined by

$$f[\boldsymbol{s}]^{PF}(g) = \sum_{\mu,n,l} M_{l}^{\mu n}[\boldsymbol{s}]^{PF}\, \dot{T}_{l}^{\mu n}(g) = \sum_{L} M^{L}[\boldsymbol{s}]^{PF}\, \dot{T}^{L}(g) \tag{5.6}$$

In deriving Eqs. (5.5) and (5.6) from Eq. (5.3) certain constants arise in the integration over the orientation space. However, these were absorbed into the kernel coefficients $\boldsymbol{A}^{L}[i,j]^{PF}[\boldsymbol{t}]^{PF}(\theta)$ to simplify the expression in Eq. (5.5), keeping in mind that the kernel coefficients in the MKS framework are calibrated to the results from FE simulations.

It is clear from Eq. (5.5) that the θ-dependence in $\boldsymbol{A}^{L}[i,j]^{PF}[\boldsymbol{t}]^{PF}(\theta)$ can be treated efficiently by considering one value of θ at a time. Because of our interest in using DFTs for effective interpolation in the θ-space, the values of θ were sampled on a uniform grid in the θ-space. In other words, the $\boldsymbol{A}^{L}[i,j]^{PF}[\boldsymbol{t}]^{PF}(\theta)$ is established through a suitable calibration with FE results on the θ-space of interest of $[0, 60)$, since it can then be expanded to $[0, 120)$ using a mirror symmetry at $\theta = 60$ degrees [76-78]. The θ-space $[0, 120)$ exhibits the periodicity needed for efficient DFT representations. In this work, the $[0, 60)$ is sampled every 10 degrees. Although it is desirable to employ a higher sampling, it should be noted that the computational cost of the calibration increases with higher sampling. Furthermore, in the MKS framework, it is always possible to add new data points in subsequent refinements of the localization kernels. For example, one can decide in the future to sample every 5 degrees and enhance the kernel coefficients (this will improve the interpolation in the θ-space). This is because the kernel coefficients at the

different θ values are stored separately from each other in the representation $\boldsymbol{A}^{L}[i,j]^{PF}[\boldsymbol{t}]^{PF}[\theta]$; the only requirement in the MKS framework is that the sampling is performed on a uniform grid to allow the use of FFT algorithms and DFT representations.

As already mentioned, the values of the $\boldsymbol{A}^{L}[i,j]^{PF}[\boldsymbol{t}]^{PF}(\theta)$ are calibrated to the results obtained from CPFEM simulations performed on synthetically generated microstructures (i.e., a calibration ensemble). The protocols for the calibration have been established in prior work [43-45, 80]; these are extended in this work for the application to the formulation of localization models for the plastic stretching tensor in polycrystalline microstructures. Broadly speaking, these protocols involve two main steps: (i) generation of a training dataset using CPFEM, and (ii) calibration of $\boldsymbol{A}^{L}[i,j]^{PF}[\boldsymbol{t}]^{PF}[\theta]$.

The generation of the training dataset requires generation of a diverse and large set of polycrystalline microstructures exhibiting a rich variety of microstructural features that might be encountered in the subsequent application of the MKS models to new microstructures. Ideally, one would cover a very large range of potential grain shape, size, orientation, and misorientation distributions in generating these synthetic microstructures. Clearly, the space of polycrystalline microstructures that could be explored is unimaginably large. Building on prior experience [45], this work focused on three classes of polycrystalline microstructures when generating the training dataset.

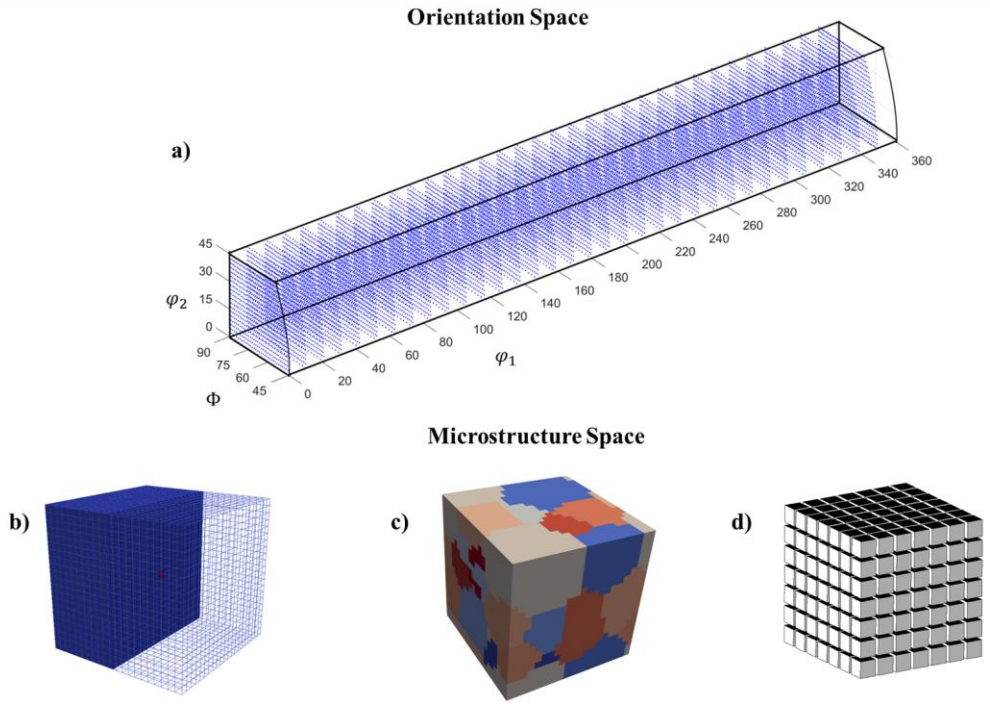

Figure 10: Calibration Ensemble Used to Train the Localization Kernel Coefficients in the Principal Frame of the Macroscopically Imposed Plastic Velocity Gradient.

Figure 10(a) shows 20,000 Bunge-Euler angles uniformly sampled from the fundamental zone of cubic lattice orientations. These Bunge-Euler angles were used to build the training dataset of the localization kernels. Figure 10(b)-(d) shows examples of the three different microstructure classes employed for generating the training dataset used in this dissertation. The example shown in Figure 10(b) is referred as a delta microstructure [43, 44, 49] and is generated by placing a cubic "grain" of a selected lattice orientation at the center of the RVE surrounded by cubic elements of a different selected lattice orientation. As mentioned earlier and demonstrated in prior work, delta microstructures are extremely efficient for the calibration of the first order MKS localization kernels because they capture accurately the impulse response [43, 44]. As a result, in principle, if one can systematically explore, in sets of two at a time, all possible combinations of the lattice orientations sampled from the fundamental zone of cubic lattice orientations (shown in Figure 10

(a)), this class of microstructures alone is adequate to calibrate the first-order MKS localization kernels to a high level of accuracy. However, this is not practical as the fundamental zone of the orientation space is quite large. Figure 10(c) depicts an example equi-axed microstructure generated using the Dream.3D software package [88]. Each equi-axed microstructure used in the training set was generated to contain approximately 25 grains, and the lattice orientations assigned to the grains were sampled randomly from the fundamental zone of the cubic orientation space (from the individual points shown inside the fundamental zone in Figure 10(a)). Figure 10(d) shows an example microstructure with cube "grains", whose lattice orientations were also assigned through random sampling of the fundamental zone of the cubic orientation space shown in Figure 10(a). Microstructures of the type depicted in Figure 10(d) exhibit rich heterogeneity in the variation of the plastic stretching tensor at the microscale and are effective in training the MKS localization models. It is important to note that the training dataset is being constructed to inform the MKS localization models (i.e., capture the complex interactions that occur at the microscale in the polycrystalline microstructures). Therefore, it is better to pick microstructures that exhibit complex microscale interactions for the training of the MKS localization kernels. A total of 9000 polycrystalline microstructures (3000 from each of the three classes described above) were generated for the training dataset.

Each training microstructure was then analyzed for each selected value of θ by imposing suitably defined periodic boundary conditions[80]. Since we explored six different values of θ, this meant executing 54000 CPFEM simulations. These simulations were performed using the commercial FE package ABAQUS [83], which allows the specification of the material constitutive laws through a user subroutine called UMAT. The UMAT used in this work employed the elastic-viscoelastic crystal plasticity theory (with a rate-sensitivity of 0.01) along with a computationally

efficient implicit time-integration scheme that was extensively validated in prior work for fcc metals [14, 89]. Size dependent effects [90, 91], which become of increasing importance when procuring the plastic response of a polycrystalline RVE with small number of grains [92], are not considered in this work. As a result, the crystal plasticity theory used to obtain the local values of the plastic response does not incorporate size-dependence effects since they complicate the behavior, and the calibration effort, because one needs more advanced crystal plasticity theories to obtain the plastic response (cf. [93] for a comparison of several size dependent crystal plasticity theories). Moreover, the incorporation of these effect needs also to define a microstructure function that incorporates the descriptors that drive/control these effects, such as back stress [93]. As it can be seen, the incorporation of these effects needs further development. Consequently, it will be addressed in future work and is not considered in the scope of this work.

Each FE model of the training microstructure employed a uniform mesh of 21x21x21 cubic continuum elements with eight nodes (C3D8) [83] (prior MKS implementations have demonstrated that this size of mesh is sufficient to calibrate the first-order localization kernels [44, 80]). High values of elastic moduli were assigned in all the FE simulations to limit the elastic strains to small numbers (~0.001), and slip hardening rates were set to zero. The volume and time averaged local plastic velocity gradient over the 0.01-0.02 range of the total imposed plastic strain was extracted from the FE simulation for each voxel (corresponding to an element in the FE model) and documented as $\boldsymbol{L}^p[\boldsymbol{s}]^{PF}$.

Looking at Eq. (5.5), it should be clear that each voxel of the FE training simulation provides one training data point, as $\boldsymbol{L}^p[\boldsymbol{s}]^{PF}$ serves as the target (output) and the details of the microstructural neighborhood (captured in $M^L[\boldsymbol{s}+\boldsymbol{t}]^{PF}$) serve as the inputs (features) for the calibration of the desired MKS localization kernels. Therefore, each FE simulation performed as

described earlier generates a set of 9261 (=21^3) training data points. The generation of the training set described above involved 54000 CPFEM simulations and as such incurred a substantial computational cost since each CPFEM simulation took approximately 90 minutes on a single 2.4 GHz AMD processor node in the Georgia Tech super computer cluster. However, the central benefit of the MKS framework is that subsequent evaluations of new microstructures (after the calibration process is completed) incur only modest computational cost.

In order to calibrate the $\boldsymbol{A}^{L}[i,j]^{PF}[\boldsymbol{t}]^{PF}[\theta]$ depicted in Eq. (5.5), we employ the DFT-based strategy demonstrated in prior MKS applications [44, 45, 48, 49, 80]. More specifically, it can be seen that the DFT representation of Eq. (5.5) allows calibration of significantly smaller subsets of the kernel coefficients (one value of θ at a time) dramatically reducing the computational cost of the calibration. Therefore, performing the liner regression for each sampled value of θ results in the establishment of the desired $\boldsymbol{A}^{L}[i,j]^{PF}[\boldsymbol{t}]^{PF}[\theta]$ array. This work calibrated the values of the localization kernels for five different truncation levels of GSH Fourier basis (i.e., five different values of the maximum value of L).

5.3 Validation of the calibrated MKS Localization Kernels for Polycrystal Plasticity

In this section it will be systematically demonstrated that one can leverage the DFT representation of the calibrated $\boldsymbol{A}^{L}[i,j]^{PF}[\boldsymbol{t}]^{SF}(\theta)$ kernels coefficients to localize any arbitrary macroscopically imposed plastic stretching tensor and that the computational savings obtained are independent of the RVE size.

The first validation case study consists in demonstrating that the calibrated localization kernels are capable of accurately localizing any arbitrary macroscopically imposed plastic velocity gradient. As in prior MKS implementations, a brand new ensemble of microstructures (i.e., a

validation ensemble) was defined. This new validation ensemble contains four new different microstructure types and sampled 3500 new (i.e., not contained in the original orientation calibration ensemble) Bunge-Euler angles from the FZ_C. As a result, the morphology (i.e., shape, size and spatial arrangement of the grains) as well as the crystal lattice orientations of the microstructures in validation ensemble are completely different from the microstructures comprised in the calibration ensemble. Figure 11 shows the validation ensemble used to demonstrate the evaluate the performance of the calibrated localization kernels.

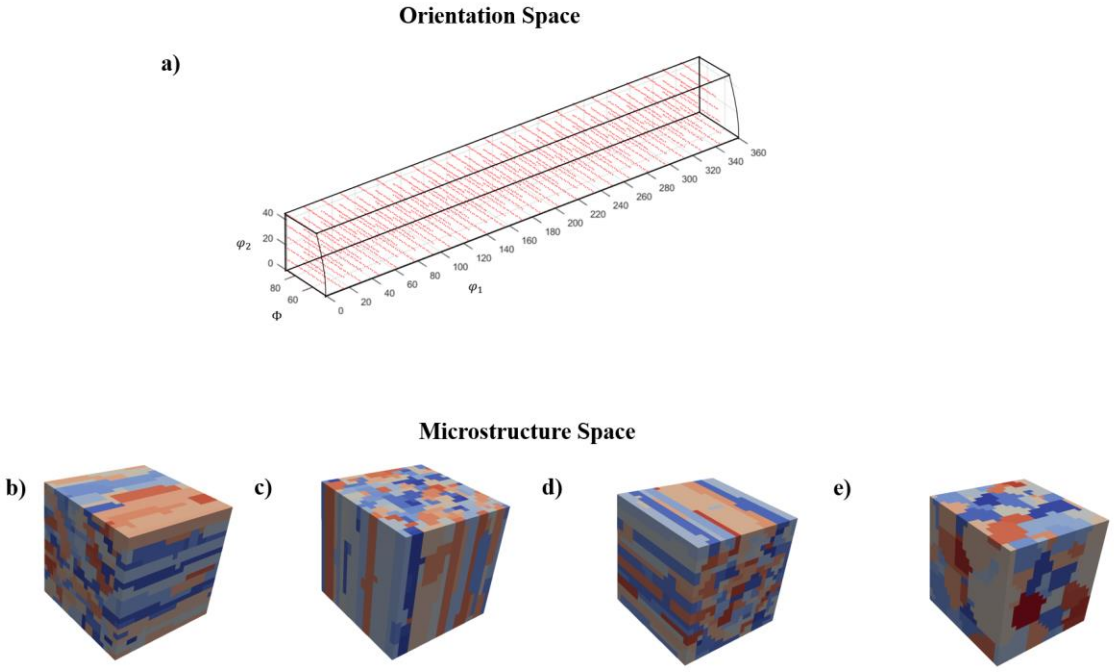

Figure 11: Ensemble Used to Validate the Calibrated Localization Kernels.

Figure 11a shows the 3500 new crystal lattice orientations (Bunge-Euler angles) sampled from the FZ_C. Figure 11b-e show the new different microstructure types comprised in the validation ensemble. Figure 11 b-d depict rolled microstructures with grains elongated along the X, Z and Y directions, respectively, with approximately 120 grains, 50 instantiations of these types

of microstructures are comprised in the validation ensemble. Figure 11e shows a new type of equiaxed microstructure that comprises approximately 120 grains (note that the equiaxed microstructure in the calibration ensemble had 25 grains) 50 instantiations of this new equiaxed microstructure type are comprised in the validation ensemble. As a result, the validation ensemble encompasses a total of 200 new microstructures.

Following the validation strategy defined in the last chapter a macroscopically imposed plastic stretching tensor not contained in the sampled θ-domain was defined and imposed to all the microstructures in the validation ensemble. The new macroscopic plastic velocity gradient tensor imposed to all the microstructures in the validation ensemble is the following:

$$\langle L^p[i,j]\rangle = \begin{bmatrix} .0111 & 0 & 0 \\ 0 & .0047 & 0 \\ 0 & 0 & -.0159 \end{bmatrix} \tag{5.7}$$

The macroscopic plastic velocity gradient denoted by Eq. (5.7) corresponds to imposing the following macroscopic stretching and spin rate:

$$\frac{\langle D^p[i,j]\rangle}{|\langle D^p[i,j]\rangle|} = \begin{bmatrix} .5568 & 0 & 0 \\ 0 & .2387 & 0 \\ 0 & 0 & -.7956 \end{bmatrix}$$

$$\text{where } |\langle D^p[i,j]\rangle| = .02 \tag{5.8}$$

$$\langle W[i,j]\rangle = \begin{bmatrix} 0 & 0 & 0 \\ 0 & 0 & 0 \\ 0 & 0 & 0 \end{bmatrix}$$

The macroscopic plastic stretching tensor defined by Eq. (5.8) corresponds to $\theta = 13^{\circ}$, a boundary condition not sampled when evaluating the $\boldsymbol{A}^L[i,j]^{PF}[\boldsymbol{t}]^{PF}[\theta]$ array. Consequently, this

new macroscopic plastic velocity gradient tensor needs to be localized using the trigonometric interpolation scheme outlined in the previous section (and developed in [80]). The local values caused by imposing the macroscopic plastic velocity gradient defined in Eq. (5.7) were obtained for each microstructure in the validation ensemble using the five different localization kernels calibrated in the last section (corresponding to the five different levels of truncation for the GSH Fourier basis) and also by performing a CPFEM simulation. The error difference between the MKS predicted values and the CPFEM values is defined as follows[50]:

$$Err[i,j]\% = \sum_{\boldsymbol{s}=1}^{\boldsymbol{S}} \frac{|L^p[i,j][\boldsymbol{s}]_{CPFEM} - L^p[i,j][\boldsymbol{s}]_{MKS}|}{\boldsymbol{S} \times |\langle L^p \rangle|} \times 100 \tag{5.9}$$

where $L^p[i,j][\boldsymbol{s}]_{CPFEM}$ denotes the value of the $[i,j]$ component of the plastic velocity gradient obtained from the CFEM simulation for bin $\boldsymbol{s}$, $L^p[i,j][\boldsymbol{s}]_{MKS}$ corresponds to the value predicted using the MKS localization framework and $\boldsymbol{S}$ denotes the total number of spatial bins comprised in the microstructure volume. In order to observe the influence of the truncation level on the accuracy of the prediction of the local values, the error between the MKS predicted values and the CPFEM results was obtained (using the error definition shown in Eq. (5.9)) for all the microstructures comprised in the validation ensemble for the five different localization kernels for each one of the components of the plastic velocity gradient tensor. Figure 12 shows the distribution of the calculated errors for all the components of the plastic velocity gradient as a function of the truncation level with the aid of an error bar plot.

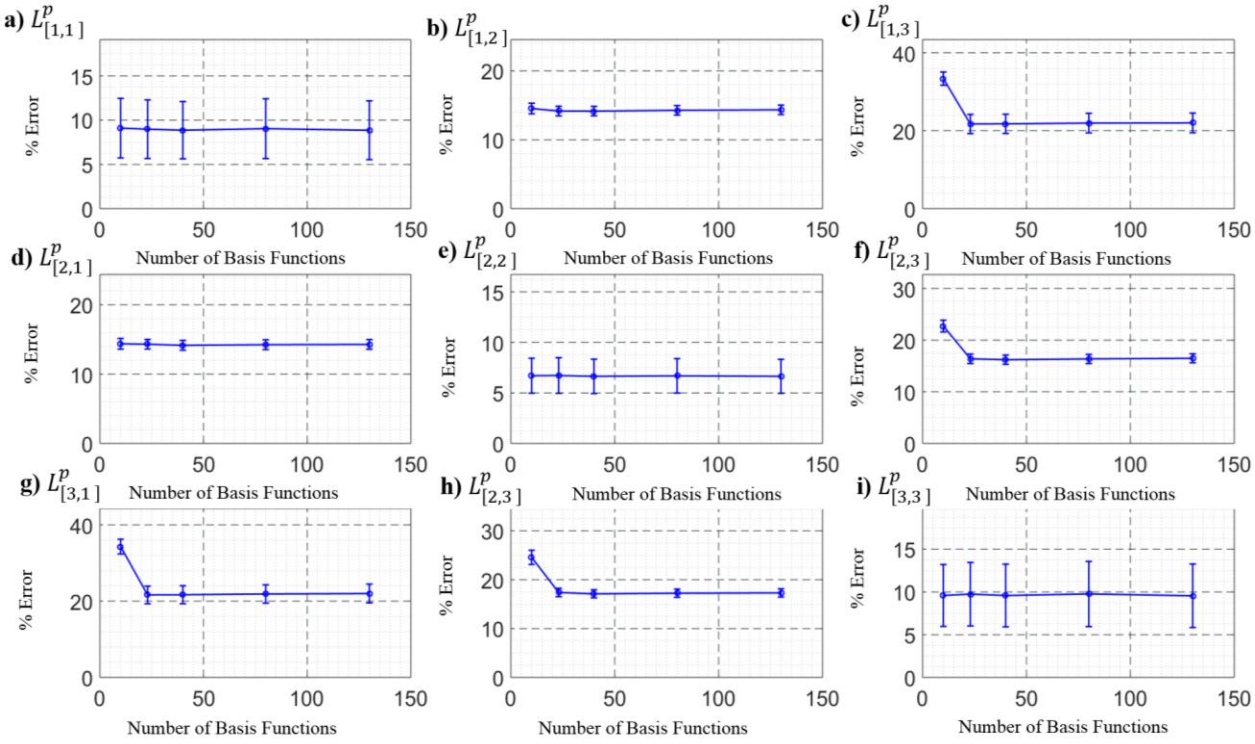

Figure 12: Distribution of Error Between the MKS Results and the CPFEM Results for All the Microstructures Comprised in the Validation Ensemble for Each One of the Components of the Plastic Velocity Gradient as a Function of the Truncation Level.

The error bar plots depicted in Figure 12a-f show the mean value of all the errors calculated for each different truncation level (i.e., maximum value of R), which corresponds to the number of GSH basis functions used, as well as the standard deviation from the obtained mean error (the error bars in Figure 12 corresponds to one standard deviation) for each component of the plastic velocity gradient tensor. The maximum value of deviation from the mean value of all the errors for all the components is 3.6%. From Figure 12 it can be seen that beyond 23 GSH basis functions, increasing the truncation level does not reduce the error between the MKS predicted values and the CPFEM predicted values. It is relevant to acknowledge that the error values presented in Figure 12 are not consistent with the error obtained in prior applications of the MKS approach (cf. [43-45, 48, 80]), as a matter of fact the error values shown are higher than prior MKS implementations. Also, notice

that the error of the off-diagonal components are significantly higher than the error of the diagonal components, a scenario also not consistent with prior MKS implementations where the error is constant throughout all the components being predicted[80]. Decomposing the plastic velocity gradient into its symmetric and antisymmetric components shows that the increment in error is caused by a subpar prediction of the anti-symmetric component of the plastic velocity gradient (cf. Figure 13 and Figure 14).

Figure 13 compares the local values predicted using the localization kernel that has 23 GSH basis functions (i.e., a truncation level of $l = 6$) of one of the microstructures of the validation ensemble to the local values obtained using a CPFEM simulation.

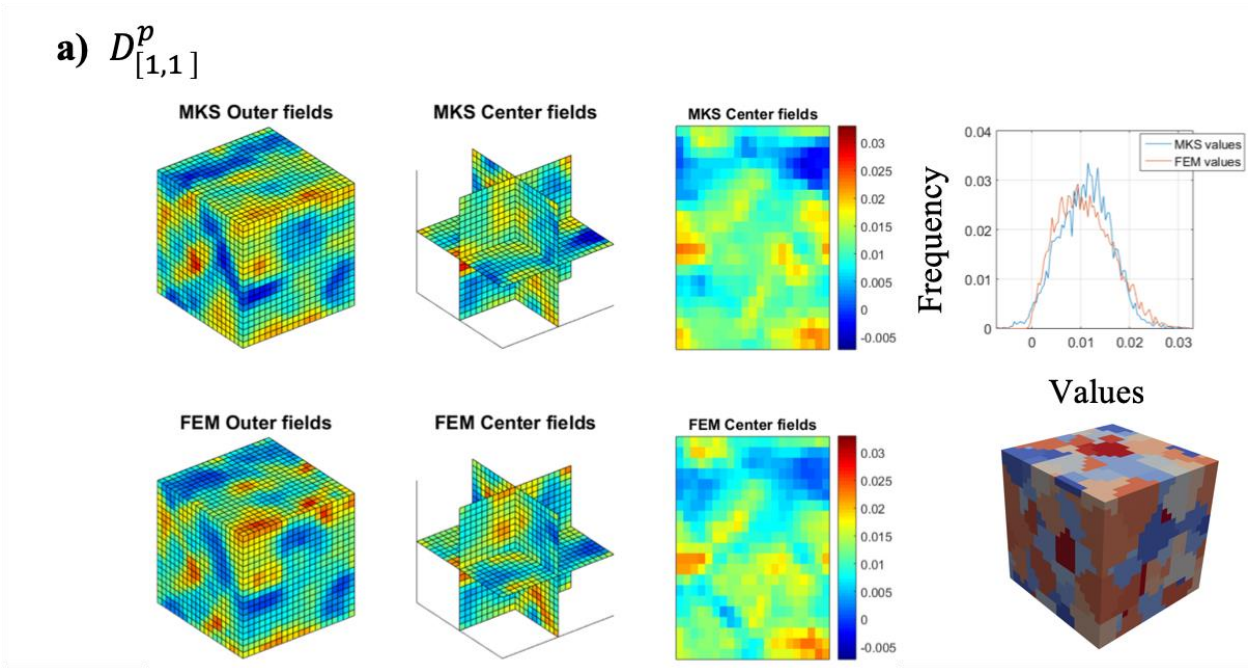

Figure 13: Comparison of the Predictions Obtained for One of the Components of the Symmetric Part of the Plastic Velocity Gradient Using the Calibrated Localization Kernels and the Results Obtained by Performing a CPFEM Simulation on the Polycrystalline RVE Shown Subjected to the Macroscopically Imposed Plastic Velocity Gradient Described by Eq. (5.7).

Figure 13a shows the response fields obtained using the calibrated localization kernels in conjunction with the trigonometric interpolation scheme (i.e., the MKS method) as well as the response fields obtained by performing a CPFEM simulation for one of the symmetric components of the plastic velocity gradient tensor ($D^p[1,1]$) for the polycrystalline RVE shown. Figure 13a also shows a comparison of the histograms of the frequency of the values predicted using both methods (MKS and CPFEM). Figure 13 shows reasonable agreement between the spatial response fields predicted using the MKS localization framework and the fields predicted using CPFEM. Finally, Figure 13also shows that the distribution of the values predicted by the MKS framework agree adequately with the distribution obtained by performing a CPFEM simulation. Similar results were also obtained for the fields of the off-diagonal components of the symmetric part of the plastic velocity gradient tensor (not shown in Figure 13).

Figure 14 compares the local values of the symmetric and anti-symmetric components for one of the off-diagonal components of the plastic velocity gradient ($L^p[1,3]$) predicted using the localization kernel that has 23 GSH basis functions (i.e., a truncation level of $l = 6$) for the same microstructure as Figure 13 to the local values obtained using a CPFEM simulation.

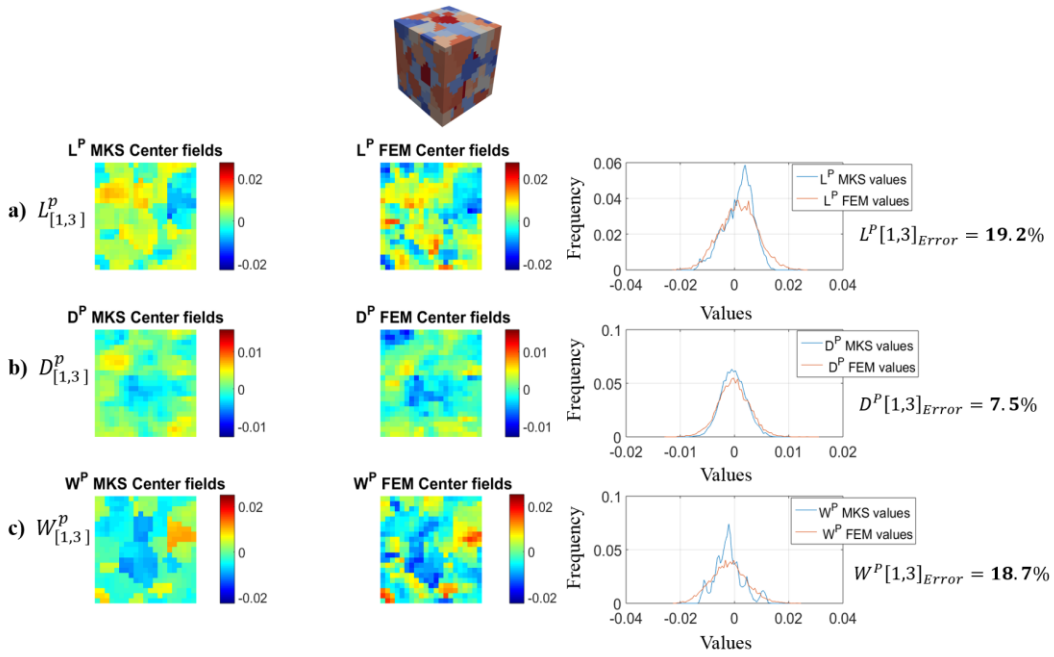

Figure 14: Comparison of the Predictions for the Symmetric and Anti-Symmetric Parts of the Plastic Velocity Gradient Obtained Using the Calibrated Localization Kernels and the Results Obtained by Performing a CPFEM Simulation on the Polycrystalline RVE Shown Subjected to the Macroscopically Imposed Plastic Velocity Gradient Described by Eq. (5.7).

Figure 14a shows the response fields obtained using the calibrated localization kernels in conjunction with the trigonometric interpolation scheme (i.e., the MKS method) as well as the response fields obtained by performing a CPFEM simulation for one of the off-diagonal components of the plastic velocity gradient tensor ($L^p[1,3]$) for the same polycrystalline RVE shown in Figure 13. Figure 14a also shows a comparison of the histograms of the frequency of the values predicted using both methods (MKS and CPFEM) and the associated error for that component (calculated using Eq. (5.9)). The fields and histograms shown in Figure 14a denote that the MKS method is not capable to predict the extreme values present in this component. Consequently, the MKS predictions have a high error. Figure 14b shows the response fields and histograms of the frequency of the values for the symmetric part of the plastic velocity gradient (i.e. $D^p[1,3]$) obtained via the MKS method and the traditional CPFEM method. As it can be seen,

Figure 14b shows reasonable agreement between the spatial response fields predicted using the MKS localization framework and the fields predicted using CPFEM and it also shows that the distribution of the values predicted by the MKS framework agree adequately with the distribution obtained by performing a CPFEM simulation. As a result, the error obtained for the symmetric component of the tensor is lower. Finally, Figure 14c shows the response fields and histograms of the frequency of the values for the anti-symmetric part of the plastic velocity gradient (i.e. $W^p[1,3]$) obtained via the MKS method and the traditional CPFEM method. The response fields shown in Figure 14c indicate that the MKS prediction for the anti-symmetric component of the tensor is not adequate and the histogram of values clearly demonstrates that the MKS method is not capable to predict the extreme values present in the anti-symmetric component of the plastic velocity gradient. Consequently, the error of the anti-symmetric component is quite high.

The decrease in accuracy exhibited by the local values predicted using the MKS framework in this chapter is caused by the significant heterogeneity present in the local values being predicted, which is in turn derived from the orientation dependence of the plastic deformation mechanisms that that drive/control the plastic deformation of the polycrystal (recall that "weak" crystallographic orientations will deform more than "strong" crystallographic orientations). The increased heterogeneity causes for the predictions obtained using only the first-order localization kernels to be adequate for the symmetric component of the tensor and subpar for its anti-symmetric component. Indeed, this limitation of the first-order terms has been observed in prior MKS implementations where the contrast in the microstructure of interest is high and only the first order localization kernels are used for predicting the local values[50]. The accuracy of the MKS framework was increased in this previous implementation when higher order terms were incorporated. Consequently, increasing the level of truncation of GSH basis functions will not

enable the calibrated kernels to provide better predictions of the local value (as Figure 12 shows). As a matter of fact, in order to obtain a more accurate prediction of the local values it is needed to incorporate the higher order localization kernels shown in Eq. (5.1). However, this is not a trivial task since the computational cost augments significantly if a direct incorporation is attempted, but promising new implementations of deep learning techniques have enabled a computationally efficient solution[94]. A protocol to increase the accuracy of the predicted responses by suitably training a deep learning model is developed and preliminarily validated in the next chapter.

Nevertheless, despite the increase in error observed, the predicted local values (and their associated distributions) for the symmetric-component of the plastic velocity gradient tensor (i.e. $\boldsymbol{D}^{p}$) using only the first-order localization kernels show adequate agreement with the values obtained using CPFEM (cf. Figure 14b). Therefore, demonstrating that the calibrated first-order localization kernels are capable of adequately predicting the plastic stretching tensor (i.e., the symmetric part of the plastic component of the velocity gradient) for polycrystalline microstructures on which they were not calibrated for any arbitrary plastic velocity gradient imposed at the macroscale. It is also important to recognize the significant computational savings obtained by predicting the local values using the MKS calibrated kernels. The CPFEM simulations took on average 90 minutes (5,400 seconds) on a single 2.4 GHz AMD processor node in the Georgia Tech super computer cluster to obtain the local values for each microstructure in the validation ensemble. On the other hand, the MKS predictions were obtained in only 4 seconds using the same resource. Thus, the MKS localization kernels are capable to predict reasonable predictions for the local values of the plastic stretching tensor two orders of magnitude faster than CPFEM.

The second and final validation case study in this section demonstrates that the calibrated first-order localization kernels are capable to procure adequate predictions of the local values of the symmetric component of the plastic velocity gradient for RVEs of different sizes. This validation also demonstrates that the computational savings obtained with the MKS framework are independent of the RVE size. For this case study, a new equiaxed microstructures containing approximately 1100 grains was created on a 43x43x43 spatial grid. Subsequently, the following macroscopic plastic velocity gradient tensor was imposed to the polycrystalline RVE of increased volume:

$$\langle L^p[i,j]\rangle = \begin{bmatrix} .0159 & 0 & 0 \\ 0 & -.0050 & 0 \\ 0 & 0 & -.0109 \end{bmatrix} \tag{5.10}$$

The macroscopic plastic velocity gradient denoted by Eq. (5.10) corresponds to imposing the following macroscopic stretching and spin rate:

$$\frac{\langle D^p[i,j]\rangle}{|\langle D^p[i,j]\rangle|} = \begin{bmatrix} .7986 & 0 & 0 \\ 0 & -.2523 & 0 \\ 0 & 0 & -.5463 \end{bmatrix}$$

$$\text{where } |\langle D^p[i,j]\rangle| = .02 \tag{5.11}$$

$$\langle W[i,j]\rangle = \begin{bmatrix} 0 & 0 & 0 \\ 0 & 0 & 0 \\ 0 & 0 & 0 \end{bmatrix}$$

The macroscopic plastic stretching tensor defined by Eq. (5.11) corresponds to $\theta = 48^{\circ}$, a boundary condition not sampled for when evaluating the $\boldsymbol{A}^L[i,j]^{PF}[\boldsymbol{t}]^{PF}[\theta]$ array. Nevertheless, as the previous case study showed the calibrated localization kernels can be used to localize the

macroscopic plastic velocity gradient defined in Eq. (5.10) by using the trigonometric interpolation scheme outlined in the previous section. However, it is important to recall that the calibrated kernels are defined on a 21x21x21 spatial grid. Therefore, their size needs to be extended in order to be employed for the larger polycrystalline RVE. Prior work has demonstrated that the required extension can be easily achieved using a resampling strategy called spectral interpolation, which corresponds to simply padding the calibrated kernels with zeros[44, 45, 48, 80, 84]. As a result, the local values of the plastic stretching tensor (i.e. the symmetric component of the local plastic velocity gradient) caused by imposing the macroscopic plastic velocity gradient defined in Eq. (5.10) to the 43x43x43 polycrystalline RVE were obtained using the MKS framework by leveraging the trigonometric interpolation scheme (to obtain the kernels for the new imposed condition) and spectral interpolation (to extend the size of the kernels to match the size of the RVE). The local values of this polycrystalline RVE were also obtained by performing a CPFEM simulation.

Figure 15 compares the local values predicted using the localization kernel with the $l = 4$ as the level of truncation (which corresponds to 10 basis functions) for the 43x43x43 polycrystalline RVE to the local values obtained using a CPFEM simulation.

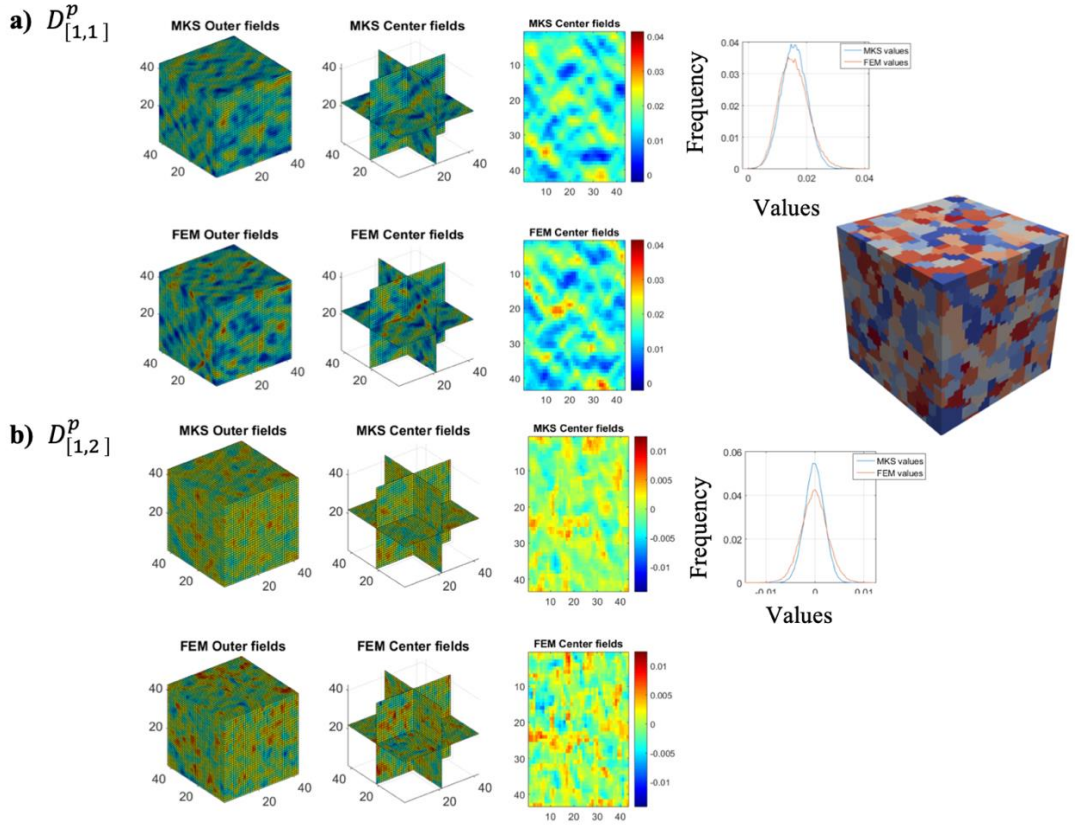

Figure 15: Comparison of the Predictions for Two Components of the Symmetric Part of the Plastic Velocity Gradient Obtained Using the Calibrated Localization Kernels and the Results Obtained by Performing a CPFEM Simulation on the 43x43x43 Polycrystalline RVE shown Subjected to the Macroscopically Imposed Plastic Velocity Gradient Tensor Described by Eq. (5.10).

Figure 15a-b shows the response fields obtained using the MKS method (i.e., using the calibrated localization kernels in conjunction with the trigonometric interpolation scheme and the spectral interpolation) as well as the response fields obtained by performing a CPFEM simulation for the 43x43x43 polycrystalline RVE of two components of the plastic stretching tensor ($D^p[1,1]$ and $D^p[1,2]$). Figure 15a-b also shows a comparison of the histograms of the frequency of the values predicted using both methods (MKS and CPFEM). Figure 15 shows reasonable agreement between the spatial response fields predicted using the MKS localization framework and the fields predicted using CPFEM. Finally, Figure 15 also shows that the distribution of the values predicted

by the MKS framework agree adequately with the distribution obtained by performing a CPFEM simulation. It is important to acknowledge that similar results were also obtained for all the other components of the plastic stretching tensor (not shown in Figure 15). Table 3 shows the error between the MKS predicted values and the CPFEM values (calculated using the definition of error between established in Eq. (5.9)) for each one of the six components of the plastic stretching tensor for the RVE shown in Figure 15.

Table 3: Mean Error (%) between the CPFEM and the MKS predicted values for the microstructure shown in Figure 15 subjected to boundary conditions expressed in Eq. (5.10).

Strain Rate Tensor Component	Error for Equiaxed Microstructure (%)
$D^p_{[1,1]}$	12.1
$D^p_{[1,2]}$	7.4
$D^p_{[1,3]}$	7.9
$D^p_{[2,2]}$	8.7
$D^p_{[2,3]}$	8.8
$D^p_{[3,3]}$	11.4

The performed validation case study demonstrates that the calibrated localization kernels can be extended as needed to obtain adequate predictions of the local values of the symmetric part of the plastic component of the velocity gradient for RVEs of extended size. Finally, it is important to recognize that the computational savings obtained by predicting the local values using the MKS framework are significantly more evident in this case because the CPFEM simulation took on 77 hours (277,200 seconds) on a single 2.4 GHz AMD processor node in the Georgia Tech super computer cluster to obtain the local values for the 43x43x43 polycrystalline RVE. On the other

hand, the MKS predictions were obtained in only 21 seconds on the same resource. As a result, the MKS framework is up to 4 orders of magnitude faster than CPFEM. Thus, demonstrating that the computational savings obtained by using the MKS framework are independent of the RVE size and actually much more noticeable when the RVE size increases.

5.4 Summary and Conclusions

The case studies performed in the last section demonstrate that the MKS localization framework is capable providing good predictions for all components of the second-rank local plastic stretching tensor for any given macroscale imposed plastic velocity gradient and for any desired volume of polycrystalline RVE with significant computational savings. Thus, successfully achieving the first implementation of the MKS framework to polycrystalline plasticity. Unfortunately, these case studies also demonstrated that suitable extension need to be defined in order to enable more accurate predictions of the complete local plastic response (i.e., the local values of the plastic stretching tensor and the local values of the spin tensor).

CHAPTER 6:

Establishing Accurate Localization Linkages for the Plastic Deformation of Polycrystalline RVEs using Deep Learning Approaches

The case studies performed in the last chapter demonstrated that the localization relationship defined in Eq. (5.5) is capable of providing adequate responses of the local plastic stretching tensors caused by an arbitrary macroscopically imposed plastic velocity gradient. Unfortunately, these case studies also demonstrated that the first-order localization kernels provide a subpar prediction of the local values of the spin tensor (cf. Figure 14). This means that the physics captured with the first-order kernels are not sufficient to procure accurate predictions of the local values of the plastic component of the velocity gradient. Consequently, the first-order kernels fail to capture the highly heterogeneous physics that control the plastic deformation in polycrystalline RVEs. Therefore, in order to increase the accuracy of the predicted local values it is needed to incorporate in a more detailed manner the contribution that local states at other spatial locations in the material microstructure have in the value of the local response of interest.

A direct manner to accomplish this goal is by incorporating the higher-order kernels denoted in Eq. (5.3). However, calibrating the values of the higher-order localization kernels to the results from numerical simulations is not trivial because the number of terms is unimaginably large and also because the DFT transformation does not fully decouple all the higher-order localization kernels. Therefore, one cannot leverage the protocols used previously in this dissertation to calibrate the values of the higher-order kernels. Nevertheless, previous work defined a robust and systematic approach to calibrate the values of higher-order localization kernels for multi-phase composites by adequately incorporating details of the neighborhood into the microstructure function [50]. Therefore, in order to enable the calibration of the higher-order

localization kernels one needs to reformulate the microstructure function of polycrystalline RVEs to incorporate the details of the neighborhood. As an example, let $\tilde{f}_{\boldsymbol{s}}(g_0, g_1, g_2, g_3, g_4, g_5, g_6)$ denote a reformulated microstructure function that enumerates all the possible combinations of local states that can exist on a neighborhood comprised by the first nearest neighbors in a 3D polycrystalline RVE for seven different given Bunge-Euler angles at bin $\boldsymbol{s}$. Figure 16 schematically shows the different voxels that define the aforementioned neighborhood in a 3D polycrystalline RVE as well as the index used to identify each of the different orientations being considered.

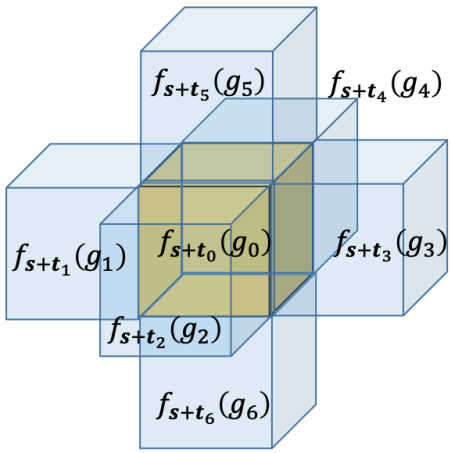

Figure 16: Schematic of the Reformulated Microstructure Function that Incorporates the Details of the First Nearest Neighbors in a 3D Polycrystalline RVE.

Figure 16 shows that the reformulated microstructure function defined for the bin indicated with a yellow color contains information about the local state of seven different voxels. Let $F^R_{\boldsymbol{s}+\boldsymbol{t}_i}$ denote the GSH coefficients associated with the crystal lattice orientation of the ith voxel in the neighborhood depicted in Figure 16. Therefore, in order to obtain all the possible combinations of local states that can exist on the neighborhood depicted in Figure 16 one needs to successively multiply the GSH coefficients of the voxels comprised in that neighborhood as Eq. (6.1) shows:

$$\tilde{F}_{\boldsymbol{s}}^{R} = F_{\boldsymbol{s}+\boldsymbol{t}_0}^{R} \cdot F_{\boldsymbol{s}+\boldsymbol{t}_1}^{R} \cdot \ \ldots \ \cdot F_{\boldsymbol{s}+\boldsymbol{t}_6}^{R} \tag{6.1}$$

where $\tilde{F}_{\boldsymbol{s}}^{R}$ denotes the result of successive multiplication for the voxel $\boldsymbol{s}$. Therefore, reformulating the microstructure function such that the local state characterizes not only the voxel of interest, but the neighborhood of its first nearest neighbors enables one to recast Eq. (5.3) into the following expression:

$$\boldsymbol{L}^{p}{}_{\boldsymbol{s}} = \left(\sum_{\boldsymbol{t}}^{\boldsymbol{S}} \int_{FZ} \tilde{A}_{\boldsymbol{s}+\boldsymbol{t}}^{R} \left(\frac{\langle \boldsymbol{D}^{p} \rangle}{|\langle \boldsymbol{D}^{p} \rangle|} \right) \tilde{F}_{\boldsymbol{s}+\boldsymbol{t}}^{R} \left(\frac{\langle \boldsymbol{D}^{p} \rangle}{|\langle \boldsymbol{D}^{p} \rangle|} \right) dg \right) \langle \boldsymbol{D}^{p} \rangle + \langle \boldsymbol{W} \rangle \tag{6.2}$$

where $\tilde{A}_{\boldsymbol{s}}^{R} \left(\frac{\langle \boldsymbol{D}^{p} \rangle}{|\langle \boldsymbol{D}^{p} \rangle|} \right)$ denote the influence kernels that capture the effect of the first nearest neighbors corresponding to a macroscopically imposed plastic velocity gradient. As a result, directly incorporating information about the neighborhood of a voxel into the microstructure function enables one to systematically capture the contribution of the local states at other spatial locations in the material microstructure. Therefore, this new formulation will enable a better prediction of the local values. Finally, it is important to recognize that this new microstructure function can be subsequently extended to incorporate other neighborhoods of the voxel such as the second-nearest neighbors, etc. (cf. [50]). The localization relationship defined in Eq. (6.2) enables for one to leverage the traditional calibration protocols to obtain the values of the kernels [43, 49] because a DFT transformation successfully decouples the kernels from the microstructure function. However, calibrating the value of these reformulated coefficients for the polycrystalline structures of interest in this work will not only require significant power but also an absurd amount of time due to the massive amount of terms that need to be calibrated. For example, using the smallest level of truncation for the GSH basis functions for single-phase cubic triclinic polycrystalline

RVEs (which is $l = 4$ and corresponds to 10 basis functions) requires for one to calibrate for 10^7 features.

As one can imagine there are significant challenges that need to be addressed in order for one to establish a robust model capable of predicting 10^7 features. Among these many challenges the most obvious one is the fact that one would need at least 10^7 numerical simulations results to calibrate the values of the kernels in order to lower the chances of overfitting. As a result, one can clearly see that the main impasse hindering the efficient implementation of the localization relationship defined in Eq. (6.2) is caused by the vast number of features that need to be generated, and subsequently calibrated, in order to incorporate details about the neighborhood. Recall that the increased number of features was needed to enable the localization kernels to capture the effect that local states present in the neighborhood of the voxel of interest have on the response. Therefore, there is a clear need for a strategy that enables one to identify a set of consistent features that are transferable from one material system to another and to subsequently train the identified features in a computationally efficient manner.

6.1 Deep Learning Approaches to Localization

Deep learning approaches are a viable solution to this problem because their great learning capability enables them to automatically identify salient features that capture the details of the neighborhood directly from the raw input data and also enables them to train the identified features better than traditional machine learning methods[95-97].A deep learning model of particular interest to this dissertation is the Convolutional neural network (CNN). CNNs automatically identify (i.e., with no human intervention and completely driven by the data) local patterns of features, commonly referred as feature maps, from the provided raw data by superimposing different filters and then convolving them with the input data (hence the name). Subsequently,

CNNs link the identified features maps to the response of interest by feeding these features maps into fully-connected layers. Therefore, in few words, CNNs are a robust machine learning technique that enables one to identify a set of consistent (spatially localized) features (i.e., local patterns in the neighborhood) and subsequently use them to build accurate models. The way in which CNNs builds models makes them specifically suitable for pattern/image recognition applications [95, 98, 99]. Prior work from our research group has successfully implemented this machine learning technique to train accurate models for both localization and homogenization relationships for multi-phase composites with high contrast difference [94, 100, 101]. Therefore, leveraging the previous successes of deep learning implementation, this chapter provides the details for developing a CNN capable of predicting the local plastic response caused by a plastic velocity gradient imposed at the macroscale in 3D polycrystalline aggregates. Thus, representing the first successful implementation of deep learning models for localizing the plastic response in polycrystalline RVEs. The developed deep learning model is trained on the same types of polycrystalline microstructures used throughout this dissertation (i.e., FCC, single-phase and with cubic-triclinic symmetry).

It is important to acknowledge that the implementation of deep learning approaches needs to be systematic. As a result, this dissertation will focus solely on localizing a single plastic velocity gradient imposed at the macroscale. The subsequent extension to enable an efficient localization for any arbitrary plastic velocity gradient imposed at the macroscale will be addressed in future work and will not be considered in the scope of this dissertation. However, it is important to recognize that the protocols developed in Chapter 4 and 5 can be suitably leveraged to train a deep learning model in the principal frame of the imposed deformation. Moreover, the interpolation scheme that enables the appropriate resampling and transformation of the localization kernels can,

and must, also be leveraged to suitably transform the filters comprised in the convolutional layers that create the feature maps that link the local values of the plastic response to the tensor imposed at the macroscale in any arbitrary sample frame.

6.1.1 Development of Deep Learning Model

This section leverages the typical CNN architecture (illustrated in Figure 17) to build and accurate deep learning model capable of accurately predicting the local plastic response caused by imposing a macroscopic plastic velocity gradient.

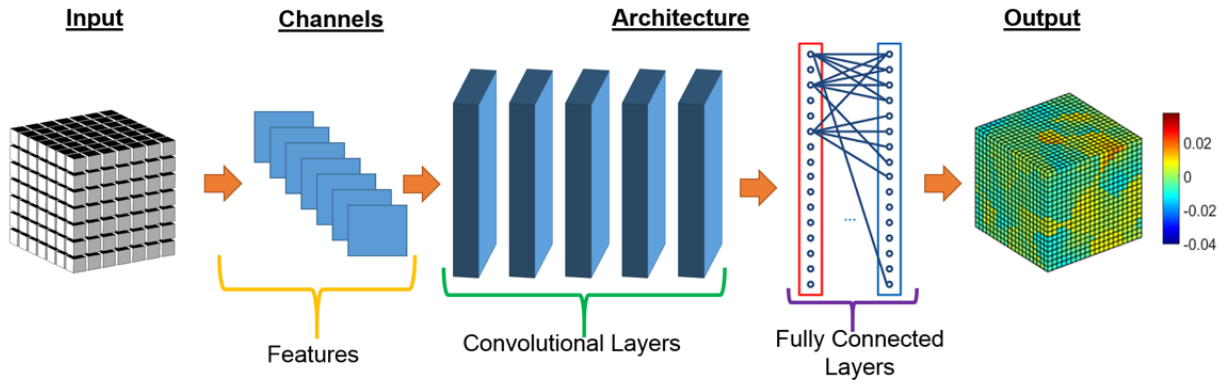

Figure 17: CNN Architecture Leveraged to Build a Robust and Accurate Deep learning Model for Predicting the Local Plastic Response Caused by a Macroscopically Imposed Plastic Velocity Gradient.

Figure 17 shows the general CNN architecture used in this section to develop an accurate localization model for the plastic response of polycrystalline materials. The input of the CNN is the local state that describes the internal structure of the polycrystalline RVE. Recall that the local state for single-phase polycrystalline materials is characterized by the spatially resolved ODF (cf. Chapter 2 section 2.2) suitably represented with GSH basis functions. Remember that the GSH representation of the local state is leveraged because it provides a compact representation of the functions defined in orientations space that inherently accounts for all symmetries present in the

polycrystalline RVE. Therefore, the input channels to the CNN are the GSH coefficients that represent the crystal lattice orientation at each point on the RVE.

The architecture of the CNN shown in Figure 17 denotes that different convolutional layers are used to identify feature maps that will be subsequently used to localize the plastic response in polycrystalline materials. Recall that this type of layers identify the feature maps from the input data by convolving different superimposed filters with the input data. The microstructures of interest in this dissertation are 3D polycrystalline RVEs. As such, 3D filters are leveraged in this work. A general convolutional layer leveraged in this work takes as an input a 3D polycrystalline volume discretized into voxels of uniform volume (the size used in this dissertation corresponds to a 21x21x21 volume) with N channels (corresponding to the GSH coefficients that represent the crystal lattice orientation at each voxel). The 3D volumes associated with each channel are convolved with 3-D convolutional filters each of size $m \times m \times m$. The mathematical representation of the described convolutional layer is the following:

$$O(x,y,z) = \sum_{q=0}^{N-1} \sum_{k=0}^{m-1} \sum_{j=0}^{m-1} \sum_{i=0}^{m-1} I\left(x - \frac{m-1}{2} + i, y - \frac{m-1}{2} + j, z - \frac{m-1}{2} + k, q\right) \times \mathcal{W}(i,j,k,q) + b \tag{6.3}$$

where O denotes the output of the convolution with the filter, q denotes the channel, I denotes the input and x, y and z denote the position of a voxel in the 3D volume. Finally, $\mathcal{W}$ and b are the weight and bias of the filters that once trained, generate the desired feature maps when convolved with the input RVE. CNNs enable one to capture non-linear functional mappings between the input and the output by passing the output O through a non-linear activation function in order to obtain the final value of O at voxel (x, y, z). This dissertation applies the typically used ReLU (rectified linear unit) [102], defined as follows $f = \max(0, x)$, to all the voxels in the output 3D volume from the convolution. Superimposing various convolutional layers enables a CNN to

define more and more intricate features maps that incorporate more and more details of the neighborhood defined by the size of the filter being convolved. Notice that the successive convolution of filters causes for the output volume to be smaller than the input volume. Therefore, in this dissertation adequate "wrapping" (i.e., repeating the information contained in the defined RVE volume) was leveraged in order to ensure that the output of the developed models to be of the same size as the input RVE volume.

Finally, the architecture depicted in Figure 17 shows that the last layers of the CNN are fully-connected (FC) layers. This type of layers train the model that links the response of interest to the feature maps (flatted to a one-dimensional vector) generated from the various stacked convolutional layers by leveraging multiple layers of fully connected neurons (hence the name). Neurons are the basic computing unit for artificial neural networks and compute an output from an input by performing the following operation:

$$o_k = f(\sum_{i=0}^{n-1} x_k(i) \times \mathrm{w}_k(i) + b_k) \tag{6.4}$$

where $o_k$denotes the output computed for the kth neuron in the FC layer, $f(\,)$ represents the non-linear activation function (ReLU is used as well for this type of layer), $x_k(i)$ denotes the ith input and $w_k(i)$ and b_k are the weight and bias (respectively) that compute the output of the neuron (their values are obtained during the training of the model). Finally, n specifies the total number of inputs to the neuron. It is important to recognize that all the neurons in a fully connected layer are connected to all the neurons or outputs of the previous layers. Therefore, one can see that the addition of fully connected layers enables one to obtain linear and non-linear combinations of all the feature maps previously identified with the help of the convolutional layers.

Once the main components of the architecture of the CNN have been discussed and introduced it is necessary to define a calibration ensemble on which to train the CNN. In this work, local values of the plastic component of the velocity gradient obtained from CPFEM simulations performed over synthetically generated microstructures were used to train the weights and biases of the different convolutional and fully connected layers. The calibration ensemble needs to be diverse and vast in order to capture as much interactions as possible between the local states. Specially, when the expected number of parameters to be trained is significant. For that reason, it was decided to extend the calibration ensemble depicted in Figure 10. Figure 18 shows the new calibration ensemble of microstructures and orientations used to train the deep learning model.

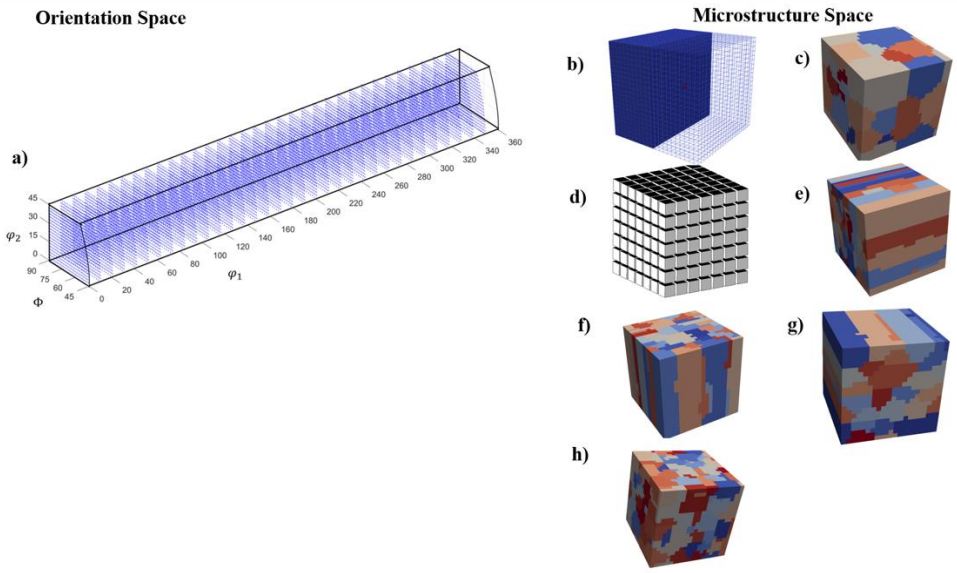

Figure 18: Calibration Ensemble Used to Train the Deep Learning Model.

Figure 18 shows 20,000 different crystal lattice orientations sampled from the fundamental zone of cubic lattice orientations and Figure 18 b-h show the seven different microstructure types comprised in the calibration ensemble. Figure 18b shows an instantiation of a delta microstructure. Figure 18c shows an instantiation of an equiaxed microstructure, all instantiations of this type of

microstructure were generated using the Dream.3D software package[88] and each one of them has an approximate of 25 grains. Figure 18d shows a schematic of a random microstructure instantiation. These types of microstructures are generated by randomly placing an orientation into each one of the volume elements of the RVE. Figure 18e-g depict rolled microstructures with grains elongated along the X, Z and Y directions, respectively, each instantiation contains approximately 25 grains and Figure 18h shows another type of equiaxed microstructure (also generated using Dream.3D) but with more grains since each instantiation has between 300 and 800 grains. The calibration ensemble shown in Figure 18 considers 3000 different instantiations of each microstructure type. Thus, comprising a total of 21,000 different microstructures capturing the interaction of 20,000 different Bunge-Euler angles. The plastic velocity gradient tensor imposed to all the microstructures in the calibration ensemble is the following:

$$\langle L^p[i,j]\rangle = \begin{bmatrix} .008 & 0 & 0 \\ 0 & .008 & 0 \\ 0 & 0 & -.016 \end{bmatrix} \tag{6.5}$$

Similarly, as performed in Chapter 5, the numerical results of the calibration ensemble were obtained by performing a CPFEM simulation for each microstructure on the calibration ensemble for the macroscopic plastic velocity gradient described by Eq. (6.5). Each microstructure instantiation in the calibration ensemble was discretized with a 21x21x21 finite element mesh using continuum elements (C3D8)[83] and subsequently deformed to a total strain of 0.02 using periodic boundary conditions and the commercial FE package ABAQUS [83], which allows the specification of the material constitutive laws through a user subroutine called UMAT. The UMAT used in this work employed the elastic-viscoelastic crystal plasticity theory (with a rate-sensitivity of 0.01) along with a computationally efficient implicit time-integration scheme that was extensively validated in prior work for fcc metals [14, 89]. High values of elastic moduli were assigned in all

the CPFE simulations to limit the elastic strains to small numbers (~0.001), and slip hardening rates were set to zero. The volume and time averaged local plastic velocity gradient over the 0.01-0.02 range of the total macroscopically imposed plastic velocity gradient was extracted from the CFEM simulation for each voxel (corresponding to an element in the FE model) and documented as $\boldsymbol{L}^{p}[\boldsymbol{s}]^{PF}$. Once the numerical results of the calibration ensemble were obtained different variations of the CNN architecture depicted in Figure 17 were explored in order to define the best deep learning model capable of accurately localizing the plastic response in polycrystalline materials. The parameter explored were the number of convolutional layers, the number of channels in each convolution, the size of the convolutional kernel/filter, the number of fully connected layers and the number of neurons in each fully connected layer. The architecture of the CNN that yielded the best model is shown in Table 4. It is important to mention that the convolutional layers used in this architecture have 64 $5 \times 5 \times 5$ 3D filters.

Table 4: Details of the best performing CNN architecture (bs. denotes the batch size).

Layer	Dimension
Input Layer	bs. $\times 41 \times 41 \times 41 \times 10$
Convolutional Layer 1	bs. $\times 37 \times 37 \times 37 \times 64$
Convolutional Layer 2	bs. $\times 33 \times 33 \times 33 \times 64$
Convolutional Layer 3	bs. $\times 29 \times 29 \times 29 \times 64$
Convolutional Layer 4	bs. $\times 25 \times 25 \times 25 \times 64$
Convolutional Layer 5	bs. $\times 21 \times 21 \times 21 \times 64$
Fully Connected Layer 1	bs. $\times 1024$
Fully Connected Layer 2	bs. $\times 512$
Output Layer	bs. $\times 9$

It is important to notice that the size of the 3D volume in the input layer is bigger than the 21x21x21 defined RVE size. This bigger volume was generated by adequately "wrapping" the input 3D RVE volume to ensure that the final feature map is the size of the input volume. Notice that this CNN architecture creates a 3D feature map with 64 features that characterize the whole neighborhood of the voxel of interest (i.e., each feature in the feature map incorporates details of all the voxels in the microstructure) at the end of convolutional layer 5. Subsequently, the identified feature map is "flattened" to a one dimensional vector and fed as an input to 2 fully connected layers that adequately train the localization model. Finally, the output layer generates nine values per voxel, each value representing the prediction of each component of the plastic velocity gradient. The CNN architecture depicted in Table 4 was implemented in PyTorch and was trained using the Adam optimizer [103] with default parameters. The batch size used during the training was set to one. The training process of the CNN was stopped after 40 epochs (i.e., 40 complete passes of the entire calibration dataset).

Finally, in order to provide a benchmark of performance, the first-order MKS localization kernels were calibrated to the same numerical results by performing linear regression (i.e., minimizing the sum of squared error) on Eq. (5.5) in the DFT space and by selecting a truncation level $l = 6$, which corresponds to 23 GSH basis functions. Recall that beyond this level of truncation the predictions of the local values did not improve (cf. Figure 12).

6.1.2 Validation of the developed Deep Learning Model and Performance Comparison with the MKS First-Order Localization Kernels Predictions.

In this section it is demonstrated that the deep learning model trained with the CNN architecture shown in Table 4 is capable of procuring accurate predictions of the local plastic response for polycrystalline RVEs on which the model was not trained. In other words, the weights

and biases of the trained CNN are independent of the microstructure and can be leveraged to procure accurate prediction for new, unseen polycrystalline RVEs. This section also demonstrates the performance improvement of the predictions obtained with the CNN-trained deep learning model by comparing the deep-learning predictions to the first-order MKS localization predictions (i.e., the localization relationship express in Eq. 5.5).

The local values of the plastic response will be obtained for a brand new ensemble of microstructures (i.e., a validation ensemble). This new validation ensemble contains four new different microstructure types and sampled 3500 new (i.e., not contained in the original orientation calibration ensemble) Bunge-Euler angles from the FZ_C. As a result, the morphology (i.e., shape, size and spatial arrangement of the grains) as well as the crystal lattice orientations of the microstructures in validation ensemble are completely different from the microstructures comprised in the calibration ensemble. Figure 19 shows the new validation ensemble used in this section.

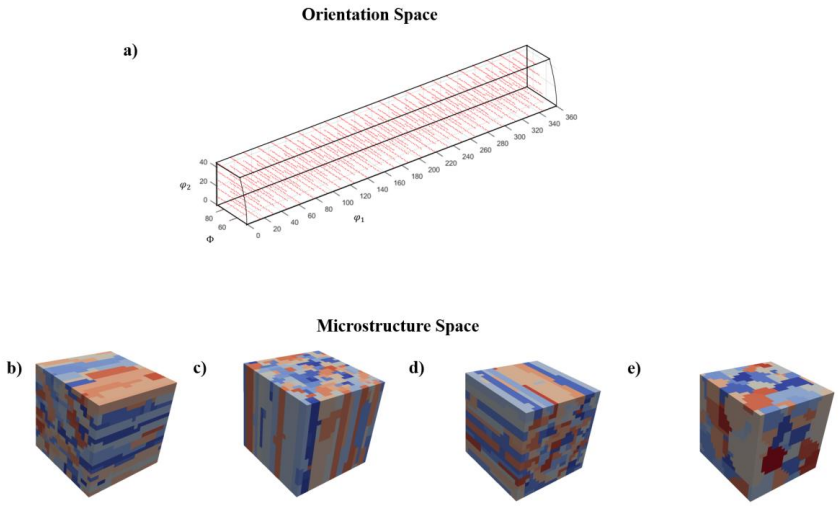

Figure 19: Ensemble of Microstructures and Orientations Used to Validate the CNN-Trained Deep Learning Model.

Figure 19a shows the 3500 new crystal lattice orientations (Bunge-Euler angles) sampled from the FZ_C. Figure 19b-e show the new different microstructure types comprised in the validation ensemble. Figure 19b-d depict rolled microstructures with grains elongated along the X, Z and Y directions, respectively, with approximately 120 grains, 50 instantiations of these types of microstructures are comprised in the validation ensemble. Notice that the rolled microstructures present in the calibration ensemble only had 25 grains. Figure 19e shows a new type of equiaxed microstructure that comprises approximately 120 grains, 50 instantiations of this new equiaxed microstructure type are comprised in the validation ensemble. Again, it is important to note that the equiaxed microstructure depicted in Figure 19 is different from the one present in the calibration ensemble because it has a different number of grains. As a result, the validation ensemble encompasses a total of 200 new microstructures. The local values caused by imposing the macroscopic plastic stretching tensor defined in Eq. (6.5) were obtained for each microstructure in the validation ensemble using the deep learning model trained in the previous section, these values were also obtained by using the first-order MKS localization kernels. Finally, the local values were also obtained by performing a CPFEM simulation, these values are considered to be the ground truth. The error difference that the CNN predicted values and the first-order MKS predicted values have with the ground truth values (i.e., the CPFEM values) is defined as follows[50]:

$$Err[i,j]\% = \sum_{\boldsymbol{s}=1}^{\boldsymbol{S}} \frac{\left| \hat{L}^p[i,j][\boldsymbol{s}] - L^p[i,j][\boldsymbol{s}] \right|}{\boldsymbol{S} \times |\langle L^p \rangle|} \times 100 \tag{6.6}$$

where $\boldsymbol{S}$ denotes the total number of spatial bins comprised in the microstructure volume, $\hat{L}^p[i,j][\boldsymbol{s}]$ denotes the model predicted value of the $[i,j]$ component of the plastic velocity gradient for bin $\boldsymbol{s}$ and $L^p[i,j][\boldsymbol{s}]$ corresponds to the ground truth value obtained from the CPFEM

simulations. In order to observe the difference between the deep learning model and the MKS model, the error difference was obtained for all the microstructures comprised in the validation ensemble. Table 5 shows the mean error obtained for all the microstructures in the validation set along with the standard deviation for each component of the plastic velocity gradient.

Table 5: Mean Error (%) table for the deep learning model predictions and the first-order MKS localization model predictions for the entire validation set shown in Figure 19 when subjected to the boundary condition defined in Eq. (6.5).

Strain Rate Tensor Component	Error for the CNN trained model (%)	Error for the first-order MKS localization model (%)
$L^p_{[1,1]}$	$6.45 \pm .66$	8.91 ± 1.21
$L^p_{[1,2]}$	$8.07 \pm .35$	$13.72 \pm .61$
$L^p_{[1,3]}$	$10.29 \pm .51$	$19.75 \pm .96$
$L^p_{[2,1]}$	$8.09 \pm .34$	$13.74 \pm .61$
$L^p_{[2,2]}$	$6.41 \pm .69$	8.89 ± 1.3
$L^p_{[2,3]}$	$10.31 \pm .50$	$19.81 \pm .98$
$L^p_{[3,1]}$	$10.55 \pm .53$	$20.02 \pm .96$
$L^p_{[3,2]}$	$10.53 \pm .52$	$20.02 \pm .91$
$L^p_{[3,3]}$	$7.79 \pm .98$	10.38 ± 1.55

Table 5 demonstrates the palpable improvements of the predictions across the whole validation ensemble since it clearly shows that the mean error for the CNN-trained deep learning is consistently lower than the mean error obtained for the first-order MKS localization model for all the components of the plastic velocity gradient. Therefore, demonstrating that the deep learning

predicted values are more accurate than the ones obtained using the first-order MKS localization model. Figure 20 compares the fields of the local plastic response predicted using the deep learning model, the first-order MKS localization model and the CPFEM simulation.

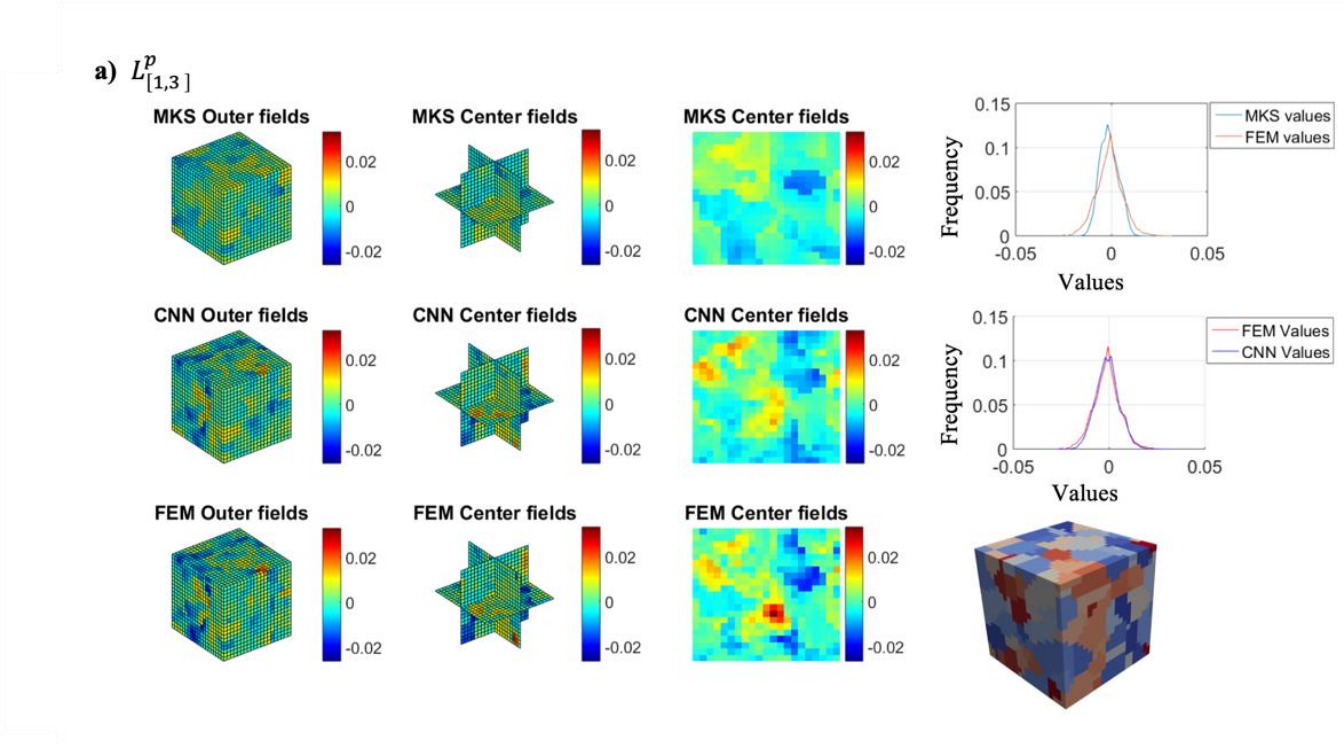

Figure 20: Comparison of the Predictions for one of the Components of the Plastic Velocity Gradient Obtained using the Deep Learning Model, the First-Order MKS Localization Model and the CPFEM Simulation for One of the Polycrystalline RVEs in the Validation Ensemble Subjected to the Macroscopically Imposed Plastic Velocity Gradient Described in Eq. (6.5).

Figure 20 reveals that the local plastic velocity gradient fields obtained using the deep learning model show better agreement with the ground-truth fields obtained by performing the CPFEM simulation. Figure 20 also shows that the deep-learning model is capable to predict better the extreme values present in the field. As a result, the distribution of values predicted using the deep learning model is closer to the distribution of values obtained using the CPFEM simulation. The local fields of the plastic velocity gradient for the same RVE shown in Figure 20 were

decomposed into its symmetric and anti-symmetric components to assess the performance of the deep learning model at capturing these two different components.

Figure 21 shows the fields of the local values of the plastic component of the plastic velocity gradient for a center slice of the same polycrystalline RVE depicted in Figure 20 as well as its symmetric and anti-symmetric components predicted using the deep learning model, the first-order MKS localization model and the CPFEM simulation. The fields shown correspond to one of the off-diagonal components of the plastic velocity gradient ($L^p[1,3]$).

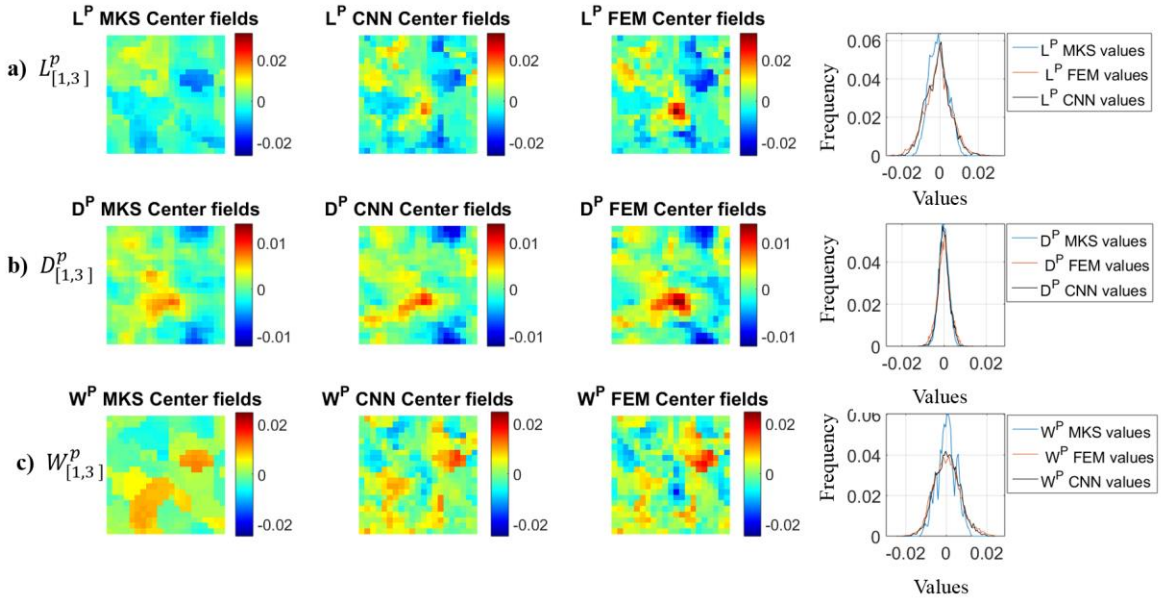

Figure 21: Comparison of the Symmetric and Anti-symmetric Fields Obtained for One Component of the Plastic Velocity Gradient Using the Deep Learning Model, the First-Order MKS Localization Model and the CPFEM.

Figure 21a clearly shows that the fields of the local values of the plastic component of the plastic velocity gradient obtained with the deep learning model show better agreement with the fields obtained with the CPFEM simulation. Not only that, the histogram that compares the

distribution of values obtained using the three different methods shows that the deep learning model was capable to predict the extreme values and therefore shows better agreement. A similar behavior is observed for the symmetric part of this component ($D^p[1,3]$) where the fields and values predicted with the deep learning model show better with the CPFEM fields. Finally, the greatest improvement is observed in the anti-symmetric part ($W^p[1,3]$) of this component. The distribution of values obtained with the deep learning model shows a clear improvement from those obtained with the first-order MKS localization model as well as the resultant fields. The improvement of the predictions using the deep learning model is substantial. Therefore, demonstrating that the deep learning model is capable to capture the highly heterogenous physics associated with the plastic deformation of polycrystalline materials better than the first-order MKS localization model.

6.2 Summary and Conclusions

The validation case study performed in this chapter demonstrated that accounting in a more detailed manner for the effect that local states at other spatial locations in the RVE have in the value of the local response of interest yields better predictions of the local values. This case study also demonstrated that the most robust technique to incorporate these effects is through deep learning approaches such as CNNs.

CHAPTER 7:

Conclusions

The work presented in this dissertation culminated in palpable and measurable advancements relevant to hierarchical multiscale modeling efforts. Specifically, this dissertation introduced three major advancements relevant to these efforts.

The first advancement eliminated one of the major impediments that hindered the wide-spread adoption of the MKS localization framework as a practical scale-bridging framework in fully-coupled multiscale modeling efforts by enabling it to accurately predict the local plastic response caused by any arbitrary periodic boundary condition imposed at the macroscale. The advancement consisted on defining a computational strategy that facilitated the efficient calculation of the localization kernels at any desired sample reference frame from a finite and compact spectral database of localization kernels calibrated in the principal frame of the macroscopically imposed periodic boundary condition.

The second advancement consisted in successfully implementing the MKS framework for modeling the localization of the plastic response in polycrystalline microstructures. This advancement was achieved by effectively incorporating the previously enhancements that enabled the MKS localization framework undertake the localization problem for complex material structures and non-linear phenomena into a newly defined localization relationship. As a result, a spectral database of localization kernels suitably represented with GSH functions was calibrated in the principal frame of the macroscopically imposed periodic boundary condition.

The third advancement consisted in the development of a robust methodology that enables the successful incorporation of deep learning techniques for modeling the localization of plasticity in polycrystalline microstructures. In this advancement the details to train a CNN capable of

accurately localizing the plastic response of polycrystalline RVEs are presented. This advancement leveraged the insights obtained from incorporating the MKS localization to polycrystalline plasticity to define a robust CNN architecture.

As a result, this dissertation brings closer to reality the development of fully-coupled computationally inexpensive multiscale plasticity simulations by successfully establishing low-computational cost, non-iterative, localization models for localizing the anisotropic plastic response of polycrystalline microstructures. In addition, this dissertation also opens new research avenues by providing a clear path forward for successfully implementing deep learning techniques to develop accurate and feature-engineering-free localization model for heterogenous and non-linear phenomena in complex material structures.

CHAPTER 8:

Future Work

This dissertation demonstrated the developed localization models were not only accurate but also computationally efficient. However, there are still certain aspects that need to be explored and suitably incorporated in order to bolster a widespread adoption of the models and protocols developed in this framework.

The material strengthening mechanisms that drive/control the work hardening that metal alloys experience when subjected to plastic deformation (e.g., metal-forming processes) have significant impact on the resulting properties and structure of the deformed metal. As a result, in order for the developed models to be suitably accepted by the metal working industry they need not only need to incorporate work hardening but also account for the size-dependent mechanisms that control the hardening behavior of metals. Specially, when localizing the plastic response of an RVE containing small number of grains. All the localization models developed in this dissertation leverage Generalized Fourier Series (GFS) to adequately represent the important/necessary descriptors of the internal structure of the material. Subsequently, the developed localization models are obtained by either calibrating a set of microstructure independent kernels or a suitably defined CNN-based deep learning model to numerical results obtained from previously validated physics-based models. Therefore, the developed calibration protocols exhibit exceptional modularity since one can readily incorporate the physics that control the phenomenon of interest (e.g., size dependent crystal plasticity) by suitably incorporating new descriptors into the microstructure function and calibrating the kernels or the CNN to numerical simulations that account for the desired physics. As a result, one can readily incorporate the size-dependent mechanisms that control the hardening behavior of polycrystalline materials by suitably

representing them with a Legendre polynomials (a GFS useful for representing non-periodic domains) and aggregating them to the descriptors considered in this dissertation (i.e., the orientation of the crystal lattice and the macroscopically imposed plastic stretching tensor). Subsequently, the kernels or the CNN-based model can be adequately trained to CPFEM simulations that account for the effects of the size-dependent strengthening mechanisms such as micropolar crystal plasticity simulations.

It is important to notice that even though the incorporation of more complex plastic behavior is readily possible, the calibration effort increases significantly. Consequently, a data-driven and automatic calibration protocol needs to be suitably defined, and ultimately leveraged, because a direct calibration effort will require significant time to perform a thorough sampling of the new space spanned by the expanded description of the microstructure. A viable way forward is to incorporate uncertainty quantification into the protocols developed in this dissertation such that the developed models provide not only a response, but its associated uncertainty. For example, leveraging Gaussian processes in order to obtain a distribution of responses and their associated uncertainty. This new envisioned protocol is capable of predicting robust models using a smartly defined and reduced set of training points. As a result, incorporating uncertainty analysis will enable an efficient exploration of the expanded training space and the definition of a robust model using an optimized amount of training points because the training of the model will occur on the points that yield the greatest uncertainty. Finally, it must be acknowledged that none of the suggested advancements would even be possible without the work performed in this dissertation since this work not only demonstrated that robust, reduced-order, computationally inexpensive localization models for the plastic response of polycrystalline materials are able to be developed but it also provided robust training protocols to establish them.

REFERENCES

[1] D.L. McDowell, H.J. Choi, J. Panchal, R. Austin, J. Allen, F. Mistree, Plasticity-related microstructure-property relations for materials design, Key Engineering Materials, Trans Tech Publ, 2007, pp. 21-30.

[2] H.-J. Choi, D.L. Mcdowell, J.K. Allen, F. Mistree, An inductive design exploration method for hierarchical systems design under uncertainty, Engineering Optimization 40(4) (2008) 287-307.

[3] D.J. Luscher, D.L. McDowell, C.A. Bronkhorst, A second gradient theoretical framework for hierarchical multiscale modeling of materials, International Journal of Plasticity 26(8) (2010) 1248-1275.

[4] G.B. Olson, Computational design of hierarchically structured materials, Science 277(5330) (1997) 1237-1242.

[5] D.L. McDowell, J.H. Panchal, H.-J. Choi, C.C. Seepersad, J.K. Allen, F. Mistree, Integrated Design of Multiscale, Multifunctional Materials and Products, Elsevier2009.

[6] D.L. McDowell, G.B. Olson, Concurrent design of hierarchical materials and structures, Scientific Modeling and Simulation SMNS 15(1) (2008) 207.

[7] B.L. Adams, S.R. Kalidindi, D. Fullwood, Microstructure Sensitive Design for Performance Optimization, Butterworth-Heinemann2012.

[8] G.I. Taylor, Plastic strain in metals, our. Inst. Metals. 62 (1938) 307-324.

[9] G. Sachs, Zur ableitung einer fliessbedingung, Mitteilungen der deutschen Materialprüfungsanstalten, Springer1929, pp. 94-97.

[10] J. Bishop, R. Hill, XLVI. A theory of the plastic distortion of a polycrystalline aggregate under combined stresses, The London, Edinburgh, and Dublin Philosophical Magazine and Journal of Science 42(327) (1951) 414-427.

[11] J. Bishop, R. Hill, CXXVIII. A theoretical derivation of the plastic properties of a polycrystalline face-centred metal, The London, Edinburgh, and Dublin Philosophical Magazine and Journal of Science 42(334) (1951) 1298-1307.

[12] E. Kroner, On the plastic deformation of polycrystals, Acta Metallurgica 9(2) (1961) 155-161.

[13] L. Anand, M. Kothari, A computational procedure for rate-independent crystal plasticity, Journal of the Mechanics and Physics of Solids 44(4) (1996) 525-558.

[14] S.R. Kalidindi, C.A. Bronkhorst, L. Anand, Crystallographic texture evolution in bulk deformation processing of FCC metals, Journal of the Mechanics and Physics of Solids 40(3) (1992) 537-569.

[15] D. Peirce, R. Asaro, A. Needleman, An analysis of nonuniform and localized deformation in ductile single crystals, Acta metallurgica 30(6) (1982) 1087-1119.

[16] S. Harren, H. Deve, R. Asaro, Shear band formation in plane strain compression, Acta Metallurgica 36(9) (1988) 2435-2480.

[17] S. Harren, R. Asaro, Nonuniform deformations in polycrystals and aspects of the validity of the Taylor model, Journal of the Mechanics and Physics of Solids 37(2) (1989) 191-232.

[18] R.J. Asaro, A. Needleman, Overview no. 42 Texture development and strain hardening in rate dependent polycrystals, Acta Metallurgica 33(6) (1985) 923-953.

[19] Z.-s. Zhao, W.-m. Mao, F. Roters, D. Raabe, A texture optimization study for minimum earing in aluminium by use of a texture component crystal plasticity finite element method, Acta Materialia 52(4) (2004) 1003-1012.

[20] D. Raabe, Y. Wang, F. Roters, Crystal plasticity simulation study on the influence of texture on earing in steel, Computational Materials Science 34(3) (2005) 221-234.

[21] C. Xie, E. Nakamachi, Investigations of the formability of BCC steel sheets by using crystalline plasticity finite element analysis, Materials & design 23(1) (2002) 59-68.

[22] P. Wu, S. MacEwen, D. Lloyd, K. Neale, Effect of cube texture on sheet metal formability, Materials Science and Engineering: A 364(1-2) (2004) 182-187.

[23] C.C. Tasan, J.P. Hoefnagels, M. Diehl, D. Yan, F. Roters, D. Raabe, Strain localization and damage in dual phase steels investigated by coupled in-situ deformation experiments and crystal plasticity simulations, International Journal of Plasticity 63 (2014) 198-210.

[24] F. Roters, P. Eisenlohr, L. Hantcherli, D.D. Tjahjanto, T.R. Bieler, D. Raabe, Overview of constitutive laws, kinematics, homogenization and multiscale methods in crystal plasticity finite-element modeling: Theory, experiments, applications, Acta Materialia 58(4) (2010) 1152-1211.

[25] F. Feyel, S. Calloch, D. Marquis, G. Cailletaud, F.E. computation of a triaxial specimen using a polycrystalline model, Computational Materials Science 9(1) (1997) 141-157.

[26] V. Kouznetsova, W.A.M. Brekelmans, F.P.T. Baaijens, An approach to micro-macro modeling of heterogeneous materials, Computational Mechanics 27(1) (2001) 37-48.

[27] C. Miehe, J. Schröder, J. Schotte, Computational homogenization analysis in finite plasticity Simulation of texture development in polycrystalline materials, Computer Methods in Applied Mechanics and Engineering 171(3) (1999) 387-418.

[28] R.J.M. Smit, W.A.M. Brekelmans, H.E.H. Meijer, Prediction of the mechanical behavior of nonlinear heterogeneous systems by multi-level finite element modeling, Computer Methods in Applied Mechanics and Engineering 155(1) (1998) 181-192.

[29] D. Balzani, A. Gandhi, A. Klawonn, M. Lanser, O. Rheinbach, J. Schröder, One-Way and Fully-Coupled FE2 Methods for Heterogeneous Elasticity and Plasticity Problems: Parallel Scalability and an Application to Thermo-Elastoplasticity of Dual-Phase Steels, Springer International Publishing, Cham, 2016, pp. 91-112.

[30] F. Feyel, J.-L. Chaboche, Multi-scale non-linear FE2 analysis of composite structures: damage and fiber size effects, Revue Européenne des Éléments Finis 10(2-4) (2001) 449-472.

[31] R.A. Lebensohn, N-site modeling of a 3D viscoplastic polycrystal using fast Fourier transform, Acta materialia 49(14) (2001) 2723-2737.

[32] H. Moulinec, P. Suquet, A numerical method for computing the overall response of nonlinear composites with complex microstructure, Computer methods in applied mechanics and engineering 157(1-2) (1998) 69-94.

[33] T. Mura, Micromechanics of defects in solids, Springer Science & Business Media2013.

[34] B. Liu, D. Raabe, F. Roters, P. Eisenlohr, R. Lebensohn, Comparison of finite element and fast Fourier transform crystal plasticity solvers for texture prediction, Modelling and Simulation in Materials Science and Engineering 18(8) (2010) 085005.

[35] R.A. Lebensohn, R. Brenner, O. Castelnau, A.D. Rollett, Orientation image-based micromechanical modelling of subgrain texture evolution in polycrystalline copper, Acta Materialia 56(15) (2008) 3914-3926.

[36] R.A. Lebensohn, A.K. Kanjarla, P. Eisenlohr, An elasto-viscoplastic formulation based on fast Fourier transforms for the prediction of micromechanical fields in polycrystalline materials, International Journal of Plasticity 32-33 (2012) 59-69.

[37] P. Eisenlohr, M. Diehl, R.A. Lebensohn, F. Roters, A spectral method solution to crystal elasto-viscoplasticity at finite strains, International Journal of Plasticity 46 (2013) 37-53.

[38] A. Prakash, R.A. Lebensohn, Simulation of micromechanical behavior of polycrystals: finite elements versus fast Fourier transforms, Modelling and Simulation in Materials Science and Engineering 17(6) (2009) 064010.

[39] E. Kroner, Statistical Modelling, in: J. Gittus, J. Zarka (Eds.), Modelling Small Deformations of Polycrystals, Elsevier Science Publishers, London, 1986, pp. 229-291.

[40] E. Kröner, Bounds for effective elastic moduli of disordered materials, Journal of the Mechanics and Physics of Solids 25(2) (1977) 137-155.

[41] S.R. Kalidindi, Hierarchical Materials Informatics: Novel Analytics for Materials Data, Elsevier2015.

[42] S.R. Kalidindi, S.R. Niezgoda, G. Landi, S. Vachhani, T. Fast, A novel framework for building materials knowledge systems, Computers, Materials, & Continua 17(2) (2010) 103-125.

[43] S.R. Kalidindi, Computationally Efficient, Fully Coupled Multiscale Modeling of Materials Phenomena Using Calibrated Localization Linkages, ISRN Materials Science 2012 (2012) 13.

[44] G. Landi, S.R. Kalidindi, Thermo-elastic localization relationships for multi-phase composites, Computers, Materials, & Continua 16(3) (2010) 273-293.

[45] Y.C. Yabansu, D.K. Patel, S.R. Kalidindi, Calibrated localization relationships for elastic response of polycrystalline aggregates, Acta Materialia 81 (2014) 151-160.

[46] N.H. Paulson, M.W. Priddy, D.L. McDowell, S.R. Kalidindi, Reduced-order structure-property linkages for polycrystalline microstructures based on 2-point statistics, Acta Materialia 129 (2017) 428-438.

[47] D.B. Brough, D. Wheeler, S.R. Kalidindi, Materials Knowledge Systems in Python--a Data Science Framework for Accelerated Development of Hierarchical Materials, Integr Mater Manuf I 6(1) (2017) 36.

[48] Y.C. Yabansu, S.R. Kalidindi, Representation and calibration of elastic localization kernels for a broad class of cubic polycrystals, Acta Materialia 94 (2015) 26-35.

[49] G. Landi, S.R. Niezgoda, S.R. Kalidindi, Multi-scale modeling of elastic response of three-dimensional voxel-based microstructure datasets using novel DFT-based knowledge systems, Acta Materialia 58(7) (2010) 2716-2725.

[50] T. Fast, S.R. Kalidindi, Formulation and Calibration of Higher-Order Elastic Localization Relationships Using the MKS Approach Acta Materialia 59 (2011) 4595-4605.

[51] H.-J. Bunge, Texture analysis in materials science: mathematical methods, Elsevier2013.

[52] W.L. Briggs, The DFT: an owners' manual for the discrete Fourier transform, Siam1995.

[53] S.C. Chapra, R.P. Canale, Numerical methods for engineers, Boston: McGraw-Hill Higher Education2010.

[54] A. Gupta, A. Cecen, S. Goyal, A.K. Singh, S.R. Kalidindi, Structure–property linkages using a data science approach: Application to a non-metallic inclusion/steel composite system, Acta Materialia 91 (2015) 239-254.

[55] M.I. Latypov, S.R. Kalidindi, Data-driven reduced order models for effective yield strength and partitioning of strain in multiphase materials, Journal of Computational Physics (2017).

[56] Modeling Across Scales: A Roadmapping Study for Connecting Materials Models and Simulations Across Length and Time Scales, The Minerals, Metals, and Materials Society, Warrendale, PA, 2015.

[57] A.A. Gusev, Representative volume element size for elastic composites: a numerical study, Journal of the Mechanics and Physics of Solids 45(9) (1997) 1449-1459.

[58] S.R. Niezgoda, D.M. Turner, D.T. Fullwood, S.R. Kalidindi, Optimized structure based representative volume element sets reflecting the ensemble-averaged 2-point statistics, Acta Materialia 58(13) (2010) 4432-4445.

[59] S.R. Kalidindi, S.R. Niezgoda, A.A. Salem, Microstructure informatics using higher-order statistics and efficient data-mining protocols, JOM 63(4) (2011) 34-41.

[60] S.R. Niezgoda, Y.C. Yabansu, S.R. Kalidindi, Understanding and visualizing microstructure and microstructure variance as a stochastic process, Acta Materialia 59(16) (2011) 6387-6400.

[61] S.M. Qidwai, D.M. Turner, S.R. Niezgoda, A.C. Lewis, A.B. Geltmacher, D.J. Rowenhorst, S.R. Kalidindi, Estimating the response of polycrystalline materials using sets of weighted statistical volume elements, Acta Materialia 60(13) (2012) 5284-5299.

[62] B.L. Adams, X. Gao, S.R. Kalidindi, Finite approximations to the second-order properties closure in single phase polycrystals, Acta Materialia 53(13) (2005) 3563-3577.

[63] M. Beran, Application of statistical theories to heterogeneous materials, physica status solidi (a) 6(2) (1971) 365-384.

[64] M.J. Beran, T.A. Mason, B.L. Adams, T. Olsen, Bounding elastic constants of an orthotropic polycrystal using measurements of the microstructure, Journal of the Mechanics and Physics of Solids 44(9) (1996) 1543-1563.

[65] S. Lin, H. Garmestani, Statistical continuum mechanics analysis of an elastic two-isotropic-phase composite material, Composites Part B: Engineering 31(1) (2000) 39-46.

[66] B.L. Adams, T. Olson, The mesostructure—properties linkage in polycrystals, Progress in Materials Science 43(1) (1998) 1-87.

[67] M.J. Beran, A. Pytte, Statistical continuum theories, American Journal of Physics 36(10) (1968) 923-923.

[68] S.R. Kalidindi, M. Binci, D. Fullwood, B.L. Adams, Elastic properties closures using second-order homogenization theories: case studies in composites of two isotropic constituents, Acta Materialia 54(11) (2006) 3117-3126.

[69] G.W. Milton, The theory of composites, The Theory of Composites, by Graeme W. Milton, pp. 748. ISBN 0521781256. Cambridge, UK: Cambridge University Press, May 2002. (2002) 748.

[70] S. Torquato, Effective stiffness tensor of composite media—I. Exact series expansions, Journal of the Mechanics and Physics of Solids 45(9) (1997) 1421-1448.

[71] D.T. Fullwood, S.R. Niezgoda, S.R. Kalidindi, Microstructure reconstructions from 2-point statistics using phase-recovery algorithms, Acta Materialia 56(5) (2008) 942-948.

[72] M. Binci, D. Fullwood, S.R. Kalidindi, A new spectral framework for establishing localization relationships for elastic behavior of composites and their calibration to finite-element models, Acta Materialia 56(10) (2008) 2272-2282.

[73] H. Garmestani, S. Lin, B.L. Adams, S. Ahzi, Statistical continuum theory for large plastic deformation of polycrystalline materials, Journal of the Mechanics and Physics of Solids 49(3) (2001) 589-607.

[74] H. Garmestani, S. Lin, B. Adams, Statistical continuum theory for inelastic behavior of a two-phase medium, International Journal of Plasticity 14(8) (1998) 719-731.

[75] A.S. Khan, S. Huang, Continuum theory of plasticity, John Wiley & Sons, 1995.

[76] P. Van Houtte, Application of plastic potentials to strain rate sensitive and insensitive anisotropic materials, International Journal of Plasticity 10(7) (1994) 719-748.

[77] M. Knezevic, S.R. Kalidindi, D. Fullwood, Computationally efficient database and spectral interpolation for fully plastic Taylor-type crystal plasticity calculations of face-centered cubic polycrystals, International Journal of Plasticity 24(7) (2008) 1264-1276.

[78] M. Knezevic, H.F. Al-Harbi, S.R. Kalidindi, Crystal plasticity simulations using discrete Fourier transforms, Acta Materialia 57(6) (2009) 1777-1784.

[79] H.F. Alharbi, S.R. Kalidindi, Crystal plasticity finite element simulations using a database of discrete Fourier transforms, International Journal of Plasticity 66 (2015) 71-84.

[80] D. Montes de Oca Zapiain, E. Popova, S.R. Kalidindi, Prediction of microscale plastic strain rate fields in two-phase composites subjected to an arbitrary macroscale strain rate using the materials knowledge system framework, Acta Materialia 141(Supplement C) (2017) 230-240.

[81] R. Hill, The mathematical theory of plasticity, Oxford university press1998.

[82] L.E. Malvern, Introduction to the Mechanics of a Continuous Medium, 1969.

[83] I. Abaqus, ABAQUS/CAE : user's manual, Version 6.5. ed., Abaqus, Inc., Providence, RI :, 2004.

[84] T. Fast, S.R. Niezgoda, S.R. Kalidindi, A new framework for computationally efficient structure–structure evolution linkages to facilitate high-fidelity scale bridging in multi-scale materials models, Acta Materialia 59(2) (2011) 699-707.

[85] H. Garmestani, S. Lin, B.L. Adams, Statistical continuum theory for inelastic behavior of a two-phase medium, International Journal of Plasticity 14(8) (1998) 719-731.

[86] J.W. Cooley, J.W. Tukey, An algorithm for the machine calculation of complex Fourier series, Mathematics of computation 19(90) (1965) 297-301.

[87] T. Sauer, Numerical Analysis, Addison-Wesley Publishing Company2011.

[88] M.A. Groeber, M.A. Jackson, DREAM. 3D: a digital representation environment for the analysis of microstructure in 3D, Integr Mater Manuf I 3(1) (2014) 5.

[89] S.R. Kalidindi, A. Bhattacharya, R. Doherty, Detailed Analysis of Plastic Deformation in Columnar Polycrystalline Aluminum Using Orientation Image Mapping and Crystal Plasticity Models, Proceedings of the Royal Society of London: Mathematical, Physical and Engineering Sciences. 460(2047) (2004) 1935 - 1956

[90] E. Hall, The deformation and ageing of mild steel: III discussion of results, Proceedings of the Physical Society. Section B 64(9) (1951) 747.

[91] N. Petch, The cleavage strength of polycrystals, Journal of the Iron and Steel Institute 174 (1953) 25-28.

[92] J.R. Mayeur, D.L. McDowell, D.J. Bammann, Dislocation-based micropolar single crystal plasticity: Comparison of multi- and single criterion theories, Journal of the Mechanics and Physics of Solids 59(2) (2011) 398-422.

[93] J.R. Mayeur, D.L. McDowell, A comparison of Gurtin type and micropolar theories of generalized single crystal plasticity, International Journal of Plasticity 57 (2014) 29-51.

[94] Z. Yang, Y.C. Yabansu, D. Jha, W.-k. Liao, A.N. Choudhary, S.R. Kalidindi, A. Agrawal, Establishing structure-property localization linkages for elastic deformation of three-dimensional high contrast composites using deep learning approaches, Acta Materialia 166 (2019) 335-345.

[95] A. Krizhevsky, I. Sutskever, G.E. Hinton, Imagenet classification with deep convolutional neural networks, Advances in neural information processing systems, 2012, pp. 1097-1105.

[96] S. Lawrence, C.L. Giles, A.C. Tsoi, A.D. Back, Face recognition: A convolutional neural-network approach, IEEE transactions on neural networks 8(1) (1997) 98-113.

[97] Y. LeCun, Y. Bengio, G. Hinton, Deep learning, nature 521(7553) (2015) 436.

[98] C. Szegedy, W. Liu, Y. Jia, P. Sermanet, S. Reed, D. Anguelov, D. Erhan, V. Vanhoucke, A. Rabinovich, Going deeper with convolutions, Proceedings of the IEEE conference on computer vision and pattern recognition, 2015, pp. 1-9.

[99] J.J. Tompson, A. Jain, Y. LeCun, C. Bregler, Joint training of a convolutional network and a graphical model for human pose estimation, Advances in neural information processing systems, 2014, pp. 1799-1807.

[100] A. Cecen, H. Dai, Y.C. Yabansu, S.R. Kalidindi, L. Song, Material structure-property linkages using three-dimensional convolutional neural networks, Acta Materialia 146 (2018) 76-84.

[101] R. Liu, Y.C. Yabansu, A. Agrawal, S.R. Kalidindi, A.N. Choudhary, Machine learning approaches for elastic localization linkages in high-contrast composite materials, Integr Mater Manuf I 4(1) (2015) 13.

[102] V. Nair, G.E. Hinton, Rectified linear units improve restricted boltzmann machines, Proceedings of the 27th international conference on machine learning (ICML-10), 2010, pp. 807-814.

[103] D.P. Kingma, J. Ba, Adam: A method for stochastic optimization, arXiv preprint arXiv:1412.6980 (2014).